2016

MEASUREMENT OF RARE EARTH AND URANIUM ELEMENTS USING LASER-INDUCED BREAKDOWN SPECTROSCOPY (LIBS) IN AN AEROSOL SYSTEM FOR NUCLEAR SAFEGUARDS APPLICATIONS

Ammon N. Williams
Virginia Commonwealth University

2016

MEASUREMENT OF RARE EARTH AND URANIUM ELEMENTS USING LASER-INDUCED BREAKDOWN SPECTROSCOPY (LIBS) IN AN AEROSOL SYSTEM FOR NUCLEAR SAFEGUARDS APPLICATIONS

Ammon N. Williams
Virginia Commonwealth University, williamsan25@vcu.edu

MEASUREMENT OF RARE EARTH AND URANIUM ELEMENTS USING LASER-INDUCED BREAKDOWN SPECTROSCOPY (LIBS) IN AN AEROSOL SYSTEM FOR NUCLEAR SAFEGUARDS APPLICATIONS

A Dissertation

Presented in Partial Fulfillment of the Requirements for the

Degree of Doctor of Philosophy

with a Major in

Mechanical and Nuclear Engineering

in the

Graduate School

Virginia Commonwealth University

By

Ammon Ned Williams

Major Professor: Supathorn Phongikaroon, Ph.D.

November 21, 2016

Abstract

The primary objective of this research is to develop an applied technology and provide an assessment for remotely measuring and analyzing the real time or near real time concentrations of used nuclear fuel (UNF) elements in electrorefiners (ER). Here, Laser-Induced Breakdown Spectroscopy (LIBS) in UNF pyroprocessing facilities was investigated. LIBS is an elemental analysis method, which is based on the emission from plasma generated by focusing a laser beam into the medium. This technology has been reported to be applicable in solids, liquids (includes molten metals), and gases for detecting elements of special nuclear materials. The advantages of applying the technology for pyroprocessing facilities are: (i) Rapid real-time elemental analysis; (ii) Direct detection of elements and impurities in the system with low limits of detection (LOD); and (iii) Little to no sample preparation is required. One important challenge to overcome is achieving reproducible spectral data over time while being able to accurately quantify fission products, rare earth elements, and actinides in the molten salt. Another important challenge is related to the accessibility of molten salt, which is heated in a heavily insulated, remotely operated furnace in a high radiation environment within an argon gas atmosphere. This dissertation aims to address these challenges and approaches in the following phases with their highlighted outcomes:

1. Aerosol-LIBS system design and aqueous testing: An aerosol-LIBS system was designed around a Collison nebulizer and tested using deionized water with Ce, Gd, and Nd concentrations from 100 ppm to 10,000 ppm. The average %RSD values between the sample repetitions were 4.4% and 3.8% for the Ce and Gd lines, respectively. The univariate calibration curve for Ce using the peak intensities of the Ce 418.660 nm line was recommended and had an R^2 value, LOD, and RMSECV of 0.994, 189 ppm, and 390 ppm, respectively. The recommended Gd calibration curve was generated

using the peak areas of the Gd 409.861 nm line and had an R^2, LOD, and RMSECV of 0.992, 316 ppm, and 421 ppm, respectively. The partial least squares (PLS) calibration curves yielded similar results with RMSECV of 406 ppm and 417 ppm for the Ce and Gd curves, respectively.

2. High temperature aerosol-LIBS system design and $CeCl_3$ testing: The aerosol-LIBS system was transitioned to a high temperature and used to measure Ce in molten LiCl-KCl salt within a glovebox environment. The concentration range studied was from 0.1 wt% to 5 wt% Ce. Normalization was necessary due to signal degradation over time; however, with the normalization the %RSD values averaged 5% for the mid and upper concentrations studied. The best univariate calibration curve was generated using the peak areas of the Ce 418.660 nm line. The LOD for this line was 148 ppm with the RMSECV of 647 ppm. The PLS calibration curve was made using 7 latent variables (LV) and resulting in the RMSECV of 622 ppm. The LOD value was below the expected rare earth concentration within the ER.

3. Aerosol-LIBS testing using UCl_3: Samples containing UCl_3 with concentrations ranging from 0.3 wt% to 5 wt% were measured. The spectral response in this range was linear. The best univariate calibration curves were generated using the peak areas of the U 367.01 nm line and had an R^2 value of 0.9917. Here, the LOD was 647 ppm and the RMSECV was 2,290 ppm. The PLS model was substantially better with a RMSECV of 1,110 ppm. The LOD found here is below the expected U concentrations in the ER. The successful completion of this study has demonstrated the feasibility of using an aerosol-LIBS analytical technique to measure rare earth elements and actinides in the pyroprocessing salt.

Acknowledgments

I am grateful for my wife, Katherine, for her love and support and for my sweet daughters that have sacrificed so much time with their dad for me to finish this work. I owe so much to my family and friends for their love, support, and encouragement along the way. I would also like to acknowledge my God because I am nothing without Him. I am sincerely grateful to my advisor and friend, Dr. Supathorn Phongikaroon, for the countless hours he has spent training and mentoring me. In addition, he has allowed me to make the research my own and granted me with opportunities to present at national and international conferences. I truly appreciate those opportunities. I want to thank Dalsung Yoon for his assistance and friendship throughout my time working on this dissertation. In addition, I want to thank Micheal Woods, Hunter Andrews, Khalid Taha, Samaneh Rakhshan Pouri, Riyadh Motny, Keith Bryce, Sean Walker, and John Arcibal for their assistance, informative conversations, and fun times. I am especially grateful to my committee members, Drs. Sama Bilbao y León, Dmitry Pestov, Laleh Golshahi, and Sarah Rutan for their invaluable inputs. I am so glad that I have had the opportunity to rub shoulders with such great people.

Most importantly, I would like to express my sincere appreciation to the DOE Office of Nuclear Energy's Nuclear Energy University Program under the work package #NU-12-VA-VCU-0203-01 for the first three year funding support and a generous financial support from the Nuclear Regulatory Commission Graduate Fellowship for the final year of my Ph.D. degree.

Contents

List of Figures

List of Tables

Abbreviations & Nomenclature

Abbreviations and Acronyms

NAME	DESCRIPTION	UNIT
AES	Atomic Emission Spectroscopy	
ANN	Artificial Neural Networks	
CCD	Charge Coupled Device	
CMD	Count Median Diameter	μm
DDG	Digital Delay Generator	
DFA	Discriminant Functional Analysis	
dscm	Dry standard cubic meter	
DU	Depleted uranium	
EBR-II	Experimental Breeder Reactor II	
ER	Electrorefiner	
FOM	Figures Of Merit	
GSD	Geometric Standard Deviation	
GUI	Graphic User Interface	
HEPA	High-Efficiency Particulate Air (filter)	
ICCD	Intensified Charge-Coupled Device	
ICP-MS	Inductively Coupled Plasma Mass Spectrometry	
LDA	Linear Discriminant Analysis	
LIBS	Laser-Induced Breakdown Spectroscopy	
INL	Idaho National Laboratory	
LOD	Limit Of Detection	wt% or ppm

LOOCV	Leave One Out Cross Validation	
LV	Latent Variables	
MCP	Micro-channel plate	
Nd:YAG	Neodymium Yttrium Aluminum Garnet (type of laser)	
NIST	National Institute of Standards & Technology	
NPT	National Pipe Thread	
PCA	Principle Component Analysis	
PLS	Partial Least Squares	
ppm	parts-per-million	
PUREX	Plutonium Uranium Redox EXtraction	
Re	Reynolds number	
RMSE	Root Mean Squared Error	
RMSECV	Root Mean Squared Error of Cross Validation	
RMSEP	Root Mean Square Error of Prediction	
%RSD	Relative Standard Deviation	%
SBR	Signal-to-Background Ratio	
SNR	Signal-to-Noise Ratio	
SMPS	Scanning Mobility Particle Sizer	
UNF	Used Nuclear Fuel	
VF	Volume Fraction	

Symbols

NAME	DESCRIPTION	UNIT
s	Standard deviation	
M	Mean between experimental repetitions	
n_r	Number of repetitions	

r_i	Value for the "i^{th}" repetition	
b_1	Slope of the linear regression line	
σ_b	Standard deviation of the blank sample	
b_0	Y-intercept of the linear regression line	
x	Concentration	wt% or ppm
$\bar{x}$	Mean of the concentration values	wt% or ppm
y	Spectral response	a.u.
$\bar{y}$	Mean of spectral response	a.u.
$S_{y/x}$	Standard deviation in the y-direction	
$\hat{y}$	Predicted spectral response from regression	
$t_{95\%}$	Students t value at 95%	
y_{CI}	Regression confidence interval	
p_{PI}	Regression prediction interval	
x_m	Measured concentration	wt% or ppm
x_{atv}	Accepted true value concentration	wt% or ppm
x_{CV}	Predicted concentration from cross validation	wt% or ppm
y_m	Measured spectral response	a.u.
S_{xm}	Uncertainty of the measurement	
X	Independent variables (spectra) in PLS	
Y	Dependant variables (concentration) in PLS	
n	Number of samples $\times$ the repetitions	
m	Number of spectral data points (PLS)	
T	Latent variable matrix (PLS)	
P	Loading or weight of X (PLS)	
C	Loading or weight of Y (PLS)	
$\hat{Y}$	Predicted concentration (PLS)	
B	PLS regression coefficient matrix	

R_1	PLS covariance	
W_1	Weight of the covariance with respect to X	
C_1	Weight of the covariance with respect to Y	
Δ_1	Matrix of values corresponding to the covariance	
u_1	First pseudo latent variable	
n_i	Number of particles within a specific size range	
N	Total number of particles measured	
d_i	Size range mid-point diameter	μm
d_g	Geometric mean diameter	μm
σ_g	Geometric standard deviation	
ΔP	Pressure differential or drop	psi
f	Friction factor	
l	Tubing length	m
D	Inside diameter of tubing	m
ρ	Density	kg/m^3
ν	Kinematic viscosity	m^2/s

Chapter 1

Introduction

1.1 Purpose

The purpose of this dissertation is to investigate and assess laser-induced breakdown spectroscopy (LIBS) as a potential analytical technique to monitor special nuclear materials in the molten salt electrolyte used in pyroprocessing towards material accountability and safeguards applications. The focus was on the development and testing of an innovative aerosol-LIBS system. This system was first developed and tested using an aqueous media to acquire essential operating parameters and experience. Following this testing, the system was adapted to the more stringent requirements for high temperature operation with molten salts and operated using $CeCl_3$ as a surrogate. Finally, this novel aerosol-LIBS system was tested using UCl_3-LiCl-KCl molten salt.

1.2 Motivation

Nuclear power is an essential component of the United States energy portfolio because it can generate clean, safe, and reliable energy. However, the nuclear industry in the United States is facing a major challenge as a result of used nuclear fuel (UNF) disposition and management. The United States has adapted a once through fuel cycle where the fuel is used, temporarily stored, and in the future, permanently interred in a geological repository[1]. This approach is wasteful with approximately 95% of the uranium being unused[2]. In addition, significant technical, political, and environmental challenges exist in the development of a long term

geological repository. Many countries, including France, use a PUREX process to recycle the UNF to better utilize the uranium and actinide resources as well as to reduce the need for a long term geological repository[1]. The PUREX process is an aqueous technique that was developed at the University of Chicago under the project led by Glenn T. Seaborg; however, it was commercially abandoned by the United States in 1977 in order to reduce the proliferation of special nuclear materials, specifically plutonium[3].

Electrochemical separation (also known as 'pyroprocessing technology' and 'electrometallurgical process') of UNF is a dry reprocessing alternative to the PUREX process[4]. In pyroprocessing technology, UNF within a hot cell environment is chopped and loaded into an anode basket. The anode basket is then positioned within an electrorefiner (ER) where the uranium is electrochemically dissolved from the fuel and transported through a molten salt electrolyte and deposited on a cathode where it can be recovered. This approach to UNF recycling is advantageous because the plutonium in the fuel cannot be separated from the other actinides making this technology proliferation resistant. However, during electrorefining, fission products, rare earth elements, and transuranics (including plutonium) accumulate in the molten salt due to process chemistry. Monitoring the concentrations of these elements in this salt for material accountability purposes is essential for safeguarding the special nuclear material within pyroprocessing facility[5]. Analytical methods to measure the composition of the salt have been limited due to the high temperature operating conditions (typically, 723 K to 773 K) and the high radiation environment that exists within the hot cell. As a result, liquid salt samples are usually drawn from the ER for later measurement via inductively coupled plasma mass spectrometry (ICP-MS)[6]. This process of extraction, material transfer, and later sample preparation and measurement is cumbersome and can impose significant delay between sampling and compositional results.

An alternative analytical approach to the traditional ICP-MS method is LIBS. LIBS is attractive because it can be done in-situ, with little to no sample preparation, and compositional information of the salt can be obtained in near real-time[7]. Several LIBS studies[8–11]

have been conducted in a molten LiCl-KCl salt to date using a static salt surface approach. Whereas these studies show that LIBS is a promising alternative for salt measurements, there are still significant long term challenges of using LIBS in a ER that need to be addressed. For example: (1) collecting a representative, homogeneous measurement, (2) reduction of material splashing and optical degradation, and (3) repeatability over time due to surface effects of the salt. These concerns provide a motivation for us to explore a new innovative system, specifically an aerosol liquid LIBS configuration, to mitigate these challenges in the ER. Successful completion of this study will provide valuable insights that may pave a path forward for enhanced material accountability and safeguards of pyroprocessing.

1.3 Approach

Definitely, a feasibility assessment of an aerosol-LIBS approach to measure special nuclear materials in pyroprocessing salt is the crucial objective. Therefore, a careful approach must be planned in order to obtain this successful outcome. To accomplish this goal, four phases have been developed and explored. In Phase I(a), a simple, aqueous experimental series (20 wt% LiCl-KCl salt) was conducted. In these experiments, a static surface LIBS configuration was used to measure $CeCl_3$ in the mixture. In this case, the $CeCl_3$ was a surrogate for UCl_3. In Phase I(b), an electromagnetic mechanism was explored to pump molten salt. The motivation for this phase was to develop a molten salt pump that could be used to create flowing liquid configurations for LIBS testing.

In the second phase (Phase II), an aerosol-LIBS system was developed (Patent pending) using a Collision nebulizer and tested at room temperature using an aqueous media with varying concentrations of Ce and Gd. LIBS analysis was performed along with ICP-MS analysis to verify results. In Phase III, the aerosol-LIBS system was transitioned to high temperature operation and tested. Testing was done using a molten $CeCl_3$-LiCl-KCl salt within a glovebox environment.

In the final phase of this work (Phase IV), UCl_3 was measured in the LiCl-KCl salt via the established aerosol-LIBS system. These experiments were used to assess the aerosol-LIBS system performance as well as the overall feasibility of the system for pyroprocessing salt measurements. Table 1.1 shows the time line for the completion of each phase of the project.

Table 1.1: Time line showing the effort period for each phase of the research project.

Phase	FY 2013	FY 2014	FY 2015	FY 2016
I(a)	✓	✓		
I(b)	✓	✓		
II		✓	✓	
III			✓	✓
IV				✓

1.4 Background

1.4.1 Pyroprocessing Technology

The Experimental Breeder Reactor II (EBR-II) was a sodium cooled fast reactor that was developed by Argonne National Laboratory and built in Idaho at the Argonne National Laboratory-West (now the Idaho National Laboratory)[12]. EBR-II successfully operated from 1963 to 1994. The reactor core configuration consisted of an enriched uranium metal driver fuel that was thermally bonded to a stainless steel cladding with sodium metal. The core was surrounded by a depleted uranium blanket fuel. The concept behind EBR-II was to generate thermal energy from fast neutrons in the core while generating secondary reactions in the blanket fuel to breed additional fuels. In addition, because this is a fast reactor, the U-238 isotope (which is the most naturally abundant) can be utilized providing Pu-239. As a result, this reactor was intended to better utilize uranium resources as well as breed new fuel, making this reactor concept more sustainable than traditional light water reactor designs. Because the actinides are burned in the reactor, this reactor design is more proliferation

resistant. However, for this process to work efficiently, recycling of the fuel is required. Indeed, EBR-II was built with this intention and on-site UNF recycling was done from 1965 to 1969 using a melt refining process[12].

Traditional aqueous recycling methods such as the PUREX process are poorly suited for recycling the sodium bonded metallic fuel used in EBR-II. The PUREX process requires a large foot print making on-site recycling of the UNF unfeasible. In addition, the organic extraction materials, are highly susceptible to radiation damage from the short lived radionuclides. As a result, prior to processing UNF with the PUREX process, the UNF is stored in cooling pools for 3 to 5 years. In addition, as part of the PUREX process, plutonium is extracted in pure form which raises proliferation concerns.

To address concern with the PUREX process for recycling EBR-II UNF, a "dry" electrochemical reprocessing method called pyroprocessing (also known as 'electrometallurgical', 'electrochemical', and 'pyrochemical') was developed by the Argonne National Laboratory[13]. This process is advantages for processing EBR-II fuel for several reasons: (1) it has a very small foot print which allows for easy on-site recycling of the fuel, (2) it is extremely resistant to radiation so no UNF cooling is required prior to treatment, and (3) no violent reaction of the sodium bonding material occurs since this is a dry process. In addition, pyroprocessing is more proliferation resistant because the plutonium cannot be extracted from the UNF in pure (weapons grade) form. Though pyroprocessing was developed in the United States, many other nations including Russia, Japan, South Korea, and the UK are actively pursuing this technology[14].

Pyroprocessing of UNF can be broken down into several key steps as shown in Figure 1.1. In the first step, the fuel rods are mechanically chopped to expose the metallic fuel. The chopped fuel is then added to an anode basket and immersed into a molten salt (UCl_3-LiCl-KCl) electrolyte within the ER. A stainless steel cathode is also immersed in the salt. When a current is applied across the electrodes, the uranium metal electrochemically dissolves into the molten salt electrolyte and is transported to and deposits on the cathode. Following

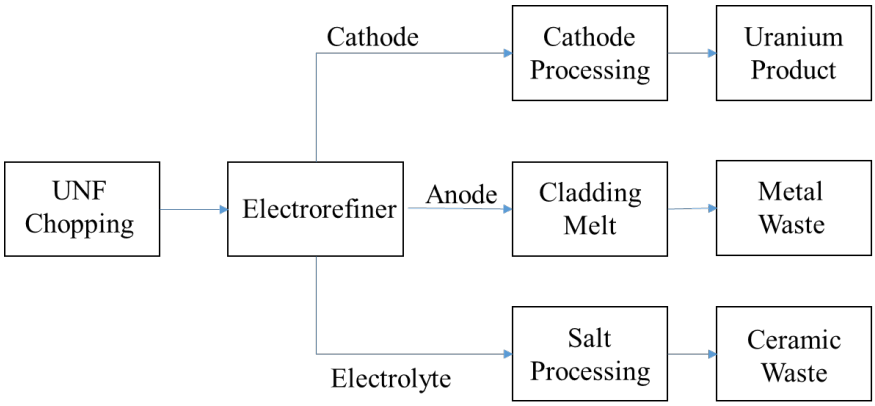

Figure 1.1: Basic block diagram for pyroprocessing of used nuclear fuel.

electrorefining, the cathode is removed from the ER and processed to remove the uranium metal for additional fuel. The anode is also removed from the ER and the cladding along with many of the fission products are melted to form a metallic waste form. The electrolyte itself accumulates sodium, fission products, and transuranics which interfere with process chemistry over time. To maintain a steady state condition within the ER, salt from the ER is periodically removed, mixed with zeolite and vitrified to form a stable ceramic waste form.

Although pyroprocessing was specifically designed to process EBR-II UNF, its application can be extended to commercial oxide fuel. In advanced pyroprocessing flow sheets, an oxide reduction step is included to first reduce the UO_2 fuel to metallic form[15]. In this case, an electrochemical cell is used in which the oxide fuel is loaded into an anode basket immersed in a LiCl electrolyte. When a current is applied, the actinides in the fuel are reduced to metallic form and gas (CO_2, CO, and O_2) is formed at the cathode. As a result, pyroprocessing is not limited to metallic fuels and is a proliferation resistant alternative to the traditional aqueous recycling processes.

1.4.2 Laser-Induced Breakdown Spectroscopy

LIBS is an atomic emission spectroscopy (AES) method that can be used to measure the atomic composition of a sample. In AES, each element emits light at very distinct wave-

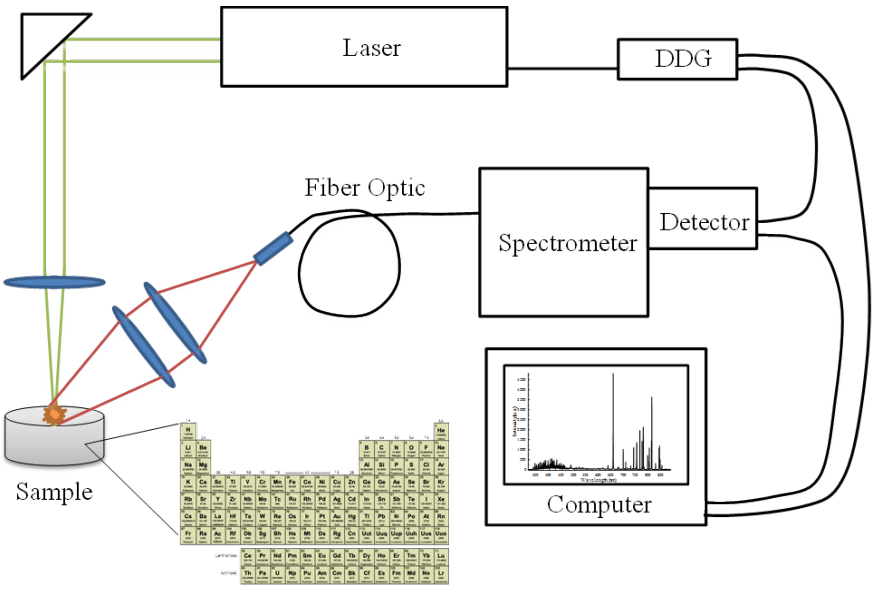

Figure 1.2: Schematic of a typical LIBS setup.

lengths to form a "fingerprint" spectra for that element. AES has been accomplished using a number of different excitation sources including flame, electrode arcs, microwave-induced plasma, and hollow cathode lamps[16]. After the invention of the laser in 1960, Brech and Cross[17] were the first to demonstrate the formation of a laser-induced plasma. This discovery led quickly to the emerging field of LIBS.

A typical setup for LIBS is shown in Figure 1.2. In LIBS, a pulsed laser is focused onto a material surface to vaporize and ionize the sample in the creation of a plasma plume. As the plasma cools, the ionized atoms return to their ground states with the emission of characteristic light which can be collected via an optical configuration. From this light, a spectrum of the emitted wavelengths can be generated via a spectrometer and detector.

LIBS is highly time dependent and the time interval between the laser firing and detector acquisition is crucial[16]. The reason for this dependence is shown graphically in Figure 1.3. In the first nanosecond after the laser initiation, the sample is heated and ablated in the formation of a plasma. During a brief time after the plasma formation, a continuum background light is emitted. This "white" light yields no atomic information and can saturate the detector. As the plasma cools, spectral emissions from the different elements become

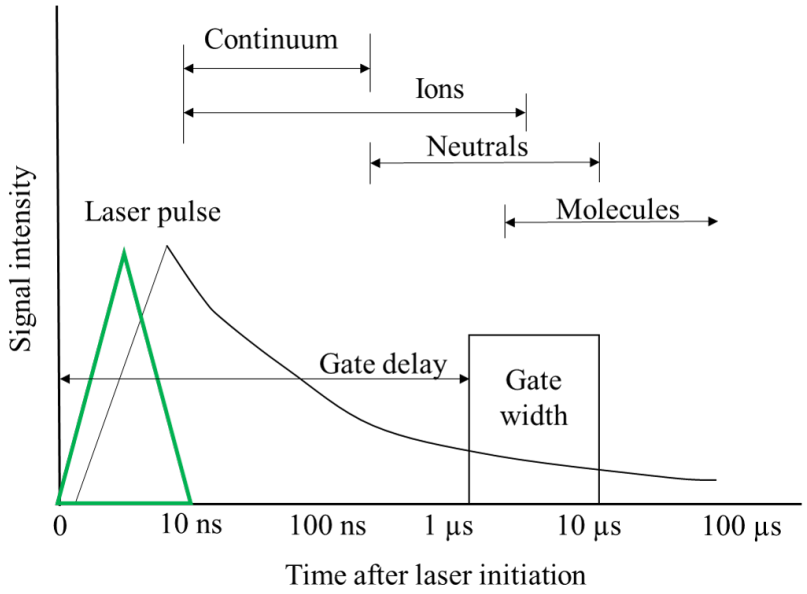

Figure 1.3: Lifetime of plasma formed using LIBS.

dominant. As a result, in LIBS, the detector is gated to block out the continuum light in order to acquire only the spectral data of interest. Increasing the gate delay not only reduces the continuum background and reduces the overall intensity, but also influences the type of spectral lines that are being observed. Typically the ionic lines are stronger earlier on in the plasma lifetime whereas molecular information is only available at longer gate delays. As a result, it is common to not only gate the detector, but to use a specific gate width. Both gate delay and gate width are typically controlled using a digital delay generator (DDG) combined with the detector.

Once the atomic spectrum of the material is obtained, qualitative information about the sample can be derived based on the wavelengths present. However, the intensity of the spectral lines can be correlated to the amount of the element that emitted them. Thus, with the construction of calibration curves, quantitative information about the elemental concentration within the sample can be obtained. LIBS is extremely versatile and can be used to analyze samples in a variety of sample compositions and phases including solids[18], liquids[19–21], gases[22], and aerosols[23, 24] without significant modification to the experimental equipment. More information will be discussed in the later chapters.

1.5 Organization of the Dissertation

Chapter 1 contains the purpose, motivation, approach, and background information for the project. Chapter 2 is a literature review of the relevant LIBS studies that have been done in molten salts, actinides, and in different environmental configurations. In Chapter 3, the analytical methodology for processing the spectral data, calculating univariate calibration curves, partial least squares (PLS) modeling, and statistical data sets are described. In Chapter 4, the design parameters for the aerosol-LIBS system were determined and the system was tested using an aqueous media. Chapter 5 focuses on the design changes, shakedown, and actual testing of the aerosol-LIBS system using $CeCl_3$ in 500°C molten salt. Chapter 6 of this dissertation provide information and discussions on the aerosol-LIBS testing and results using UCl_3 and an assessment of the overall approach for LIBS in the ER. In Chapter 7, the key points from the dissertation are summarized and recommendations and future work are presented. Appendices A, B, and C contain MATLAB programs developed to process the spectral data, the aqueous static surface experimental results, and the electromagnetic pump development, respectively.

Chapter 2

Literature Review

2.1 LIBS in Actinides

Significant challenges exist when performing LIBS with a heavy element, notably the spectral interferences due to the density of the spectral lines. Wachters and Cremers[19] were among the first (1987) to use LIBS to study uranium (U). In this work, they studied U in a nitric acid solution that was contained in a horizontal vial to prevent lens damage from splashing. Their results of their study showed that LIBS was capable of performing quantitative analysis on a heavy element like U in solution. Sarkar and co-workers[25, 26] also studied U in a solution form. However, rather than performing the LIBS analysis directly in the liquid, the authors dried the samples onto a substrate (filter paper[25] or graphite surface[26]) prior to measuring the sample. Singh and co-workers[27] studied U, Pu, and Np in aqueous solutions. The Pu and Np in the solution were dried onto a carbon rod and detected on the surface using LIBS and the strongest lines were identified. For U, the sample was nebulized using an ultrasonic nebulizer and LIBS was conducted in the aerosol using a gate delay of 30 μs. Results yielded a LOD of 1,359 ppm U using the 409.013 nm line. The above studies demonstrate the capability of LIBS to detect U in aqueous solutions despite spectral interferences and challenges of working with liquid samples.

Not only have actinides been quantified using LIBS in solutions, extensive work has been done in other sample configurations. Sirven et al.[28] used LIBS to determine the geographical origin of yellow cake. Here the yellow cake samples were mixed with grease

to form a paste in which the LIBS analysis was done. Results in their study showed that the origins of the yellow cake samples could be determined in all 11 cases. Chinni and co-workers[18] were able to measure U in soils using a standoff approach showing that uranium could be detected in trace quantities via this method. Judge et al.[29] demonstrated the measurement of U and Th in powder form as well as in uranium ore. The research team was able to identify these elements despite the large matrix effects due to working in an ore sample. Fichet et al.[30] studied the detection of impurities in UO_2 and PuO_2 powders. Here, up to 21 impurities in the sample matrix were studied and identified down to 100 ppm with %RSD between repetitions being on the order of 10%. Zheng et al.[31] measured PuO_2 residues using LIBS. Overall, these reported studies show that LIBS is versatile and capable of determining subtle impurities even in high matrix samples.

LIBS has also been used to measure oxide fuel components for fuel fabrication quality control. Sarkar et al.[32] performed a LIBS study using mixed U and Th oxide fuel pellets. Here, the authors performed an optimization study to determine key LIBS parameters for U and Th in solid oxide fuels. Barefield and co-workers[33] studied several mixed oxide fuels including UO_2, PuO_2, AmO_2, and NpO_2; these authors used a high resolution spectrometer and were able to identify elemental peaks with very little interference.

A number of other authors used a high resolution spectrometer to measure the isotope ratios of U and Pu. Smith et al.[34] was able to resolve the isotopic shift between Pu-239 and Pu-240. Doucet and co-workers[35] were able to determine the isotope ratios of U-235 and U-238 along with the ratios between hydrogen and deuterium via LIBS analysis. However, high resolution LIBS comes with a trade-off of spectral intensity. Tampo et al.[36] explored a microwave-assisted LIBS method to improve the intensity of the spectra while operating with a high resolution spectrometer. In this study, Gd was used as a surrogate and results indicate that the plasma can be significantly enhanced. Emmert et al.[37] also studied methods for enhancing actinide measurement enhancement. Here, depleted uranium samples were explored using nanosecond and femtosecond laser pulses. Results indicated the

femtosecond laser pulses could help overcoming challenges with heavy element analysis and could significantly increase sensitivity.

2.2 LIBS in LiCl-KCl Salts

2.2.1 Molten Salt

To enhance the material accountability and safeguards of the special nuclear materials used in pyroprocessing, a number of studies have been conducted using LIBS in a molten salt. Andrew Effenberger[8] was among the first to demonstrate LIBS analysis in a molten LiCl-KCl salt by using a static surface approach. In the static surface approach, the laser is directed downwards onto the top surface of a static or non-moving liquid surface. In Effenberger's work, $CrCl_3$, $CoCl_2$, and $MnCl_2$ were studied in the molten salt matrix at 773 K with the concentrations ranging between 0.3 wt% and 2.5 wt%. This work showed that LIBS analysis in the molten salt was feasible and that limits of detection (LOD) down to 0.3 wt% could be achieved.

Hanson and co-workers[9, 38] performed an in depth LIBS study of $CeCl_3$ and $MnCl_2$ in LiCl-KCl salts at temperatures ranging from 523 K (solid) to 773 K (liquid) using the static surface configuration. Here, the concentration range studied was between 0.1 wt% Ce to 1 wt% Ce. Results of the study showed that, in general, the molten samples had less self-absorption and lower relative standard deviations than the solid samples.

Weisberg et al.[10] also studied a molten LiCl-KCl salt with additives of $EuCl_3$, and $PrCl_3$ using the static surface approach. The concentration ranges studied were between 0 and 1 wt% for Eu and 0.1 wt% to 1 wt% Pr. In this work, a thin film was observed on the top surface of the salts containing Eu and Pr but not on blank (LiCl-KCl) samples. The composition of the film with respect to the bulk was not reported; however, the presence of the film influenced the shot-to-shot results since a plasma formed on the liquid surface differed from those formed on the solid film surface. To address this issue, the authors

used conditional analysis to eliminate large shot-to-shot fluctuations within the collected spectra, thus effectively grouping shots that fell only on the liquid surface. In addition to the conditional analysis, a partial least squares (PLS) method was used to obtain qualitative and quantitative results. Specifically, the absolute root mean square error of prediction (RMSEP) was reported to be 0.13% within the range studied for both Eu and Pr.

More recently, Smith and co-workers[11] from the Argonne National Laboratory have designed a probe that can be used to remotely analyze the static surface of the molten salt within a glovebox environment. Feasibility studies using the probe have been done to measure U, Pu, and Np in the LiCl-KCl salt. Conclusions from this study is that optical degradation occurs over time and provision to change optics without effecting the alignment is needed.

The above studies demonstrate LIBS analysis in a molten salt matrix, however, significant challenges still exist as a result of the static surface configuration used, namely with respect to splashing, optical degradation, and sample homogeneity. For LIBS to be effective for molten salt compositional analysis in the ER, these issues must be addressed.

2.2.2 Solid Salt

One approach to improve material accountability and safeguards within the ER and to reduce many of the challenges of working with a liquid sample is to extract the salt prior to LIBS analysis. Bryce and co-workers[39] have explored a solid salt configuration to explore Ce and Gd in LiCl-KCl salt. Here, the salt was drawn from the melt in a 4 mm diameter pyrex tube where it froze. This salt was extracted and placed in a 25 mm diameter sealed jar. With this setup, significant dust formation occurred after 100 shots and %RSD values were poor. However, by normalization using a Li peak, the signal could be improved significantly; the results show that an LOD can be achieved down to 1,800 ppm Gd.

Kim et al.[40], studied solid UCl_3-LiCl-KCl salt with concentrations of UCl_3 ranging from 0 wt% to 10 wt%. In this work, the U 502.73 nm line was normalized using the Li

497.16 nm line. With the normalization, the %RSD was 1.65% between the repetitions. Univariate calibration curves were made with an R^2 value of 0.985 and a root mean squared error (RMSE) of 0.141 wt% or 1,410 ppm. A method for extracting the salt from the ER was not addressed in this study.

Yoo et al.[41] and Kim and co-workers[42] explored a method to extract a solid sample from the ER for LIBS analysis. Here, a gas cooled mandrel is dipped into the salt to form a thin frozen layer of salt. The mandrel is then extracted revealing a solid layer of salt for LIBS sampling. By shooting the frozen salt at different axial locations, the salt compositions can be determined at different salt depths. Results from multiple shots indicate variation in the salt composition; that is, depth profiling of the frozen salt revealed non-homogeneous behavior.

Whereas the above studies have demonstrated significant potential, repeatability and optical degradation issues occur as a result of dust formation. Extracting salt from the ER for analysis adds a sample preparation step which has the potential to increase delay between sampling and data acquisition. Another potential concern is homogeneity of the sample. Several authors have reported that separation and non-homogeneity effects exist in salt freezing from the molten phase[43–47]. Granted, the freezing rates in these studies were slow; however, it introduces a variable that must be addressed in a solid salt LIBS approach. In addition, Hanson and co-workers have shown that, in general, better results are acquired from a molten phase[9, 38]. As a result of these findings, solid salt analysis may not be ideal for near real-time salt analysis in the ER.

2.3 LIBS in Liquids and Aerosols

It has been shown that LIBS can effectively measure actinides in a number of phases as well as determine material compositions in molten and solid salts. Of the liquid analyses conducted, nearly all used a static surface configuration with the exception of Singh and

co-workers[27]. In this section, other liquid LIBS configurations are explored and assessed in order to identify configurations more likely to mitigate challenges of a molten salt LIBS measurement within the ER.

There are several main approaches or configurations for LIBS in liquid samples; these are (1) static surface analysis as described above, (2) subsurface bulk analysis, (3) jet analysis, and (4) aerosol stream analysis. The static surface analysis approach is conceptually the easiest of the different methods; however, with this approach, liquid splashing as a result of the plasma shock-wave becomes a significant challenge. Wachter and Cremers[19] used a horizontal glass vial to mitigate some of the effects of splashing. Here, the splashed material would hit the upper curved portion of the vial and roll back down into the bulk of the liquid. St-Onge and co-workers[20] conducted a static surface analysis to measure sodium chloride. The effects of splashing were somewhat mitigated by using a long focal length (400 mm). However, the authors noted that after multiple laser shots the liquid level within the test crucible declined. In addition, the formation of bubbles on the static surface influenced the repeatability of the results. Barreda et al.[21] also performed work using a static surface and noted that the shot-to-shot frequency is low due to the time required for the liquid surface to calm between shots.

In addition to the aqueous and molten salt cases above that use a static surface configuration, other cases involving molten materials were identified. Yun and co-workers[48, 49] explored a molten borosilicate glass mixture to enhance material accountability in the vitrification process of UNF using a static surface approach. In this study, a long (500 mm) laser focal length was used with a high resolution spectrometer ($\lambda/\Delta\lambda$ = 40,000). Calibration curves for Sr, Al, Ti, Ca, Mg, Fe, Nd, and Zr were determined. The effects of splashing and optical degradation were not mentioned. Gruber et al.[50] studied Cr, Ni, and Mg in a molten steel under reduced pressures. To reduce splashing, optics were flushed with gas and the incoming laser light was non-perpendicular to the surface. Results of the sampling were able to identify each of these elements quantitatively as well as detect the real-time addition

of other components such as Ti. The study was conducted over a two week period and no optical degradation was noted in the paper.

In a subsurface bulk analysis technique, the laser is focused through the liquid to create plasma below the surface of the liquid. Work has been done using this approach to measure compositions of liquid samples using single[51, 52] and double[51, 53] pulse systems. In the double pulse case, the first laser pulse creates a bubble and heats the sample and the second pulse creates the plasma within the bubble which greatly increases signal and repeatability. One of the key challenges of the bulk analysis technique is that a fairly transparent liquid is required in order to transport the laser to the desired plasma location and to collect the incident light from the formed plasma. Lucas et al.[54] filed a patent in 2005 for a novel molten LIBS approach similar to the double pulse approach. In this case, a gas is bubbled horizontally into the melt and the laser light is focused onto the interior surface of the bubble through the gas feed line. The results for this configuration were shown for a number of melt materials including Cu, Al, Fe, and Zn. The advantage of this approach is that it does not require a transparent liquid and surface films can be avoided.

Another liquid-LIBS configuration incorporates a liquid jet stream. In this scenario, the laser light is focused onto the surface of the liquid jet to create the plasma. Cheung and Yeung[53] were among the first to explore this method and found that low LOD values could be achieved. Kumar et al.[55] and Feng et al.[56] studied the effect of the jet thickness and overall optimization of the system and found that the processes is highly repeatable. Yaroshchyk and co-workers[57] compared a liquid jet system to a static surface system and found that the LOD for the jet case were in general 4 times lower. This observation in part, is due to a continuous flow—thus reducing the splashing effect. In addition, the shot-to-shot frequency is not limited by surface perturbations. The disadvantages of this system are material clogging in the jet and the large throughput to maintain the jet.

Another potential method is to use a LIBS-aerosol measurement technique[23]. In this approach, the laser is focused within an aerosol gas stream to create the LIBS plasma.

This technique is often used for online monitoring of environmental air samples for toxic metals[58–62]. In these cases, the aerosol concentration within the gas stream is low, leading to high shot-to-shot variation as a result of low probability of particle interaction with the plasma. Diwakar and co-workers[61] have shown that the plasma-particle interaction can be defined by Poisson modeling statistics. As a result, this supports the conditional analysis technique for excluding shots below a certain threshold.

In many cases, the aerosol is generated from a liquid sample via an aerosol generator. Here, the aerosol concentration within the gas stream can be sufficiently high as to reduce the probability of shots containing no particles; however, significant shot-to-shot variation is still observed. Huang and co-workers[62, 63] observed that the shot-to-shot variation could be large due to fluctuations in the number of aerosol particles consumed per plasma volume. Poulain and Alexander[64] as well as Schechter[65] observed the shot-to-shot variation in liquid aerosols and concluded that the variation can be attributed to (1) the number of particles within the plasma volume, (2) the location and size of the particles within the plasma, and (3) the liquid droplet interference with the incoming laser light. As a result, Schechter[65], developed a basic algorithm to perform conditional analysis on the collected spectra to reduce variation prior to ensemble averaging. Using the above conditional analysis scheme, Schechter was able to significantly improve the sensitivity of the system.

Despite challenges with particle-plasma interactions and interference, LIBS analysis from liquid aerosols has been shown to perform well. Kumar et al.[66] used a Meinhard nebulizer to generate an aerosol and found that the aerosol approach yielded better results than a liquid jet method. They concluded that this in part was due to better utilization of the laser energy to ionize the sample in the aerosol stream, whereas much of the laser energy was used to first vaporize the sample in the liquid jet case. Martin and Cheng[67] measured chromium in water and reported LOD for Na down to 400 ng/dscm. Cahoon and Almirall[24] measured the concentrations of Sr, Ba, Mg, and Ca in water using both an aerosol and micro-droplet approach. Here, both methods resulted in ultralow detection limits with %RSD on the order

of 1%. Alvarez-Trujillo and co-workers[68] performed stand-off LIBS in a liquid aerosol and determined that they could detect Na down to 55 ppm in water at 10 meters away.

2.4 Liquid Configuration Selection and Approach

LIBS has been conducted in molten LiCl-KCl salts at high temperature. However, all of these molten salt LIBS studies were conducted using a static surface configuration which appears to be the least favorable from an analysis standpoint. However, the static surface approach is the easiest to implement and therefore will be tested in phase I of this project in order to gain understanding, insight, and experience. Of the other potential liquid analysis techniques, the bulk analysis technique is not a favorable option due to the transparency requirement and the bubble approach has been patented. Between the jet and aerosol configurations, the aerosol approach appears to be capable of greater signal intensity and sensitivity due to increased laser energy utilization. As a result, the liquid jet configuration will not be considered further in this work.

In measuring molten salts in the ER, the aerosol sampling approach offers several additional advantages over the current static approach. Using an aerosol method, the liquid sample can be drawn continuously from the bulk of the salt, reducing variation due to non-homogeneity. In addition, since splashing, bubble formation, and surface perturbations are not an issue with the aerosol approach, the frequency of the sampling system is less limited. Lastly, the laser energy is better utilized to ionize the sample. Due to these advantages, it has been proposed to use this approach to measure molten salt. To date, the high temperature aerosol generation of molten salts has never been reported.

Chapter 3

Equipment and Methodology

3.1 Experimental Equipment

This work was done using a Neodymium Yttrium Aluminum Garnet (Nd:YAG) laser (Q-smart 450) from Quantel USA. Figure 3.1 shows a picture of the Q-smart 450 laser used. This laser is a solid state laser with the flashlamp excitation operating at 10 Hz. The Q-switch divider controls the lasing frequency while still operating at the optimal flashlamp frequency in order to deliver optimal beam characteristics. The output wavelength of Nd:YAG lasers is 1064 nm; however, in this work, the laser light was frequency doubled to achieve the second harmonic at 532 nm. The Q-switch delay for this laser was factory optimized at 6 μs, resulting in a peak laser energy of approximately 450 mJ at 1064 nm or 250 mJ at 532 nm. Adjusting the Q-switch delay changes the laser energy; by increasing the Q-switch delay, the energy decreases. However, the laser energy becomes less stable below 50% of its maximum energy. In order to maintain a stable laser energy at levels below 50% of max, a beam attenuation module was installed. With this addition, the Q-switch delay was left at the optimal value and the laser energy was controlled via the beam attenuator. This resulted in better stability despite the laser energy level. Even so, Nd:YAG lasers have fairly high shot-to-shot variation in the laser energy itself, typically on the order of 3 to 5%. This variation constitutes one of the largest spectral variations in LIBS using a Nd:YAG laser. To measure the laser energy, a power meter and monitor were purchased from Gentec EO. The MAESTRO power monitor and meter are shown in Figure 3.2.

Figure 3.1: Picture of the Q-smart 450 Nd:YAG laser used in this work.

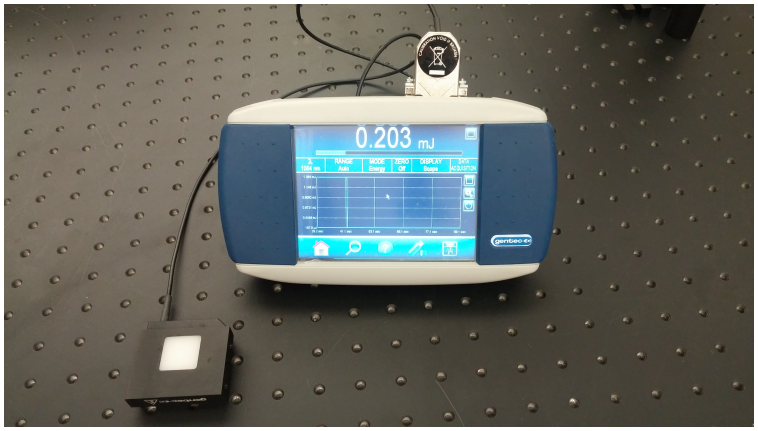

Figure 3.2: Picture of the laser power meter used to determine the laser energy.

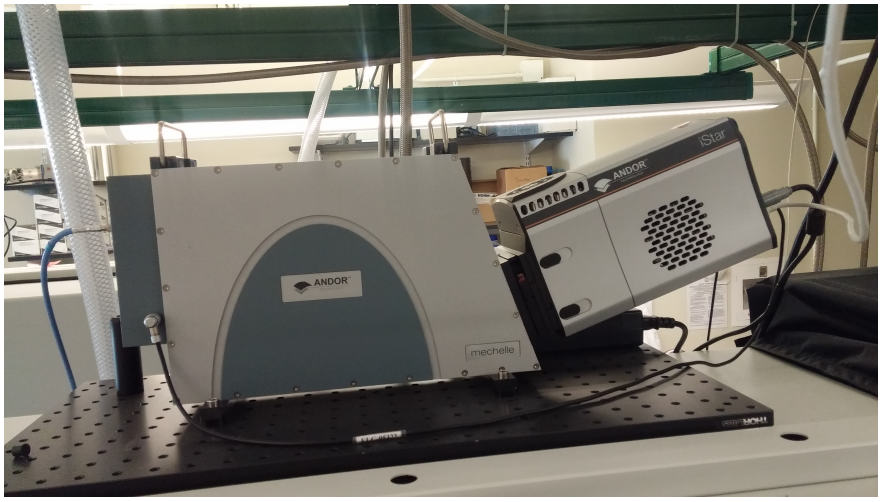

Figure 3.3: The Andor Mechelle 5000 spectrometer with iStar ICCD camera.

Light collected from the LIBS plasma was carried to the spectrometer via a fiber optic cable from Ocean Optics, Inc. The fiber optics used had 50 μm cores and were 2 m long and 4 m long for the aqueous and molten salt experiments, respectively. The fiber transmission between 450 nm and 900 nm was approximately 75%. Between 280 nm to 450 nm the transmission varied almost linearly from 5% up to 75%. As a result, signal below 450 nm is reduced due to poor light transmission.

The spectrometer used was the Mechelle 5000 from Andor Technologies. This spectrometer is an echelle type that uses a grating system to disperse the incoming light into their respective wavelengths to create an echellogram (stacks of spectra) on the detector. As a result of these stacks, a larger spectral range can be obtained with high resolution within a single detector. In this instrument, the spectral wavelength range is 200 nm to 975 nm with a spectral resolution ($\lambda/\Delta\lambda$) of 4,000 at 435 nm. The aperture is F/7 with a focal length of 195 mm. The slit width was 10×50 μm. A picture of the Mechelle 5000 spectrometer is shown in Figure 3.3.

Also shown in Figure 3.3 is the detector (iStar 334T Gen II, Andor Technologies, Inc.) that has been coupled with the spectrometer. This detector is an intensified charge-coupled device (ICCD). In a normal CCD camera, incoming photons are incident onto a 2D semi-

conductor array with each region representing a pixel. As a photon strikes a given pixel area, electrons from the semiconductor are knocked out and are stored in a capacitor. The charge created is proportional to the photon intensity. After the array has been exposed to an image, a shift register dumps the charge from the capacitors through a charge amplifier to convert it into a voltage. The resulting matrix of voltages can then be used to recreate the image digitally. An ICCD camera intensifies the incident light before it enters the CCD detector. The intensifier usually consists of a photocathode, a micro-channel plate (MCP), and a phosphor screen. As light from the spectrometer strikes the photocathode, photoelectrons are generated. Due to an applied potential, the photoelectrons are accelerated towards the MCP which causes photoelectron gain. At the phosphor screen the photoelectrons are converted back into light which then enters the CCD. The intensifier can act as a shutter by reversing the voltage that is applied between the photocathode and the MCP. This feature is advantageous for LIBS because it results in fast shutter times. The ICCD used in this work has a quantum efficiency of 15% and has 1024×1024 active pixels with an effective pixel size of 13×13 μm.

Built into the iStar 334 ICCD detector is a digital delay generator (DDG). The DDG is essential in order to control the precise timing required for LIBS. As discussed in Chapter 1, the detector must be gated in order to reduce or eliminate the continuum background light. The built-in DDG of the iStar detector can control the timing in two basic ways: (1) it externally triggers the laser and then gates the detector accordingly or (2) it receives an impulse from the laser and then starts the timing. In this work, the DDG and other equipment are operated in mode 2.

Experiments and salt preparation were conducted within an inert atmosphere glovebox purchased from Innovative Technology. This glovebox operates using argon gas and maintains the O_2 and H_2O levels down to 0.1 ppm. A custom-made quartz window (15×15 cm) was added to allow easy transport of the laser light into the glovebox. External features of the glovebox were modified to allow for the installation of a breadboard for laser mounting

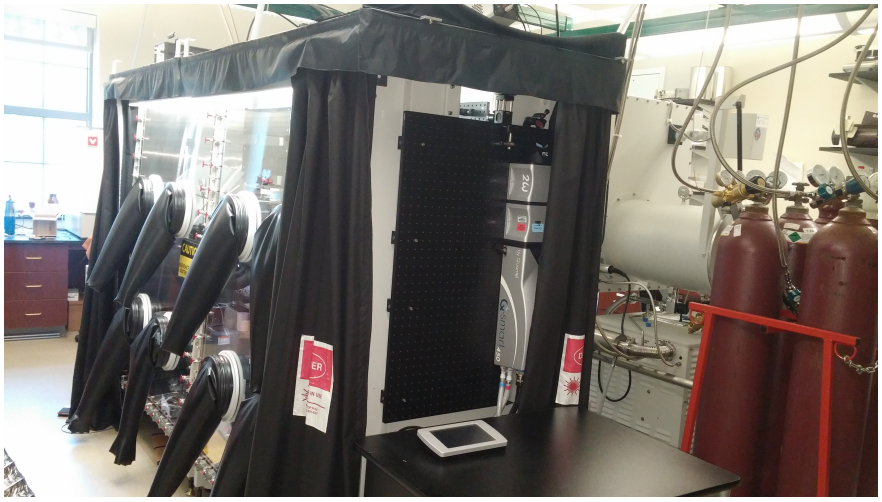

Figure 3.4: Inert atmosphere glovebox used in these experiments with laser blackout curtains.

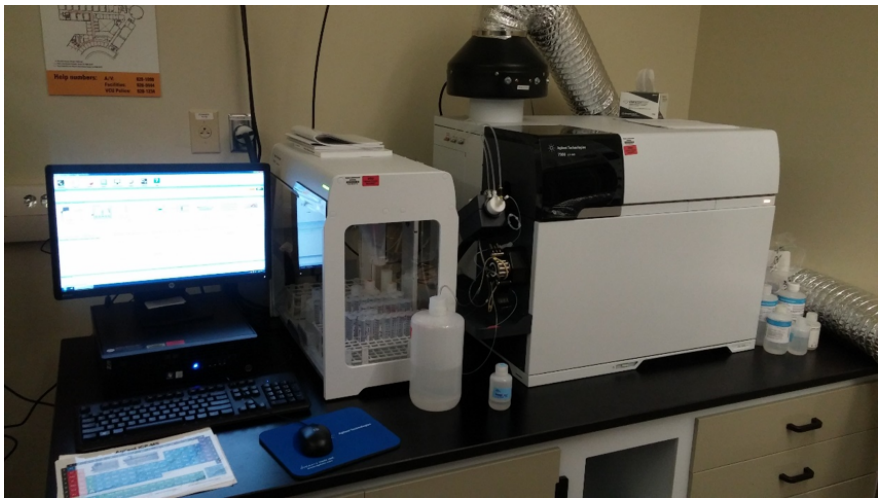

Figure 3.5: Agilent 7900 ICP-MS mass spectroscopy system used for sample validation.

and laser blackout curtains. A picture of the glovebox with the laser mounting and curtains is shown in Figure 3.4.

Samples measured with LIBS were verified using ICP-MS using a 7900 model ICP-MS from Agilent Technologies. This instrument is shown in Figure 3.5 along with the SPS 4 autosampler.

3.2 Spectral Analysis

Analytical figures of merit (FOM) provide a method to assess the performance of a particular analytical method in a standardized way. There are many FOM; however, the main ones are the precision, accuracy, and limits of detection (LOD) of the system. Other factors that feed into the aforementioned FOM's are peak selection, normalization, and calibration curves. This section will address methods used in this dissertation to assess the FOM for LIBS.

3.2.1 Peak Selection and Quantification

In order to perform qualitative and quantitative analysis using LIBS, appropriate spectral lines must be identified. Every element has numerous potential spectral lines between the different neutral and ionization states which form a "fingerprint" for that element. If strong spectral lines for a given element are present in the spectra and there is low interference for these peaks, then it can be shown that this element is contained in the sample. For quantitative analysis, careful selection of spectral peaks is necessary to obtain the strongest lines and to reduce spectral interference. The relative intensity between the spectral lines for a given element is a function of the gate delay, plasma energy, and matrix effects. These complicate the approach; however, there are usually multiple lines that can be used and methods to compare between lines are available. Peaks with low interference with nearby lines and a strong signal intensity with respect the background are desirable. Both can be determined visually; however, methods to quantify and compare between spectral lines is the signal-to-background ratio (SBR) and the signal-to-noise ratio (SNR)[58]. These quantities are defined below:

$$SBR = \frac{Peak\ intensity}{Background\ intesity\ near\ the\ peak} \tag{3.1}$$

$$SNR = \frac{Peak\ Area}{RMS\ noise \times Peak\ width} \tag{3.2}$$

where *RMS noise* is the root mean squared noise (or standard deviation of the noise). The *background intensity near the peak* is the intensity at the base of the peak. With these metrics, peaks can be compared to identify lines that are the strongest. The SBR is slightly simpler to compute, and in most cases yields similar results. Consequently, the SBR will be used in this dissertation as part of the peak selection process as well as optimizing different parameters such as the gate delay, laser energy, and nebulizer pressure.

To quantify the amount of a given element in the material, the strength of the line or intensity must be determined and compared to samples at different known compositions. The two common methods used to determine the peak strength are the maximum peak intensity of the line and the peak area as shown in Figure 3.6. The peak area of the peak is determined as the area under the curve minus the background. A number of approaches can be used to subtract the background; in this case, the background area is simply subtracted from the total area to get the peak area. A graphical user interface (GUI) function was written in MATLAB to determine these spectral values. In these programs, the peak region of interest is displayed and the user identifies the peak starting wavelength and ending wavelength by clicking the plot. With these values, the maximum intensity, peak area minus the background, the SBR and the SNR can be determined. These programs called, "Data_Analysis" and "FindXPeak" can be found in Appendix A.

3.2.2 Precision and Normalization

A key FOM is the precision of the analytical approach. In order to identify the precision of the measurement, multiple repetitions of every sample are taken. The standard measurement to demonstrate the precision of the signal is the percent relative standard deviation (%RSD). The %RSD between repetitions is calculated using[70]:

$$\%RSD = 100 \times s/M \tag{3.3}$$

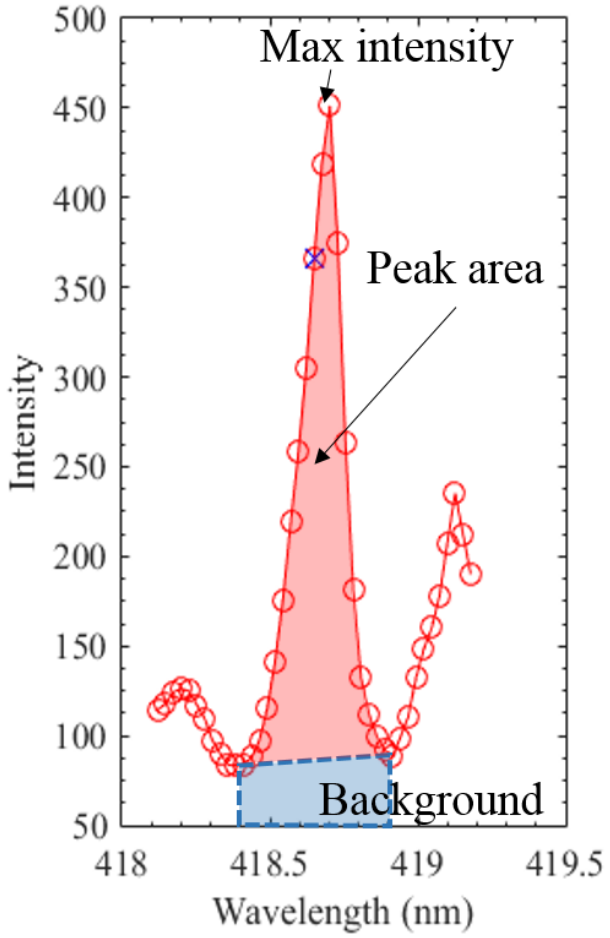

Figure 3.6: Example demonstrating the two methods (peak area and max peak intensity) to quantify intensity of a spectral peak. The blue x shown is the line wavelength reported in NIST[69].

where s is the standard deviation and M is the mean between repetitions. The standard deviation between the repetitions is calculated by[70]:

$$s = \left[\frac{\Sigma(r_i - M)^2}{n_r - 1}\right]^{1/2} \tag{3.4}$$

where n_r is the number of repetitions and r_i a given repetition. The lower the value of the %RSD, the more precise the measurement. In this dissertation the %RSD is used in two ways: (1) the entire spectrum between repetitions is compared to get a general feel for the repeatability and (2) the individual peak parameters are compared. The %RSD for both methods were computed in the MATLAB programs shown in Appendix A.

In many cases, the precision of the measurement can be enhanced by using an internal standard or a normalization technique. The LIBS spectral intensity can vary significantly from shot-to-shot due to fluctuations in the laser energy, optical degradation or a number of other reasons. Often an internal standard is used to reduce this variation[71]. In this case, an element is added to the samples at a constant concentration. Since the concentration is known, normalizing with respect to the element's spectral response will reduce variation in the spectra from shot-to-shot. Normalization is also an important tool to reduce systematic changes in the signal over time. In spectral analysis, the most common normalization scheme is to divide the peak intensity of interest by the intensity of the internal standard. In this work, this approach is used to normalize the entire spectrum with respect to an internal standard before using the GUI to identify peak characteristics.

3.2.3 Calibration Curves

Once the peak intensity has been determined for a number of samples, a calibration curve can be made. A calibration curve is the relationship between the concentration of the sample and the analytical response (peak area, intensity, etc.). The response region of greatest interest for analysis is the section where the spectral response varies linearly with the concentration.

The slope of this linear section can be found using linear regression. With this approach, the slope of the line is[72]:

$$b_1 = \frac{\Sigma[(x_i - \bar{x})(y_i - \bar{y})]}{\Sigma(x_i - \bar{x})^2} \tag{3.5}$$

where b_1 is the slope, x_i is the concentration at a given point, y_i is the response at a given point, $\bar{x}$ is the mean of all the concentration values, and $\bar{y}$ is the mean of the detector responses. The y-intercept of the linear regression line is determined by:

$$b_0 = \bar{y} - b_1\bar{x} \tag{3.6}$$

where b_0 is the y-intercept. The R value is determined by[72]:

$$R = \frac{\Sigma[(x_i - \bar{x})(y_i - \bar{y})]}{\sqrt{\Sigma(x_i - \bar{x})^2\Sigma(y_i - \bar{y})^2}} \tag{3.7}$$

The coefficient of determination (R^2) is the standard measure for how well the data correlates with the regression line. The R^2 value is simply the square of R and values closer to unity indicate a stronger linear trend.

The standard deviation $S_{y/x}$ in the y direction for the regression line is calculated using[73]:

$$S_{y/x} = \sqrt{\frac{\Sigma(y_i - \hat{y}_i)}{n_r - 2}} \tag{3.8}$$

where $\hat{y}_i$ is the value from the regression line (the residual is $y_i - \hat{y}_i$). This quantity is very similar to the root mean squared error (RMSE), the only difference is that the $(n_r - 2)$ is changed to $(n_r - 1)$. Typically the larger of the two numbers are reported. The uncertainties, or standard deviations for the slope and y-intercept can be determined using Students t value ($t_{95\%}$), typically at 95%. The uncertainties can be combined to form upper and lower confidence intervals for the regression line. The confidence interval (y_{CI}) of the regression

curve is shown below.

$$y_{CI} = \hat{y}_i \pm t_{95\%} S_{y/x} \sqrt{\frac{1}{n_r} + \frac{(x_i - \bar{x})^2}{\Sigma (x_i - \bar{x})^2}} \tag{3.9}$$

In addition to the confidence interval, prediction intervals can be determined. The prediction interval, calculated with $t_{95\%}$ represents the region where 95% of the data should exist on the curve. The prediction interval is shown below[73].

$$y_{PI} = \hat{y}_i \pm t_{95\%} S_{y/x} \sqrt{1 + \frac{1}{n_r} + \frac{(x_i - \bar{x})^2}{\Sigma (x_i - \bar{x})^2}} \tag{3.10}$$

A MATLAB program ("Calibration Curves", Appendix A) was developed to plot the concentration and response data along with the confidence and prediction intervals.

3.2.4 Limits of Detection, Cross Validation, and Accuracy

The LOD for a specific analytical approach can be determined from the calibration curve and represents the smallest amount of a material in a sample that can be detected with reasonable certainty. The LOD is calculated using[71]:

$$LOD = \frac{3\sigma_b}{b_1} \tag{3.11}$$

where σ_b is the standard deviation of the blank measurements. In some cases, blank measurements were not available, in which case the standard deviation for the lowest standard was used. By using "3" in Equation 3.11, the LOD is the minimum amount of material that can be measured at 33% confidence. One of the biggest factors determining the LOD is the slope of the calibration curve, which is a determination of the measurement sensitivity to changes in concentration. A steeper curve means that the element is more sensitive and better analytical results can be achieved.

Cross validation techniques are used to explore how well a calibration curve performs with unknown samples. In a cross validation approach, data points not used in the calibration

are predicted. There are many different cross validation methods, two methods used in this dissertation are venetian blinds and leave one out cross validation (LOOCV). In venetian blinds, not every data point in the calibration is left out but only every"ith" point. This results in a certain number of splits and a percentage of the data being used in the cross validation. In LOOCV, each data point is systematically left out to assess the error of calibration. The standard measure of this error is the root mean squared error of cross validation (RMSECV). The equation for the RMSECV is shown below[74]:

$$RMSECV = \sqrt{\frac{\Sigma(x_{i,atv} - x_{i,CV})^2}{n_s}} \tag{3.12}$$

where $x_{i,atv}$ is the accepted true value or reference value, $x_{i,CV}$ is the predicted value from the cross validation, and n_s is the number of cross validation points used. The RMSECV is a comparison between the actual concentration and the predicted concentrations of the samples used in the cross validation. The RMSECV is a measure of the error estimate for unknown samples obtained at the same time as the calibration data.

Accuracy is an important FOM of any analytical system because it determines how well the analytical approach and calibration curve can predict the sample composition. One method to determine the accuracy, or the estimated error of the calibration curves is the root mean squared error of prediction (RMSEP). In this case, the formula is exactly the same as the RMSECV; however, rather than using the predicted values from the cross validation, independent samples are analyzed and the predicted concentrations are used in the formula. This method provides an overall estimate of the error for the curve. Another method to determine the accuracy is to compare the predicted or measured concentrations (x_m) to the reference value individually. The residuals or error between the measured and reference values is expressed as $x_m - x_{atv}$ and the percent error[71]:

$$\%\ Error = \left[\frac{x_m - x_{atv}}{x_{atv}}\right] \times 100 \tag{3.13}$$

The accepted true values for the samples used in this work were determined using ICP-MS. The value of x_m for unknown samples is found using the slope and y-intercept of the calibration curve combined with the measured spectral response (y_m). The uncertainty of the measurement (S_{xm}) can be determined using[73]:

$$S_{xm} = S_{y/x}\sqrt{\frac{1}{n} + \frac{(y_m - \bar{y})^2}{b_1^2 \Sigma (x_i - \bar{x})^2}} \tag{3.14}$$

Again the Student t value is used to calculate the uncertainty of the measurement. In this case, the concentration for the sample would be $x_m \pm t_{95\%} S_{xm}$. Often, unknown samples are not available to directly determine the accuracy of the analytical setup; however, in these cases, the accuracy can be approximated using the LOOCV. A drawback to this approach exists when few calibration points are used because the linear regression line may vary depending on the point left out. Typically six calibration points are needed to form a good calibration curve[71].

3.3 Univariate and Multivariate Calibration Methods

The univariate calibration technique has been the standard approach because of its simplicity. Here, only one aspect or variable from the spectra is used to generate the calibration curve. The above section introducing calibration curves and methods is an example of the classical univariate approach. In this work, calibration curves were made using a single peak from the element of interest. Whereas this approach is easy to implement and yields good analytical results for simple sample matrices, the results can be poor when complex, multi-component samples are studied.

An additional calibration approach stems from the emerging area of complex spectral analysis called chemometrics. Chemometrics is the application of mathematical models and statistical principles in analytical chemistry. Using chemometrics to perform multivariate analysis, the maximum amount of useful information about a sample can be obtained be-

cause more variables can be considered simultaneously. In fact, a single LIBS spectra can contain thousands of spectral intensity data points (variables) which can be modeled using chemometrics. There are many chemometric models that are useful for LIBS analysis including[71]: discriminant functional analysis (DFA), linear discriminant analysis (LDA), principle component analysis (PCA), partial least squares (PLS), and artificial neural networks (ANNs).

Specifically important for developing multivariate calibration curves is the PLS method[74–81]. In this dissertation, only the PLS method has been used to analyze the LIBS data. The basic structure and equations for PLS will be summarized below[82–85]. PLS uses a matrix X of independent variables (spectra) and a vector Y dependent variable (concentrations) to develop and train a model that can be used to predict the concentration of n unknown samples. The size of X is $(n \times m)$ where n is the number of samples/repetitions and m is the number of spectral data points. Y is $(n \times 1)$. PLS is an iterative process which finds the latent variables (T matrix) that can model X while predicting Y. This is shown in the following matrix forms:

$$X = TP^T \tag{3.15}$$

$$\hat{Y} = TBC^T \tag{3.16}$$

where $\hat{Y}$ is the predicted concentration and P and C are the loadings or weights of X and Y, respectively. This can be re-arranged to get:

$$\hat{Y} = TBC^T = XB_{PLS} \tag{3.17}$$

with

$$B_{PLS} = P^{T+}BC^T \tag{3.18}$$

where P^{T+} is the so called Moore-Penrose pseudoinverse of P^T. Matrix B contains the regression coefficients and is a diagonal matrix, and B_{PLS} contains the weighted coefficients.

In the first step of the iterative process, X and Y are set equal to X_0 and Y_0, respectively. The covariance (R_1) of X_0 and Y_0 is :

$$R_1 = X_0^T Y_0 \tag{3.19}$$

Singular value decompression is done on R_1 to produce singular orthogonal matrices W_1 and C_1 with a third matrix Δ_1 of corresponding values. The lowercase counter parts of these matrices represent the first vector in the matrix, as a result, the first latent variable of X is:

$$t_1 = X_0 w_1 \tag{3.20}$$

where t has been normalized to force $t_1^T t_1$. The projection of X_0 on t_1 is given by:

$$p_1 = X_0^T t_1 \tag{3.21}$$

Next, the least squares estimate of X from the first latent variable is given by:

$$\hat{X_1} = t_1^T p_1 \tag{3.22}$$

For Y, the first pseudo latent variable is:

$$u_1 = Y_0 c_1 \tag{3.23}$$

Reconstructing Y yields:

$$\hat{Y_1} = u_1 c_1^T \; or \; \hat{Y_1} = t_1 b_1 C_1^T \tag{3.24}$$

with

$$b_1 = t_1^T u_1 \tag{3.25}$$

where b_1 is a scaler and represents the slope of the regression of Y_0 on t_1. The last step of

the first iteration is to deflate $\hat{X_1}$ and $\hat{Y_1}$ by subtracting the original X_0 and Y_0 as follows:

$$X_1 = X_0 - \hat{X_1} \; and \; Y_1 = Y_0 - \hat{Y_1} \tag{3.26}$$

This iterative process continues until X is completely decomposed resulting in a diagonal matrix B_{PLS} with the regression coefficients. With B_{PLS}, the predicted concentration can be obtained from the spectral information X using Equation 3.17.

Typically when a PLS model is being developed, a training data set is used to develop the model which is then validated using a test set. The training set should contain data that was collected to include all sources of variation and conditions. The better the experimental conditions (i.e., the smaller the variation) the better the predicted model. As the model is developed using the training set, it is possible to over-fit the model by selecting more LV to reduce the RMSECV. The test data set is used to verify the model performance; as the number of LV increase, the RMSEP decreases to a minimum before increasing. The minimum RMSEP indicates the ideal number of LV, too few LV and the model is under-fit and with too many LV the model is over-fit.

Due to the number of samples available in this dissertation, it was not possible to have independent samples for the training and validation data sets. As a result, sample repetitions were split to form the training and validations sets. The danger with this is that the two sets will be nearly identical. This leads to a scenario where the model can be over-fit since the RMSECV and the RMSEP will have a similar modeling response.

Due to the complexity of PLS modeling, a commercial software package that operates in the MATLAB environment was purchased called PLS_toolbox from Eigenvector Research. The repetitions measured per sample were divided between the training and validation sets.

Chapter 4

Aerosol System Design and Aqueous Testing

This chapter provided the discussion on a new LIBS system for exploring liquid aerosols in preparation for studying molten salts using an aerosol approach. The overall design concept and specifics of the design were addressed. In addition, initial testing of the designed system was done using an aqueous sample in order to gain insight into aerosol-LIBS detection and to work out challenges in the design and assess the system overall.

4.1 Early Experimental Design

4.1.1 Aerosol Generation

Liquid aerosol generation can be achieved in a variety of ways including Meinhard and ultrasonic nebulizers. However, many of these methods will not work for molten salts due to (1) the extreme operating temperature and (2) potential clogging of the system as salt flows through the tip aperture. However, one atomizer, called the Collison nebulizer (manufactured by BGI, Inc.), has been identified as a possible means of generating a molten salt aerosol. The Collision nebulizer is made entirely out of stainless steel; therefore, it can handle the high temperatures. In addition, the Collison nebulizer has reduced likelihood of clogging since the gas is passed through the nozzle aperture rather than the fluid. The fluid is drawn up into the gas stream as a result of a vacuum created by the compressed gas flow through

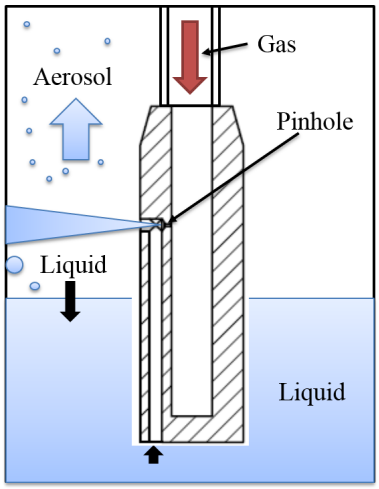

Figure 4.1: Illustration of how the Collision nebulizer works.

the nozzle (see Figure 4.1). As the gas and fluid mix in the gas stream, and also as the fluid impacts the nebulizer wall, an aerosol is being generated with particle sizes on the order of 2 μm (for a compressed air and water system). One key parameter influencing the aerosol generation of a fluid is the viscosity. K. R. May[86] investigated the performance of the Collison nebulizer with fluids ranging from 1 mPa·s (water) to 500 mPa·s (silicone mixture). Molten LiCl-KCl salt at 500°C has a viscosity of 210 mPa·s which is well within the range studied[87]. As other elements are added to the salt, the viscosities will change only slightly in comparison to the large range of viscosities studied for the Collison nebulizer. As a result, it is expected that the molten salt can be formed into an aerosol via the Collison nebulizer.

4.1.2 Basic Design Concept

An illustration of a molten salt-LIBS configuration using a Collison nebulizer is shown in Figure 4.2. In the first step, cold argon gas must be heated up to 500°C before entering the Collison nebulizer to prevent salt freezing during mixing. Next the gas must enter the Collison nebulizer to generate the molten salt aerosols. The argon flow and molten salt droplets then passes into a sampling chamber that can be viewed through quartz or sapphire sight windows. Through the windows, laser light is focused into the aerosol stream to create

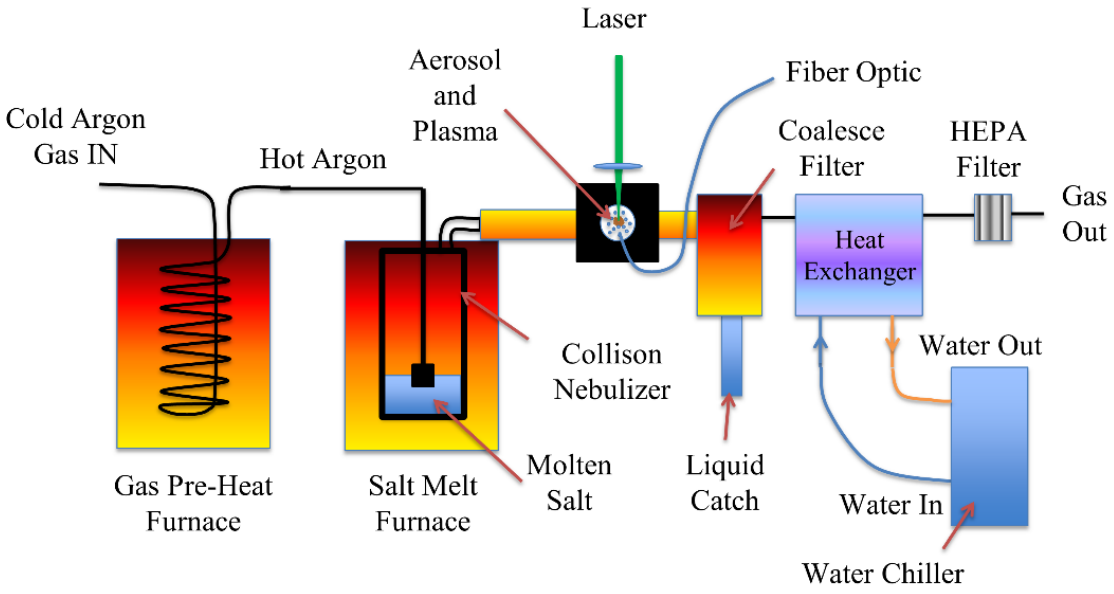

Figure 4.2: Illustration of the aerosol-LIBS setup.

a plasma. Optics and a fiber optic cable are positioned just outside the window at 90° from the incident laser to collect the spectral light generated as the plasma cools. The aerosol stream then passes into a coalescing filter, thereby removing the aerosol from the gas stream. The hot gas then passes through a heat exchanger cooling it down to a designed ambient temperature before being passed through a HEPA filter and vented out to the exhaust system. The following sections will discuss each aspect of this concept in detail.

4.1.3 Carrier Gas Heating

To prevent salt freezing during the aerosol generation, it is crucial that the input gas be at an operating temperature near 500°C, or at least greater than 350°C prior to entering the nebulizer. A simple heat exchanger system was made to fit inside a 1,350 W Kerr Lab

jewelers furnace with an inside cavity of 81 cm in diameter and 15 cm depth. A basic energy balance was done to determine if the Kerr Lab furnace was capable of heating the gas stream at the assumed maximum gas flow rate of 20 L/min (based on Collision nebulizer specifications). The amount of energy required to heat the gas was estimated to be 1,057 W. The available furnace was sufficient for this application.

An important parameter is the diameter of the tubing used for the coils of the gas heating the heat exchanger. At smaller diameters, the heat transfer within the tubing itself can be enhanced as well as an increased length of the tubing that can fit inside the furnace cavity. However, the pressure drop will increase as the tube diameter decreases. There are three available tubing sizes - 3.2 mm, 6.3 mm, and 9.5 mm diameters. The length of the tubing within the furnace cavity can be calculated by assuming the tubing is coiled like a spring at a diameter of 6.35 cm by 15 cm long (to be safe inside dimension of the cavity). Using the given information, the lengths are found to be 9.5 m, 4.75 m, and 3.2 m for the 3.2 mm, 6.3 mm, and 9.5 mm cases, respectively. The pressure drop between these systems was determined using[88]:

$$\Delta P = f\frac{l}{D}\frac{\rho v^2}{2} \tag{4.1}$$

where f is the friction factor, l is the tubing length, D is the inside diameter, ρ is the fluid density, and v is the fluid velocity. The only parameter that is unknown for these cases is the friction factor, which is a function of the surface roughness and the Reynolds (Re) number. The Re number was calculated to be 1.96×10^5, 5.98×10^4, and 3.5×10^4 for the 3.2 mm, 6.3 mm, and 9.5 mm cases, respectively at the max assumed flow rate of 20 L/min. Assuming a surface roughness of 0.000015 and using the Moody chart, the friction coefficients were tabulated. The resulting pressure drop was 8.4 kpsi for the 3.2 mm diameter tubing which is too high to be of practical use. The pressure drops for the 6.3 mm and 9.5 mm cases were 11.5 psi and 0.5 psi, respectively. Both the 6.3 mm and 9.5 mm diameter cases yield pressure drops that are sufficiently small to be applied to this application. Since the original intention was to build an in-house heating coil, the 6.3 mm diameter was selected due to

Figure 4.3: Photo of the heating coil manufactured in-house.

difficulty in bending the 9.5 mm diameter tubing.

The stainless steel heat exchanger designed above was made using the 6.3 mm tubing and is shown in Figure 4.3. The final dimensions for the heat exchanger were 7 cm in diameter and 14 cm long. The total length of tubing is 4.3 m.

4.1.4 Collison Nebulizer and Seals

The Collison nebulizer purchased from BGI, Inc. is shown in Figure 4.4. Basic components of the nebulizer are the jar, lid, tip, and inlet. The nebulizer can be purchased with 1, 3, 6, or 24 jet ports. In general, as the number of jets increase, the concentration (number density) of the aerosol increases. The amount of material used per jet configuration ranges from 1.5 ml/h to 66 ml/h in a water system. The 3 jet system was selected as a starting point because it is in the middle of the lower range. For the water system, the 3-jet system uses approximately 4.5 ml/h to 14.1 ml/h of sample depending on the input pressure of the gas. As the input pressure increases, the amount of material consumed also increases. For a

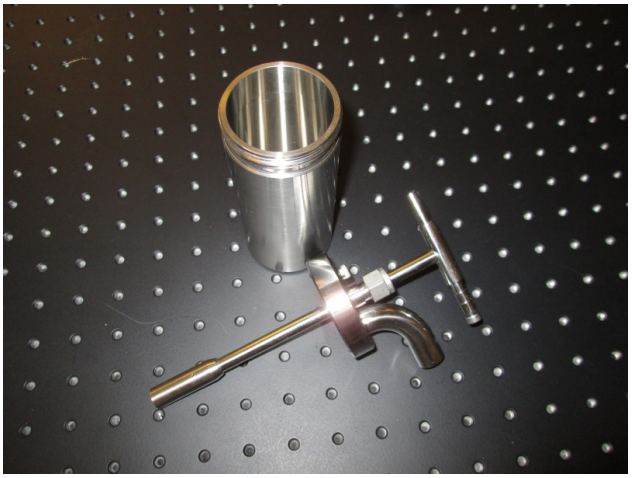

Figure 4.4: Photo of the Collison nebulizer.

water and air system, the recommended pressure range is between 20 psi and 100 psi. The pressure drop in the gas flow across the jets is substantial and will drop to the minimum pressure required to push the gas stream through the remainder of the system. As such, pressure measurements will be made at the inlet and outlet of the nebulizer to verify the actual pressure conditions of the aerosol generation.

The Collison nebulizer was constructed completely of stainless steel and therefore, should withstand the high temperature and corrosive environment proposed in this study. However, the unit had several Teflon and rubber seals that needed to be modified for the unit to function at high temperature conditions. Three seals were required and must be given a careful attention: (i) one between the inlet gas line and the lid, (ii) another between the lid and the canister, and (iii) one between the inlet gas line and the jet head. The seal between the gas line and lid could be easily fixed by replacing the Teflon ferrules in the Swagelok fitting with stainless steel ferrules. The seal between the gas line and jet head was also addressed by using a high temperature thread sealant called Deacon 770-L (stable up to 950°F (510°C)). The last seal was the most complicated due to the large (5.7 cm) diameter of the unit. In the original design of the product, the manufacturers had used a simple rubber o-ring. A high temperature alternative to rubber o-rings is ceramic fiber braid or wick material that could be compressed to form a seal. In this aqueous phase of the work,

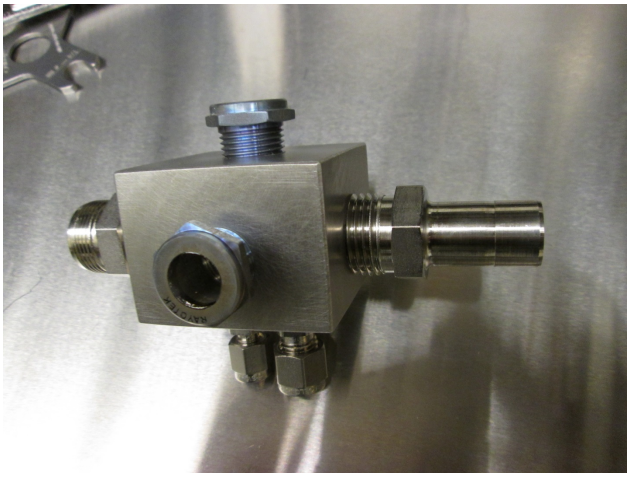

Figure 4.5: Photo of the sampling chamber complete with inlet and outlet ports, sight windows, and temperature and pressure system ports.

the simple rubber o-ring was being used (a solution to this issue for the molten salt case will be addressed later).

4.1.5 Sampling Chamber and Sight Glass

Once the aerosol has been generated in the Collison nebulizer, it is transported in the carrier gas through a 75 mm long by 12.5 mm diameter stainless steel tube into the sampling chamber. The sampling chamber design consisted of a solid stainless steel cube with seven different ports that had been drilled into it leaving a central cavity for the plasma formation. The sampling chamber along with connection ports is shown Figure 4.5. Two 1/2 NPT ports were used to deliver and remove the aerosol stream from the chamber. The inside diameter of the sampling chamber throughput was 22 mm. Three other ports were used to fit 3/8 NPT sight glass windows from Rayotek. Through these windows, the laser light could be focused into the system to create the plasma and the resulting light could be collected. The remaining two ports were designed for the insertion of a thermocouple and for collecting pressure measurements within the chamber during the operation. This sampling chamber was designed such that the plasma formation would be within the aerosol stream itself.

Selection of materials for the optical ports was limited due to the high temperature and

corrosive environment. Quartz and sapphire windows were evaluated for the molten salt application due to their optical properties and high temperature capabilities. In general, quartz had a tendency to etch in the molten salt environment over time, while sapphire would not etch due to excellent chemical resistance. The cost of sapphire window was significantly greater than that of quartz window; therefore, the quartz windows were selected for initial testing for high temperature conditions and plain glass windows were used for the aqueous testing.

4.1.6 Aerosol Removal from the Gas Stream

Once the aerosol stream departed from the sampling chamber, the liquid droplets should be removed before cooling the gas stream to prevent salt freezing in the cooling lines. Several methods were explored to remove the aerosol droplets including mixing/freezing, filtering, and condensing. However, at length, a coalescing filter was selected from United Filtration Systems, Inc. This coalescing filter is shown in Figure 4.6. The filter housing was connected to the sampling chamber using 1/2 NPT and 5/8 inch Swagelok tubing. The housing was approximately 75 mm from the sampling chamber. The filter itself was designed with three layers of stainless steel mesh that would collect and coalesce liquid droplets down to the 1 μm size. The unit was equipped with high temperature seals allowing for a use up to 540°C operation. The collected liquid drained to a 1/4 NPT port at the bottom of the unit. A Swagelok sample bottle was used to collect the liquid for further validation via ICP-MS. The pressure drop across the coalescing filter was unknown and measurement was done later.

4.1.7 Gas Cooling and Cleaning

Following the coalescing filter, the gas stream at 500°C was cooled to room temperature prior passing through a HEPA filter and being released into the exhaust system. The heat removal system should be capable of removing at least 1,057 W of energy. The easiest method would be to use a heat exchanger with water as the cooling fluid. Most heat exchanger designs for

Figure 4.6: Photo of the coalescing filter housing and filter element.

this scale are not designed to operate at temperatures up to 500°C, nor are they designed to operate with such a large temperature gradient. However, one style of heat exchanger, called a tube in tube heat exchanger, fit the application nicely. The tube in tube heat exchanger had two concentric tubes coiled around such that their walls would not touch. The advantage of this system was that it could be easily sealed at high temperature. In addition, since the tubes were not touching, significantly more thermal stress (larger temperature gradient) can be properly handled. A tube in tube heat exchanger was identified and purchased from Exergy miniature heat exchangers. The heat exchanger is shown in Figure 4.7. The gas line connecting the filter housing to the heat exchanger was 6.3 mm stainless steel tubing that was approximately 1 m long.

The heat exchanger performance was calculated (for the assumed maximum conditions, 20 L/min), and results were provided by Exergy. The pressure drop on the argon side of the heat exchanger is 12.2 psi and on the water side 0.62 psi. The water input temperature was 23°C and the exit temperature was 35°C at a flow rate of 1.24 L/min. Due to the high argon gas temperature, some boiling in the heat exchanger may occur; however, boiling should not present a problem in our design because of high flow rates.

To pump and cool the water used in the gas cooling system, an Isotemp II water circulator/chiller was used. The Isotemp II has a cooling capacity of 1,000W at 20°C, which is lower

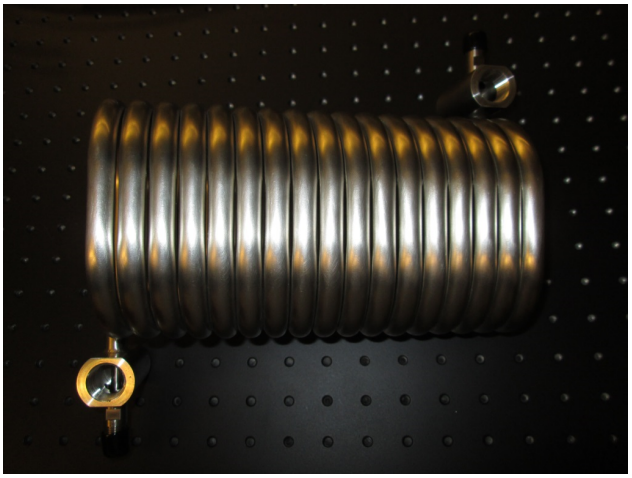

Figure 4.7: Photo of the tube in tube heat exchanger.

than the required amount. However, at 35°C the heat removal is increased to approximately 1,400 W. As a result, the chiller was set to circulate water at a higher temperature to ensure energy removal. Once the gas stream was cooled, it was passed through a HEPA filter before entering the lab exhaust system.

4.1.8 Assembly and Laser Mounting

The entire system was installed on the inside of an inert atmosphere glovebox. However, the glovebox was not sealed in order to better test the system using aqueous fluids and to allow for an easy access during the initial shakedown period. Figures 4.8 and 4.9 show all of the different components as they are assembled into the whole aerosol-LIBS system.

As a result of working in the glovebox, a method to mount the Q-smart 450 Nd:YAG laser to the glovebox was developed as shown in Figure 4.10. Here, a 12 mm x 600 mm x 900 mm optical breadboard was mounted to the side of the glovebox using eight right angle pieces. The laser was then mounted vertically and mirrors were used to reflect the laser beam through a quartz window installed in the glovebox. As a result of this setup, the laser light was easily transported into the glovebox. Blackout materials were installed around the glovebox in order to adhere to laser safety standards.

Figure 4.8: Photo of the aerosol system assembly.

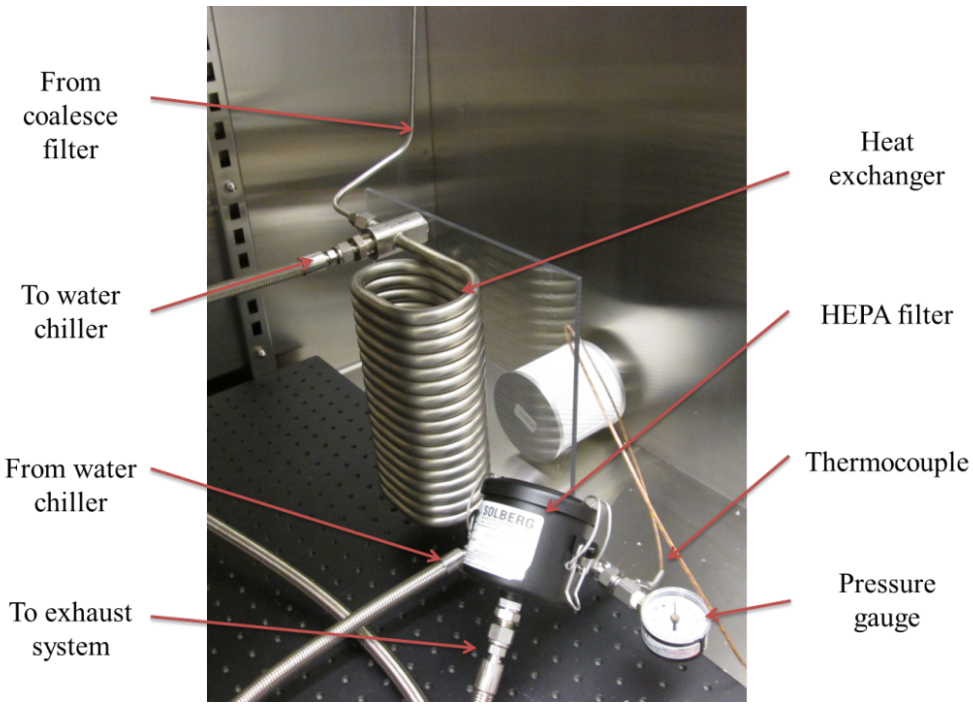

Figure 4.9: Photo of the installed heat exchanger system.

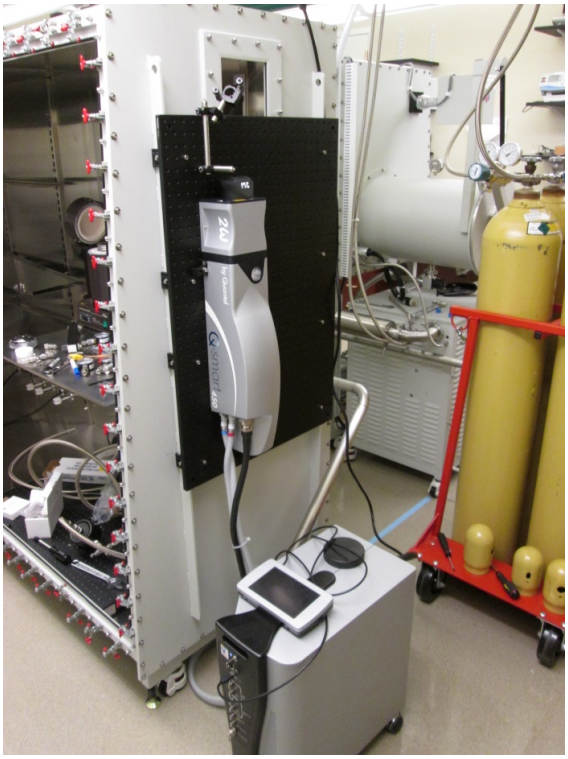

Figure 4.10: Photo of the Q-smart laser mounted to the glovebox and optics used to direct the beam through the window and into the glovebox.

4.2 Initial Testing using Aqueous Media

4.2.1 Materials and Methods

Before operating at the high temperature, a room temperature testing was done in order to gain experience with the aerosol-LIBS system prior to working with molten salts. Here, DI water was used as the working fluid with additives of rare-earth elements (Ce, Nd, and Gd). All the salts were purchased from Alfa Aesar. Concentrations of Ce and Gd ranged from 100 ppm to 10,000 ppm and the Nd concentration was set at 1,000 ppm for all samples. Table 4.1 shows the concentrations of the samples that were made. Here, each element was tested with low (100 ppm), medium (6,000 ppm for Gd and 3,000 ppm for Ce), and high (10,000 ppm) concentrations of another element and vice versa in order to see matrix effects, if any, occurred. Samples were prepared and run using the aerosol-LIBS system and then

Table 4.1: Prepared samples showing the concentrations for Ce and Gd. The Nd concentration was set at 1,000 ppm for each sample.

Standard	ppm Gd	ppm Ce	Standard	ppm Gd	ppm Ce
1	100	100	19	100	100
2	100	500	20	500	100
3	100	1,000	21	1,000	100
4	100	3,000	22	3,000	100
5	100	6,000	23	6,000	100
6	100	10,000	24	10,000	100
7	6,000	100	25	100	3,000
8	6,000	500	26	500	3,000
9	6,000	1,000	27	1,000	3,000
10	6,000	3,000	28	3,000	3,000
11	6,000	6,000	29	6,000	3,000
12	6,000	10,000	30	10,000	3,000
13	10,000	100	31	100	10,000
14	10,000	500	32	500	10,000
15	10,000	1,000	33	1,000	10,000
16	10,000	3,000	34	3,000	10,000
17	10,000	6,000	35	6,000	10,000
18	10,000	10,000	36	10,000	10,000

verified using ICP-MS.

The salt solutions were loaded into a 3-jet Collison nebulizer and argon gas was used as the carrier gas. The aerosol stream passed through a 12.5 mm diameter by 75 mm tube to a sampling chamber as shown in Figures 4.5 and 4.11. The laser light was focused into the sampling chamber using a plano-convex lens with a 50 mm focal length to create the plasma. Light from the plasma was collected using a 25 mm diameter plano-convex lens with a 75 mm focal length. Light was directed at 90° using a dielectric elliptical mirror and then through a 25 mm diameter plano-convex lens with a 100 mm focal length. The latter lens focused the plasma light into the 2 m fiber optic cable to the spectrometer and detector.

The argon gas flow rate was measured using a Key Instruments 1G08 R3 flow meter. The aerosol droplets generated in the Collison nebulizer were characterized using a scanning mobility particle sizer (SMPS) system. The SMPS system used a TSI 3080 electrostatic classifier, a TSI condenser particle counter, and model 3081 DMA. The aqueous droplets

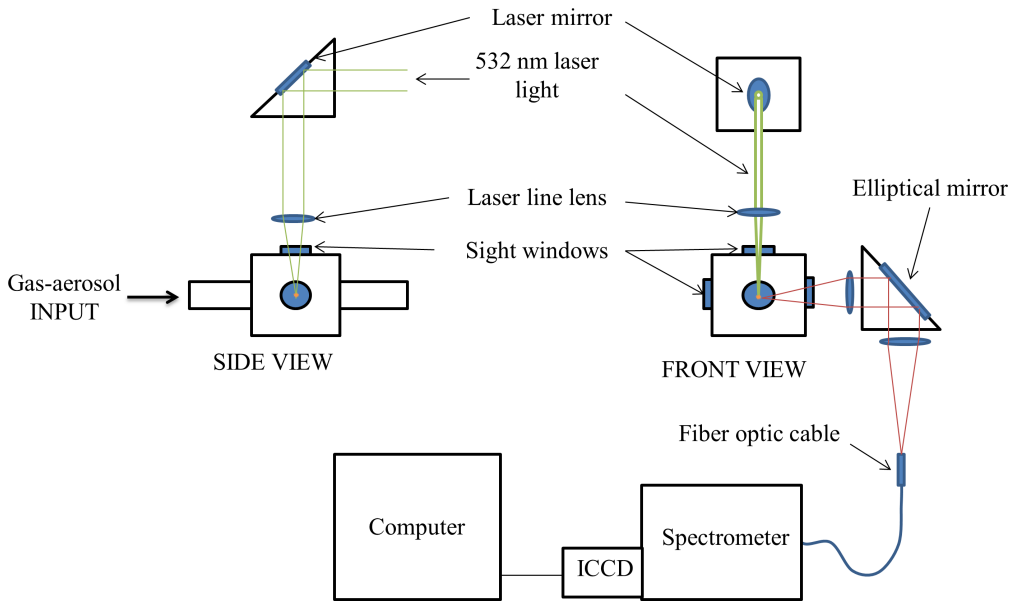

Figure 4.11: Representation of the aerosol system experimental setup and optics.

dried very quickly in the ultra-pure argon and the SMPS system was not able to directly measure the wet diameter. As a result, two 1 m long drying columns with silicone beads were used in series to first dry the aerosol before the measurement was made. From the dry diameter, the wet diameter could be calculated from knowledge of the material volume fractions (concentrations). Here, the amount of salts per droplet were assumed based on the bulk concentration of the sample. Using the component densities and concentration, the volume fraction (VF) of the solids in bulk solution could be calculated. Using relationships between the dry volume, VF, and the droplet wet volume, the wet droplet diameter the following equation was derived:

$$D_w = \frac{D_d}{\sqrt[3]{VF}} \tag{4.2}$$

where D_w is the wet diameter and D_d is the dry diameter of the aerosol particle.

For each sample run, ten repetitions were collected, each consisting of 200 laser shots. In this case, the Andor Solis software was operated in kinetic mode so a spectrum for each laser shot was recorded. The 200 laser shots were then averaged to provide a single spectrum representing that particular repetition. The ten average spectra generated from each sample

were then used to create a single point on the calibration curve. Calibration curves were generated for the low, medium, and high cases and a comparison was made between different emission lines for each case.

4.2.2 Results and Discussion

To better understand the operating conditions of the aerosol-LIBS system, initial optimizations were done. First, the nebulizer flow rate was explored to find the optimal flow rate from a LIBS signal perspective. It was observed that the spectral intensity increased as the gas flow rate decreased. This may be a result of a decreasing number of droplets within the stream which interfere with the incoming laser light. It was determined that the ideal carrier gas pressure was 10 psig prior to the nebulizer; this corresponded to a flow rate of approximately 1.9 L/min. At this flow rate and pressure, approximately 5 ml of solution was used per hour. This pressure and flow rate are within the lower range expected in the design of the aerosol-LIBS system.

Next, the optimal gate delay and gate width were optimized by running a series of experiments while varying these parameters. As the gate delay increased, the signal decreased but the background or continuum noise decreased at a faster rate. As a result, an optimal gate delay was found to be 6 μs with a gate width of 20 μs. The laser power was also varied to determine the optimal energy. At different laser energies, the plasma changed position and shape within the aerosol-gas stream. With higher energies, the plasma became more elongated which created challenges in capturing the light. As a result, a laser energy of 55 mJ was selected to provide good plasma shape and signal. The ICCD camera gain and exposure time were set at 3000, and 0.003 sec, respectively.

Determining the size distribution of the aerosol has proved to be challenging due to the rapid rate at which the aqueous aerosol dried in the pure argon gas. Because drying between the aerosol generation and the SMPS system could not be avoided, drying columns were used to completely dry the aerosol prior to the measurement. From knowledge of the aerosol

composition and density, a liquid volume and size could be estimated from the dry volume diameter. For sample 18 (10,000 ppm Gd and 10,000 ppm Ce), the VF was calculated to be 0.00395. Figure 4.12 shows the wet particle size distribution obtained at 10 psi and 22 °C for sample 18 (10,000 ppm Gd and 10,000 ppm Ce). The observed distribution is bimodal with a total aerosol number density (N) of approximately 5.8×10^6 particles/cm^3 of gas. The intersection between the two log-normal distributions was used as a separation point, and each size distribution was analyzed separately. The geometric mean diameter (d_g) of the distributions were computed using[89]:

$$d_g = CMD = exp\left(\frac{\Sigma n_i ln\, d_i}{N}\right) \tag{4.3}$$

where n_i and d_i are the number of particles and the mid point diameters per size range, respectively. Based on the log-normal distribution, the geometric mean diameter is equivalent to the count median diameter (CMD). The geometric standard deviation (GSD) of the distributions was calculated using[89]:

$$ln\,\sigma_g = \left(\frac{\Sigma n_i (ln\, d_i - ln\, d_g)^2}{N-1}\right)^{1/2} \tag{4.4}$$

The first distribution had a CMD of 1.4 μm and a GSD of 1.2 and the second distribution had a CMD of 4.2 μm and a GSD of 1.0. The bimodal distribution observed may be a result of agglomeration of aerosol droplets within the drying column and tubing prior to the SMPS measurement.

A representative spectrum collected for the aerosol stream configuration is shown in Figure 4.13. In the lower wavelength range, there are numerous peaks from Ce, Gd, Nd, and Ar in the sample. In the upper wavelength range, all of the lines are from Ar with the exception of the H and O peaks shown. The Ce and Gd lines that had a SBR greater than 2.5 with low interference from other peaks were selected for analysis. This proved to be somewhat of a challenge because the rare earth elements Ce, Gd, and Nd have such a high

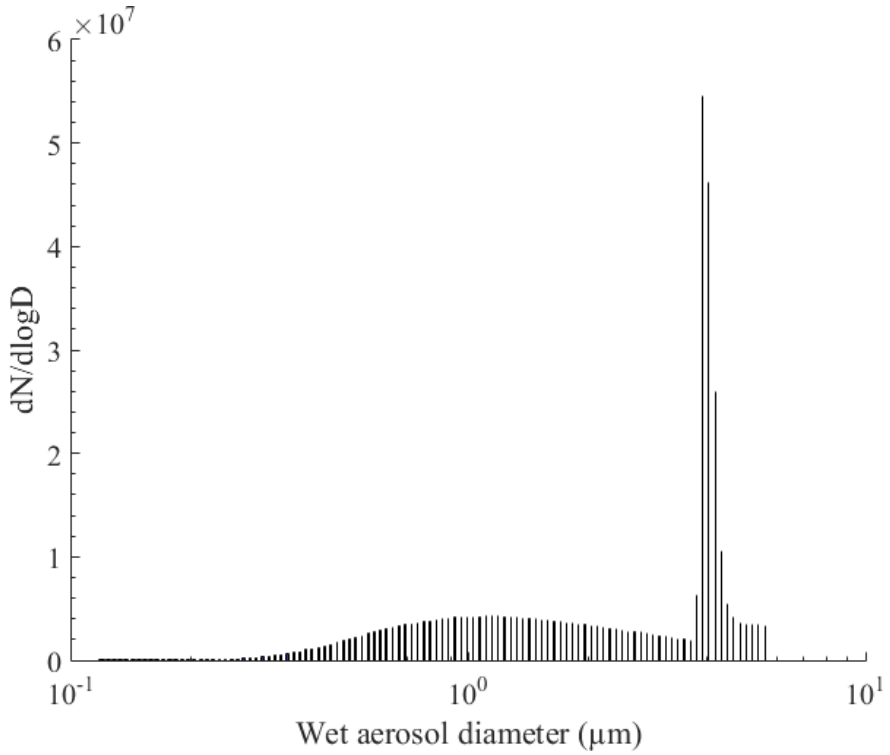

Figure 4.12: A typical size distribution plot for the aerosol generated in this work. The specific plot was generated from sample 18 (10,000 ppm Gd, 10,000 ppm Ce).

density of lines in the lower range. In addition, due to the nature of the aerosol, strong Ar lines were also observed that added to interference. However, several lines were found[69] that met the criteria; they are the Ce 418.660 nm, Ce 428.999 nm, Ce 457.228 nm lines for Ce and the Gd 374.347 nm, Gd 404.986 nm, and the Gd 409.861 nm lines for Gd. Of the lines selected, the Ce 418.660 nm line would have a slight interference with a Gd 418.425 nm line but was included anyway due to its intensity. The Nd in the sample was not analyzed at this time because the concentration was constant throughout all the standards and peak intensities were too weak to be used as an internal standard.

An example of the variation between the different repetitions is shown in Figure 4.14 for sample 4 (100 ppm Gd and 3,000 ppm Ce). In this example, the point-wise %RSD over the spectral range between 355 nm and 460 nm is approximately 5.5% as shown in Figure 4.15. In general, the %RSD's from the 36 samples ranged between 6% and 9% with an average around 7.5%. The best %RSD was 4.4% from sample 11 and the worst was 22% from sample

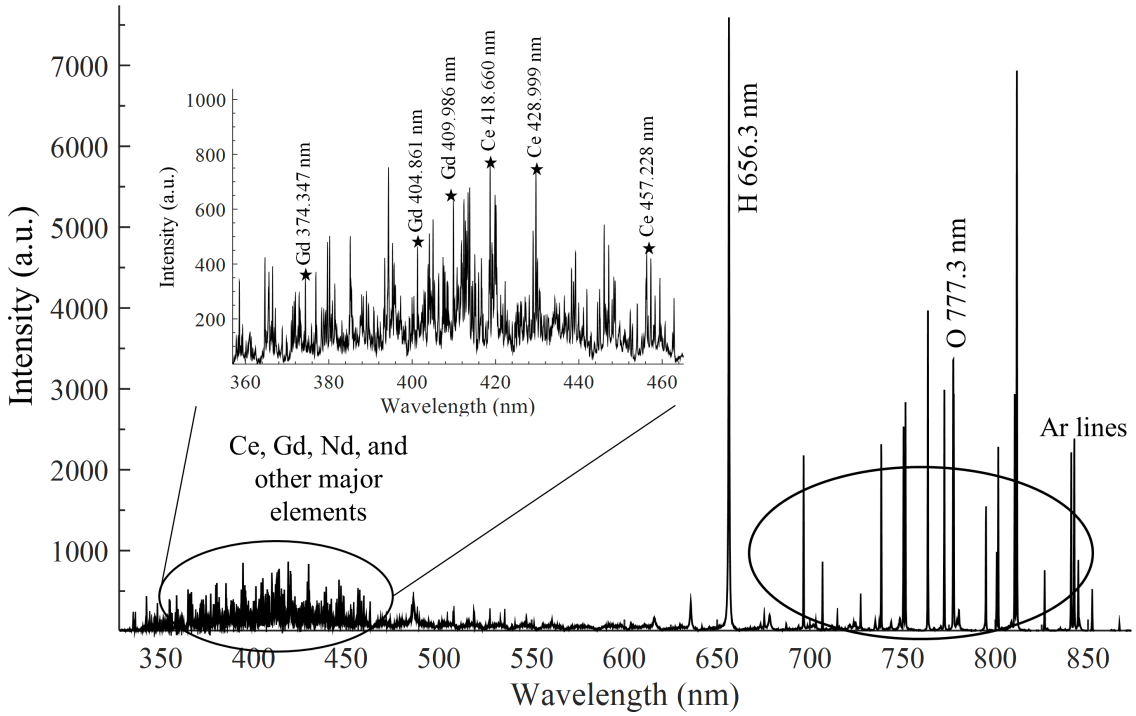

Figure 4.13: A typical spectrum showing the major element peaks and a close up of the spectral region with the minor element peaks. The spectrum was generated from for sample 18 (10,000 ppm Gd, 10,000 ppm Ce).

15. The %RSD values for the repetitions over a large spectral range could provide an overall view of the precision, but to better understand the system, specific peaks were analyzed and results showed better repeatability. The %RSD for the Ce 418.660 nm line intensity averaged 4.4% between all 36 samples with a standard deviation of 1.2%. For the Gd 409.861 nm line, the %RSD averaged 3.8% with a standard deviation of 1.0%.

There were several potential factors that contributed to the variation in the spectra: (1) fluctuations in laser energy, (2) interaction (light scattering, premature plasma formation, and light absorption) of the droplets with the laser light, and (3) condensation at the bottom of the sampling chamber which can splash upwards onto the windows. The energy of the Nd:YAG laser used would vary up to 5% and in some cases was measured at 10% fluctuation. The best way to mitigate or reduce the error here was by using a sufficient number of shots per repetition. During experiments, droplet interference was observed in the form of bright spots within the laser path. As a result of changes in the laser energy, particle interaction,

and presumably the size and location of particles within the plasma, the location of the observed plasma and intensity varied shot-to-shot. The effect of splashing or condensation on the windows was very noticeable when such instances occurred. In the duration of the 36 samples run, two such instances occurred in which the signal was drastically lower. In these cases, the system was dried and the experiments were re-run. An additional source of variation that existed between samples was the position of the sampling chamber with respect to the incoming laser light; this would be a result of small shifts in the system over time as a result of using only a single mounting point for the entire assembly.

The original intent was to use the Nd in the sample as an internal standard; however, the 1,000 ppm amount resulted in a spectral intensity too weak to be of use in that capacity. Since Nd was too low, the other elements contained in the spectra were Ar, H, and O. The Ar gas was not actually a part of the sample itself, but the carrier gas. As a result, if there were any variation with the gas flow, aerosol generation, or number of particles being hit in the plasma, normalization with Ar would not help. Between the H and O, the O line has multiple Ar lines in close proximity. Here, it was noticed that the H 656.3 nm line was isolated and represented the strongest line in the spectra. As a result, this line was the best normalization candidate available. The spectral region between 655 nm and 657 nm (width of the H line) was averaged and then the entire spectra was divided by this value. Each individual spectra was normalized using this method.

The effects of the low, mid, and high concentrations of Ce and Gd in the spectra are shown in Figure 4.16. In Figure 4.16(a), it can be seen that the Gd 418.425 nm line interferes with the Ce line and the measurable area under the curve, and without a deconvolution method, is significantly reduced as the Gd concentration increases. The Ce 428.999 nm and Ce 457.228 nm lines do not show a specific Gd interference line; however, the high density of Gd lines in the spectra contributes to the background in these regions. As a result, the intensities of the lines change slightly as an effect of the Gd concentration. This same background contribution is observed for the Gd lines with respect to the Ce concentration. In addition,

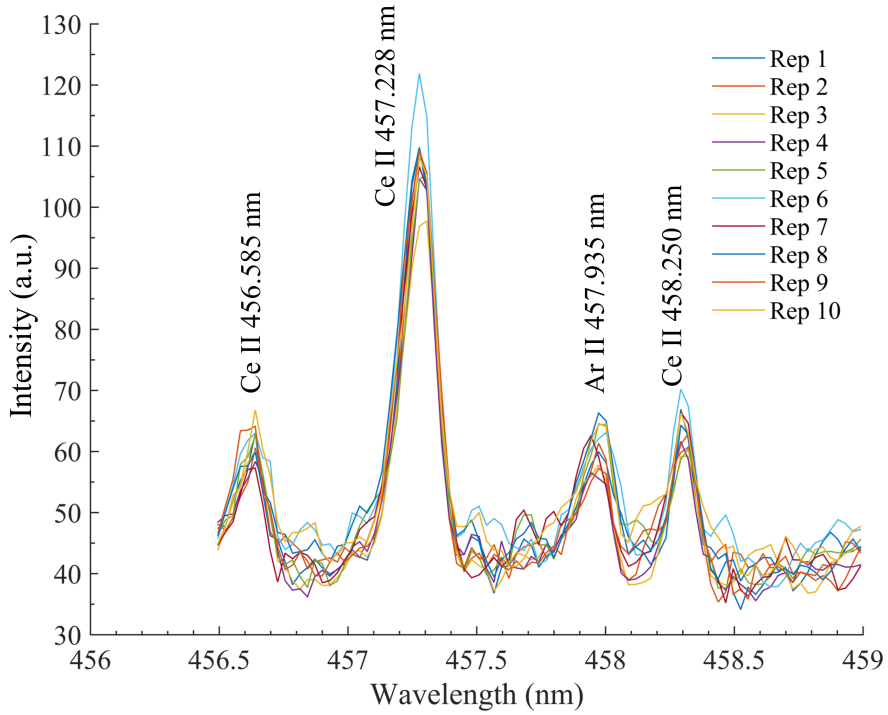

Figure 4.14: Difference between the 10 repetitions taken for sample 4 (100 ppm Gd and 3000 ppm Ce.)

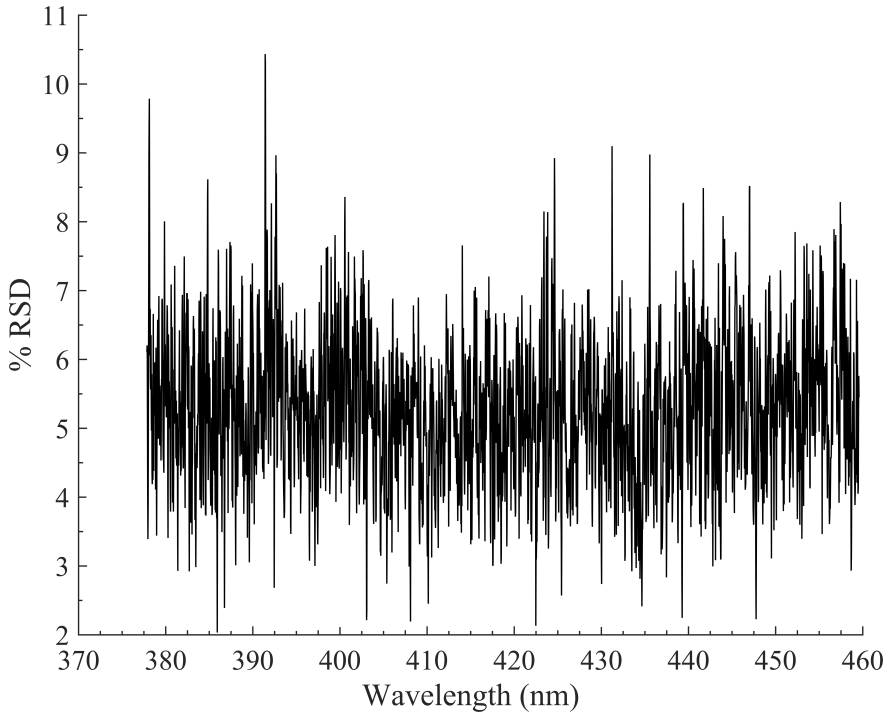

Figure 4.15: Typical plot of the %RSD's between the 10 repetitions taken for each sample. The specific %RSD shown is from sample 4.

the Gd 409.861 nm line has a Ce line interference that affects the peak area. These results show that there is a concentration effect on all of the selected peaks simply as a result of the background contribution.

Univariate Calibration Curves

The program written in MATLAB was used to determine the peak area and intensities for each of the 6 peaks (3 for Ce and 3 for Gd) of interest for each repetition for all 36 samples (2,160 peak selections). The spectral response (peak areas and intensities) between the different repetitions was averaged to get a single point for the calibration curve. The error bars for the data point were the standard deviations between the 10 repetitions.

Figure 4.17 shows calibrations curves for Ce lines generated using the peak areas and peak intensities. Table 4.2 shows the regression coefficients, R^2 values and LOD for the various lines. As expected, the Ce 418.660 nm line shows significant variation with respect to the peak area as a result of the Gd 418.425 nm line. The Ce 418.660 nm calibration curves generated using the peak intensity do not show a strong dependency on the Gd concentration. However, there is a weak function as a result of the Gd background contribution. For example, by examining closely the y-intercept (b_0), it is clear that as the Gd concentration increases, b_0 also increases. Despite this rising value, the regression confidence intervals between the three cases appear to be similar. The peak areas of Ce 428.999 nm and Ce 457.228 nm show less dependence on the Gd concentration than that of Ce 418.660 nm (although slight variations in the slope can be seen). The curves generated using the peak intensities are more affected by the Gd background contribution. Overall, the Ce 418.660 nm curve generated with the peak intensities appeared to have the least variation between the low, mid, and high cases. In addition, it has one of the lowest LOD and is therefore recommended for use. Variation between the low, mid, and high Gd cases for the recommended 418.660 nm peak were compared using a two tailed T-test with 95% confidence. When all cases were compared point-wise, the majority of the points were statistically different. However,

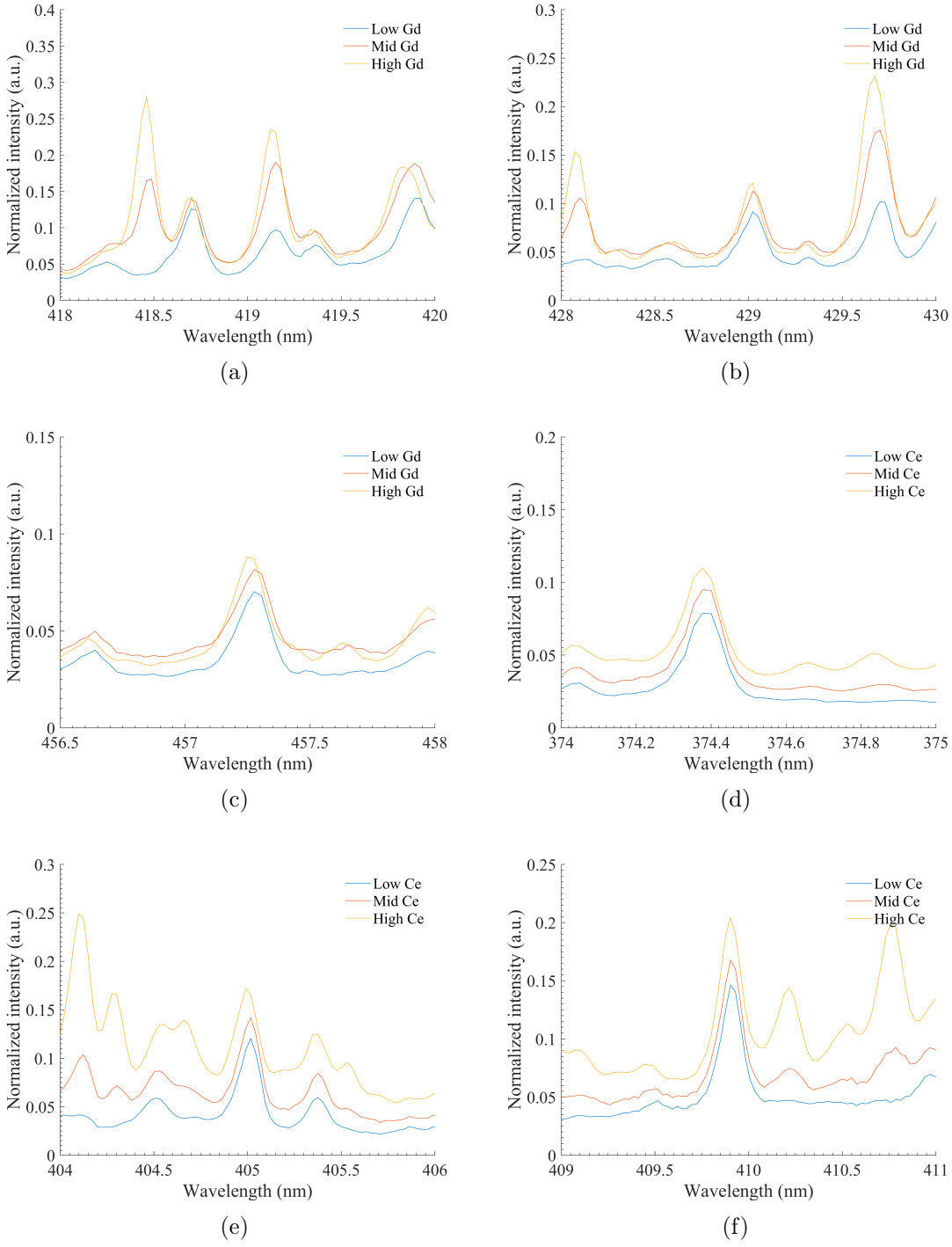

Figure 4.16: The variation of the Ce and Gd spectral lines as a function of the low, mid, and high cases explored. (a) The Ce 418.660 nm line at 3,000 ppm Ce, (b) the Ce 428.999 nm line at 3,000 ppm Ce, (c) the Ce 457.228 nm line at 3,000 ppm Ce, (d) the Gd 374.347 nm line at 3,000 ppm Gd, (e) the Gd 404.986 nm line at 3,000 ppm Gd, (f) the Gd 409.861 nm line at 3,000 ppm Gd.

Table 4.2: Tabulation of the R^2, b_1, b_0, and LOD for the Ce calibration curves.

418.660 nm (Area)	b_1	b_0	R^2	$S_{y/x}$	LOD
Low Gd	4.582e-06	-9.33e-04	0.990	0.0022	129
Mid Gd	3.172e-06	-0.0018	0.980	0.0022	115
High Gd	2.714e-06	-9.00e-04	0.998	5.37e-04	179
418.660 nm (Intensity)	b_1	b_0	R^2	$S_{y/x}$	LOD
Low Gd	3.120e-05	0.0277	0.992	0.0134	163
Mid Gd	3.182e-05	0.0316	0.991	0.0148	168
High Gd	3.045e-05	0.0412	0.998	0.0069	183
428.999 nm (Area)	b_1	b_0	R^2	$S_{y/x}$	LOD
Low Gd	2.600e-06	-6.526e-06	0.995	8.62e-04	369
Mid Gd	2.585e-06	4.945e-05	0.987	0.0015	196
High Gd	2.497e-06	0.0011	0.998	5.54e-04	370
428.999 nm (Intensity)	b_1	b_0	R^2	$S_{y/x}$	LOD
Low Gd	2.000e-05	0.030	0.994	0.0077	164
Mid Gd	2.026e-05	0.041	0.989	0.0102	211
High Gd	1.948e-05	0.053	0.997	0.0050	441
457.228 nm (Area)	b_1	b_0	R^2	$S_{y/x}$	LOD
low Gd	2.183e-06	-4.304e-05	0.987	0.0012	283
Mid Gd	2.157e-06	-2.395e-04	0.989	0.0011	332
High Gd	1.957e-06	8.543e-04	0.995	6.73e-04	325
457.228 nm (Intensity)	b_1	b_0	R^2	$S_{y/x}$	LOD
low Gd	1.566e-05	0.0252	0.988	0.0084	284
Mid Gd	1.544e-05	0.0292	0.993	0.0067	223
High Gd	1.446e-05	0.0366	0.996	0.0044	245

a combined calibration curve was generated using data from the low, mid, and high cases as shown in Figure 4.19(a). Though the T-test showed deviation between the different cases, the combination of the curves provides a good approximation for the Ce spectral response with respect to the concentration. The R^2 value, $S_{y/x}$, and LOD for this curve are 0.994, 0.0117 ppm, and 189 ppm, respectively.

Figure 4.18 shows the Gd calibration curves using both the area and intensity approaches. Table 4.3 shows the regression coefficients, R^2 values and LOD for the various peaks. The Gd curves are similar to the Ce curves in that the Ce background contributes to a change in the y-intercepts for those generated using intensities and slope dependence for the curves generated using areas. Overall the Gd 409.861 nm curve generated using area has the least variation and relatively good LOD. Again a two tailed T-test at 95% confidence was used

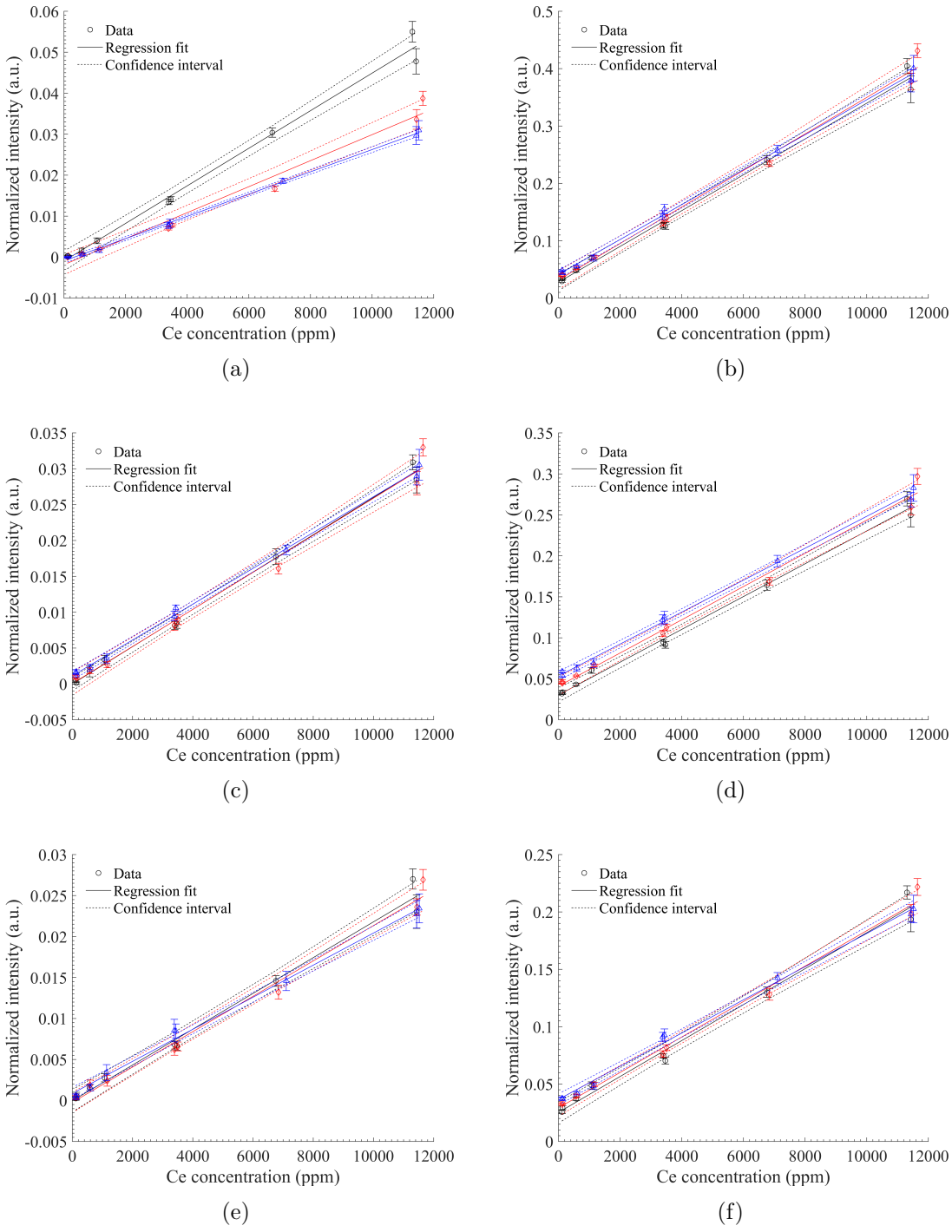

Figure 4.17: Comparison between Ce calibration curves using peak area and max intensities. The black, red, and blue data set sets represent the low, mid, and high cases, respectively. (a) The 418.660 nm using area (b) 418.660 nm line using intensity (c) 428.999 nm line using area (d) Ce 428.999 nm line using intensity (e) Ce 457.228 nm line using area (f) Ce 457.228 nm line using intensity.

Table 4.3: Tabulation of the R^2, b_1, b_0, and LOD for the Gd calibration curves.

374.347 nm (Area)	b_1	b_0	R^2	$S_{y/x}$	LOD
Low Ce	2.768e-06	-7.876e-04	0.992	0.0012	211
Mid Ce	2.483e-06	-4.444e-04	0.994	9.68e-04	307
High Ce	2.373e-06	7.192e-05	0.990	0.0012	241
374.347 nm (Intensity)	b_1	b_0	R^2	$S_{y/x}$	LOD
Low Ce	2.457e-05	0.0104	0.993	0.0100	134
Mid Ce	2.329e-05	0.0175	0.994	0.0086	149
High Ce	2.255e-05	0.0300	0.990	0.0109	181
404.986 nm (Area)	b_1	b_0	R^2	$S_{y/x}$	LOD
Low Ce	4.497e-06	-0.0013	0.994	0.0016	106
Mid Ce	4.105e-06	-0.0011	0.993	0.0017	147
High Ce	3.848e-06	-8.57e-04	0.993	0.0016	340
404.986 nm (Intensity)	b_1	b_0	R^2	$S_{y/x}$	LOD
Low Ce	3.723e-05	0.0129	0.993	0.0152	120
Mid Ce	3.411e-05	0.0284	0.986	0.0102	124
High Ce	3.445e-05	0.0542	0.994	0.0130	244
409.861 nm (Area)	b_1	b_0	R^2	$S_{y/x}$	LOD
Low Ce	4.964e-06	-6.632e-04	0.994	0.0019	297
Mid Ce	4.706e-06	-8.593e-05	0.994	0.0018	358
High Ce	4.516e-06	0.0014	0.993	0.0018	350
409.861 nm (Intensity)	b_1	b_0	R^2	$S_{y/x}$	LOD
Low Ce	3.852e-05	0.0343	0.995	0.0141	161
Mid Ce	3.732e-05	0.0459	0.992	0.0167	164
High Ce	3.439e-05	0.0806	0.993	0.0189	243

to point-wise compare between the low, mid, and high cases. The T-test showed that the different cases were not the same; however, as in the Ce case, a calibration curve using the recommended peak has been generated using all 36 samples as an approximation. This calibration curve is shown in Figure 4.19(b). The R^2, $S_{y/x}$, and LOD are 0.992, 0.0019 ppm, and 316 ppm, respectively.

To validate the calibration curves for Ce and Gd, and to explore the accuracy of the LIBS measurements, two independent samples were run with Ce and Gd concentrations within the studied ranges. Table 4.4 shows the values for independent samples 1 and 2 generated from the combined calibration curves. When comparing the predicted and actual values for that given concentration, the predicted values are nearly within the estimated error of the measurements. Interestingly, the calibration curves overestimate the concentration for

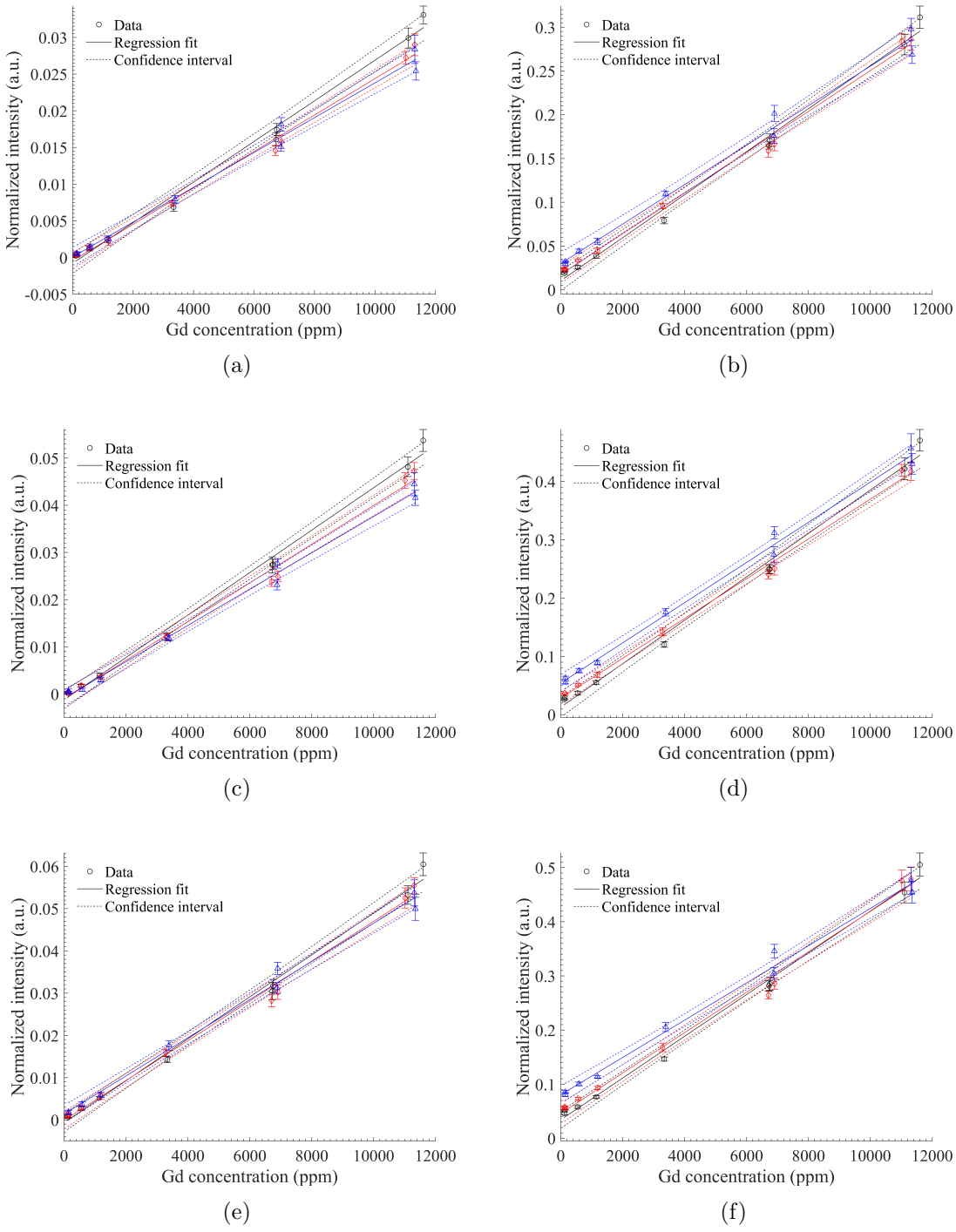

Figure 4.18: Comparison between Gd calibration curves using peak area and intensities. The black, red, and blue data set sets represent the low, mid, and high cases, respectively. (a) The 374.347 nm using area (b) 374.347 nm line using intensity (c) 404.986 nm line using area (d) 404.986 nm line using intensity (e) 409.861 nm line using area (f) 409.861 nm line using intensity.

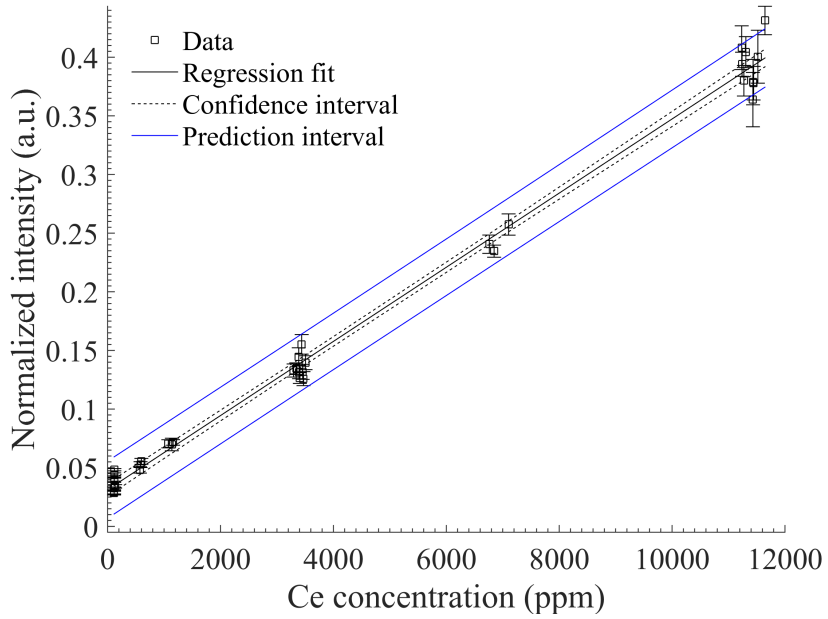

(a)

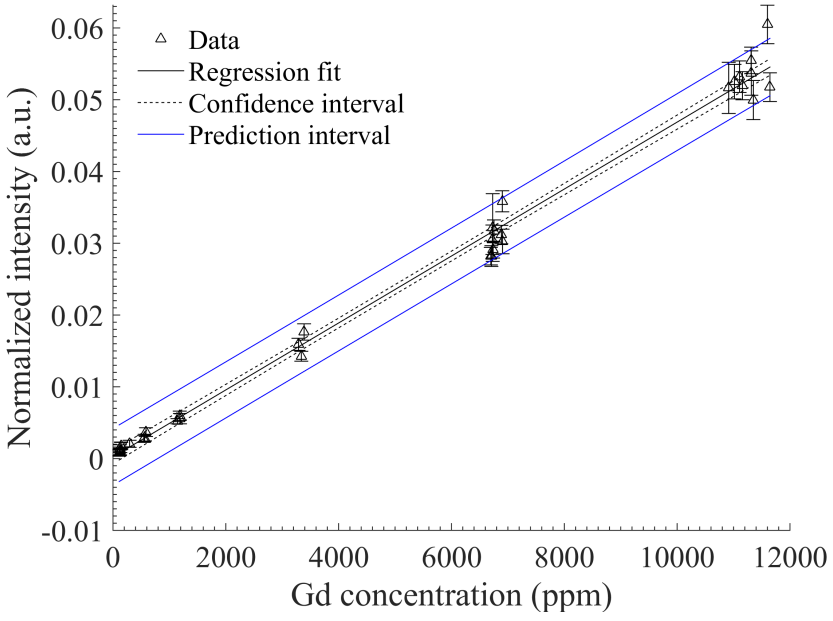

(b)

Figure 4.19: (a) The Ce curve generated using all 36 samples from the Ce 418.660 nm peak using intensity. (b) The Gd curve generated using all 36 samples from the Gd 409.861 nm peak using area.

Table 4.4: Table showing the different values for the independent samples generated using the combined Ce 418.660 nm peak and the Gd 409.861 nm peak by univariate calibration.

Sample 1	Predicted (LIBS)	Actual (ICP-MS)	% Difference
ppm Ce	1401±501	1252±75	11.24
ppm Gd	10302±848	10203±500	0.96
Sample 2	Predicted (LIBS)	Actual (ICP-MS)	% Difference
ppm Ce	4548±488	5244±250	-14.22
ppm Gd	5312±832	6219±260	-15.73

both Ce and Gd (although the Gd concentration is almost exactly predicted). The predicted values for unknown sample 2 appear to be underestimated by approximately 15%. Overall, the validations of the univariate calibration curves generated for the aqueous samples perform well despite small variations as a result of the low, mid, and high concentration effects within the samples. The RMSEP for the calibration curves was estimated from the predicted independent samples. The RMSEP for the Ce and Gd curves was 503 ppm and 645 ppm, respectively.

In addition to the unknown samples, a LOOCV approach was used to further assess the calibration curves and the accuracy. Being that there are 36 total samples with a strong correlation, the regression curve should not change significantly, and indeed it does not. The % error for the left out samples were calculated for the Ce and Gd cases using the combined calibration curves and results are shown in Table 4.5. For Ce, the % error for the 100 ppm concentration sample is 125% which is not acceptable for analytical results. The LOD for the Ce curve is 189 ppm so this result is not unexpected. The % error for the other Ce concentrations ranges are acceptable, especially for concentrations greater than 500 ppm where the % errors range between 3-7%. The % errors for Gd follow a similar trend to the Ce measurements. For samples containing more than 500 ppm, the % error's were less than 10% which would be acceptable for most analytical measurements. Using the LOOCV approach, the accuracy of the system was further assessed to better understand the limitations of the analytical setup. The RMSECV for the Ce and Gd curves was calculated to be 390 ppm and 421 ppm, respectively.

Table 4.5: The average % error between the univariate predicted sample concentration and the actual concentration for LOOCV analysis.

Sample concentration	Ce % Error	Gd % Error
100 ppm	125%	57%
500 ppm	17%	10.4%
1,000 ppm	7%	5.0%
3,000 ppm	5.1%	7.6%
6,000 ppm	3.0%	5.3%
10,000 ppm	5.2%	3.1%

Multivariate Calibration Curves

The commercial package PLS_toolbox by Eigenvector Research was used to generate a PLS model of the generated spectra. The 10 spectra from each sample were divided into two groups (5 repetitions each) and then averaged. This may result in over-fitting. The first and second groups were for calibration and validation, respectively. In the PLS modeling, the entire spectra are used resulting in a model that is more robust and is less prone to matrix effects. In the first part of the modeling, the number of latent variables (LV) was selected to minimize the RMSECV. Here, the RMSECV was determined using venetian blinds within the calibration set. Figure 4.20 shows that as the number of LV's increase, the RMSECV decreases rapidly at first and then levels off. The PLS_toolbox software recommended that 3 LV be used for this system since the first three values would capture the majority of the system response. However, to further decrease the RMSECV, 7 LV were chosen for this model. The RMSECV for this condition is 406 ppm. Figure 4.21 shows the Ce calibration curve generated from 5 repetitions from each of the 36 samples. The calibration curve shows a very strong linear trend.

Next, the spectra that were not used in the calibration set were used to validate the model. Figure 4.22 shows the predicted vs. measured results. The RMSEP for the validation set was calculated to be 519 ppm. The % error between the PLS predicted concentrations and the ICP-MS measured results were calculated to distinguish the accuracy of the model from the validation data set. Table 4.6 shows the % error for the different Ce concentration

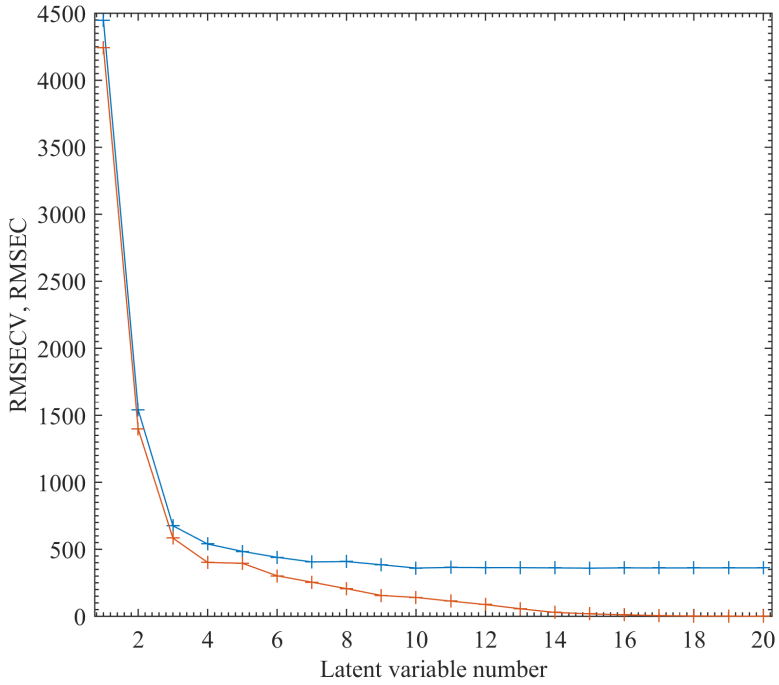

Figure 4.20: The number of latent variables as a function of the root mean squared error of cross validation (RMSECV).

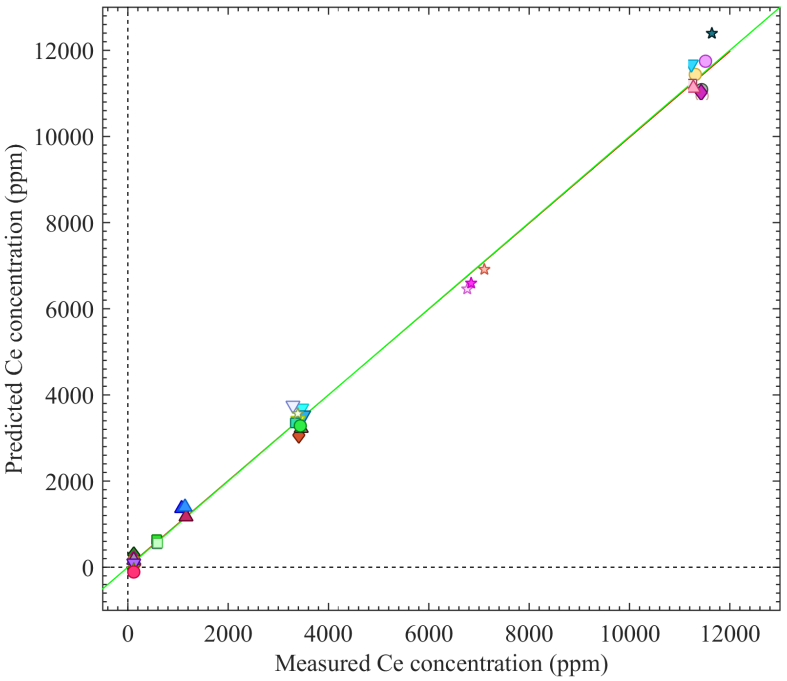

Figure 4.21: Calibration curves for Ce generated from the PLS model.

Table 4.6: The average % error between the predicted sample concentration using the PLS model and the actual concentration.

Sample concentration	Ce % Error	Gd % Error
100 ppm	107%	190%
500 ppm	16.4%	50.2%
1,000 ppm	27.8%	5.65%
3,000 ppm	8.4%	13.9%
6,000 ppm	3.8%	5.0%
10,000 ppm	6.5%	6.6%

ranges. As was observed in the univariate case, results in the lower range have poor % error's; however, the % error's are higher overall. In PLS, the LOD could not be calculated directly; but from the validation, accuracy with this model is poor for sample concentrations below approximately 1,000 ppm.

For Gd, a PLS model was generated using the similar method for the Ce cases. The number of LV was left at 7 as before because the trend was almost identical. However, in this case, the RMSECV was 417 ppm. Figure 4.23 shows the calibration curve for Gd. Figure 4.24 shows the validation results. The RMSEP for the validation set is 536 ppm. Table 4.6 gives a list of the calculated % error's for the Gd validation set. The % error's for the 100 and 500 ppm concentration ranges are too high to be acceptable in an analytical measurement, but the % errors for the higher concentration ranges are within an acceptable level.

The PLS models for Ce and Gd were applied to the unknown samples as was done with the univariate cases. Table 4.7 shows a comparison between the actual concentrations of the unknown samples and the predicted values based on the PLS model. The Ce concentration for unknown sample 1 shows the greatest variation from the actual value with a % difference of 24.3% which is consistent with the validated results. Despite the large variation for unknown sample 1 Ce concentration, the Gd for both samples and Ce for unknown sample 2 were closely predicted. The RMSEP for these cases was 583 ppm and 280 ppm for the Ce and Gd samples, respectively.

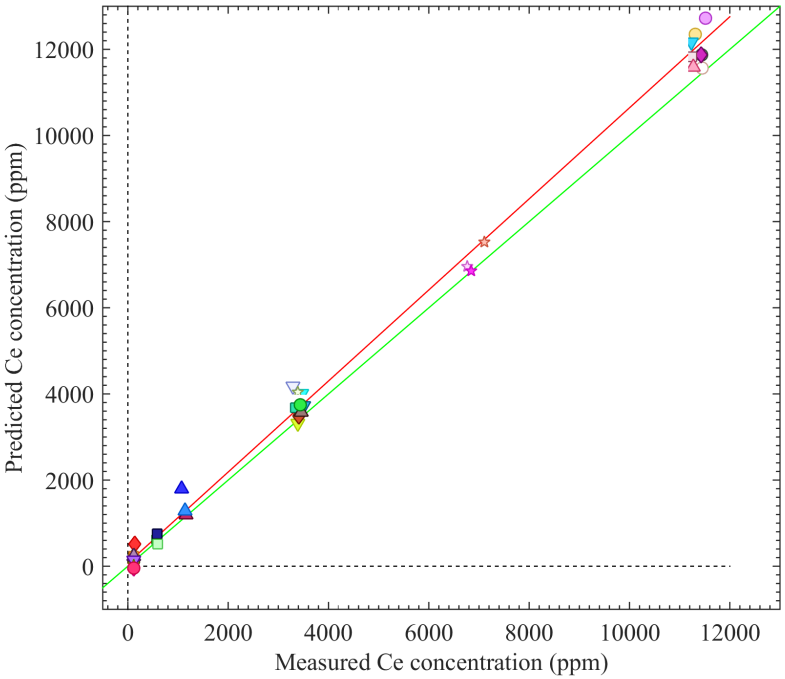

Figure 4.22: The measured vs. predicted results for the Ce validation set.

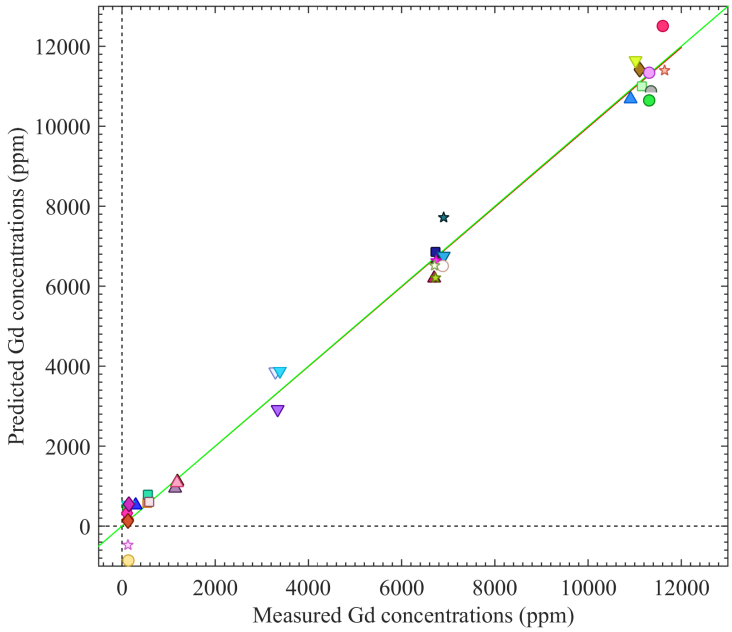

Figure 4.23: Calibration curves generated from the PLS model for Gd.

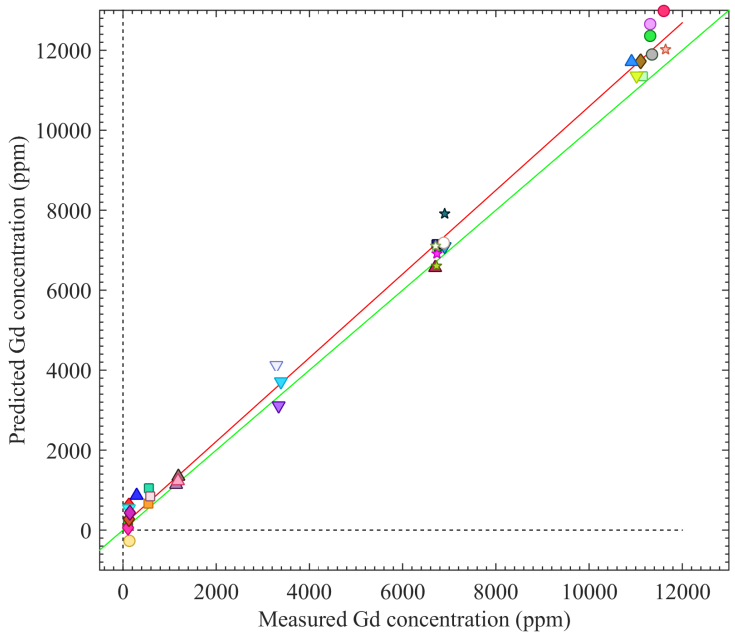

Figure 4.24: Validation generated from the PLS model for Gd.

Table 4.7: Predicted vs actual concentrations for the independent samples. Predictions were done using the PLS models.

Sample 1	Predicted (ppm)	ICP-MS (ppm)	% Difference
ppm Ce	1,599 ± 425	1,252 ± 75	24.3%
ppm Gd	10,547 ± 438	10,203 ± 500	3.3%
Sample 2	Predicted (ppm)	ICP-MS (ppm)	% Difference
ppm Ce	4,992 ± 440	5,244 ± 250	-0.5%
ppm Gd	5,961 ± 450	6,219 ± 260	-4.2%

4.3 Summary and Conclusions

A novel molten salt aerosol system has been designed, built, and tested using an aqueous media. The main design incorporates a Collison nebulizer to generate the aerosol. The Collison nebulizer was an ideal candidate for this application due to its all stainless steel construction and reduced likelihood of material clogging. Other components such as the gas pre-heat, sampling chamber, filtration system, and gas cooling were described and key design features were determined.

In the initial design period, the system was tested at room temperature using an aqueous solution containing Ce, Gd, and Nd with concentrations ranging from 100 ppm to 10,000 ppm. The aerosol generated using the Collison nebulizer was bimodal with a CMD of 1.4 μm and 4.2 μm. The %RSD between the 10 repetitions collected per sample averaged at 7.5% for the spectral range between 355 nm and 460 nm. The %RSD values were 4.4% and 3.9% for the Ce and Gd lines of interest, respectively. Variation in the spectra could be attributed to fluctuations in laser energy, particle interactions, and small shifts in the position of the sampling chamber.

Several Ce and Gd lines from the spectra were analyzed to gain insights on the concentration effects between Ce and Gd. It was determined that for the Ce 418.660 nm peak there were a few interferences as a result of a close Gd line. However, the peak intensity was not greatly affected. In addition, as a result of the high density of lines for Ce and Gd, even areas with no apparent lines were influenced as a result of an apparent background. The univariate calibration curves for the Ce and Gd lines were presented and the Ce 418.660 nm peak using peak intensity was determined to be the ideal peak for Ce analysis. In this case, the R^2 is 0.994 and the LOD is 189 ppm. The ideal Gd line is the 409.861 nm line using peak area, in this case, the R^2 was 0.992 with the LOD of 316 ppm. The accuracy of the univariate calibration curves and the analytical setup was explored using LOOCV and independent samples. The LOOCV analysis showed that the analytical setup and univariate

model were capable of providing acceptable results for concentrations greater than 100 ppm. In addition, the RMSECV for the Ce and Gd univariate calibration curves were calculated to be 390 ppm and 421 ppm, respectively. The LIBS analysis on the independent samples overpredicted the sample 1 by up to 11% and under predicted the sample 2 by 15%. The RMSEP of the calibration curve were calculated to be 503 ppm and 645 ppm, respectively. Table 4.8 shows a summary of the analytical results for Ce and Gd.

Table 4.8: Summary of the aqueous aerosol-LIBS results.

	Ce	Gd
%RSD	4.4%	3.8%
Univariate		
b_1	3.16E-05	4.66E-06
b_0	0.0313	2.38E-04
R^2	0.994	0.992
$S_{y/x}$ (ppm)	0.0117	0.0019
LOD (ppm)	189	316
RMSECV (ppm)	390	421
RMSEP (ppm)	503	645
Multivariate		
LV	7	7
RMSECV (ppm)	406	417
RMSEP (ppm)	519	536

In addition to the univariate analysis, a multivariate approach using PLS was being done to generate calibration models. For these models, the 10 repetitions per sample were split to create calibration and validation data sets. The repetitions in each of the sets were averaged to provide 36 total sample points, each an average of 5 repetitions. The Ce PLS model used 7 LV and had a RMSECV of 406 ppm. The Gd model also used 7 LV and had a RMSECV of 417 ppm. From the validation data set, the % error between the predicted and accepted true concentrations were calculated. Results show that the model poorly predicts the lower concentration range and does not predict the upper concentration range as well as the univariate case. From the validation set, the RMSEP was calculated to to be 519 ppm and 536 ppm for Ce and Gd, respectively. For the unknown samples, the PLS models over predict the sample 1 by up to 24% for the Ce case. The sample 2 was under predicted by

4.2% which was an improvement over the univariate case. Overall, the PLS models yield acceptable analytical results.

This study was completed with the successful testing of the aqueous aerosol-LIBS system. Results show the feasibility of the system and potential areas in the design that can be improved in the next study within this dissertation–such as the sampling chamber design and the system mounting mechanism.

Chapter 5

Molten Salt System Design and $CeCl_3$ Testing

5.1 Molten Salt Experimental Design

5.1.1 Initial Design and Shakedown

Initial System Design

In the aqueous design, the aerosol-gas stream entered directly from the 5/8 inch tubing of the Collison nebulizer into the sampling chamber where the LIBS plasma was formed in its center. As a result of this configuration, multiple particle interactions (scattering) with the laser light occurred, which consequently, varied with respect to the plasma location and strength. To minimize this effect, a new sampling chamber was redesigned in which the optical windows were now centered at the top of the 5/8 inch aerosol input stream. As a result, the plasma formation could be positioned at the top surface of the stream while still having the plasma centered with respect to the light collection windows. The intent with this new design was to reduce the number of particles interacting with the laser prior to breakdown (that is, it helped reduce the variation in the plasma location). The new sampling chamber also used 3/8 NPT sight glass windows; however, rather than plain glass windows, a quartz window with a 6 mm optical port was used. From the aqueous study, the pressure within the sampling chamber did not change, as a result, in the new sampling

Figure 5.1: Deacon 770-L thread sealant used to seal the NPT threads used to attach the tubing to the sampling chamber.

chamber design, only one port was added to measure the temperature.

Prior to molten salt experiments, the seals in the nebulizer, sampling chamber, and coalesce filter needed to be changed to operate at high temperatures. All of the threaded joints were sealed using Deacon 770-L, which is a high temperature (up to 500°C) thread sealant as shown in Figure 5.1. This product has a tar like consistency and was spread on all of the threads prior to assembly of the component. As the product was being cured with temperature, it released CO_2 and CO off-gases. To prevent contamination within the glovebox, the seals were cured at 200°C in the fume hood prior to installation. The coalescence filter was fit with Flexatalic seals (United Filtration Systems, Inc.). The main seal between the nebulizer and the jar was made using a graphite impregnated cord that was cut to size and fitted into the o-ring groove. The system was pressure-tested offering a leak free system up to 40 psi, at which point a small leak developed between the jar and the nebulizer.

In Chapter 4, the heating requirements and components for the gas pre-heat and salt melting furnaces were addressed at the maximum assumed gas flow rate of 20 L/min. From

the aqueous experiments, it was apparent that these flow rates were not achievable or desirable with the Ar carrier gas. Originally, it was assumed that at the high gas flow rate, the temperature drop in the gas stream from the gas pre-heat to the nebulizer would be small. However, initial testing of the system at the operating temperature and typical flow rates showed that the gas temperature, as measured at the top of the nebulizer, was only 130°C. This temperature was obtained via a 1/8 inch diameter stainless steel sheathed thermocouple that had been inserted into the nebulizer feed line. To ensure the gas would not freeze the salt in the nebulizer, a 0.5 inch by 24 inch heating tape was coiled around the gas tubing leading from the gas heater to the melt furnace. This heating tape was controlled at 500°C. In addition, two cartridge heaters were added, one into the sampling chamber and the other to the coalesce filter. Each cartridge heater (125 W) could be operated up to 500°C.

Another major modification was to fit the entire system with a proper insulation. This proved to be rather challenging due to several constraints: (1) it needed to be easily removable, or at least allow for the disassembly of components for cleaning, (2) it needed to be relatively dust free, (3) it needed to have minimal off gases at a high operating temperature, and (4) it needed to be compact. Several different configurations were explored. However, in the final design, two rigid discs of insulation lined with a stainless steel mesh were used to top the melting furnace. The thickness of the insulation around the nebulizer was approximately 25 mm. The stainless steel was placed to provide structural support as well as for dust control. The tubing, sampling chamber, and coalescence filter were first wrapped in a half inch thick ceramic blanket before being covered with an insulation repair wrap that solidified into a hard casing material. This repair wrap supported the insulation structurally and reduced dust formation. The completed setup with all the insulation in place is shown in Figure 5.2.

Just prior to closing off and sealing the glovebox, the 4 m fiber optic cable from Ocean Optics was inserted through a port in the wall of the glovebox and sealed using a cord grip and epoxy. Following this process, the glovebox was sealed to establish the argon atmosphere

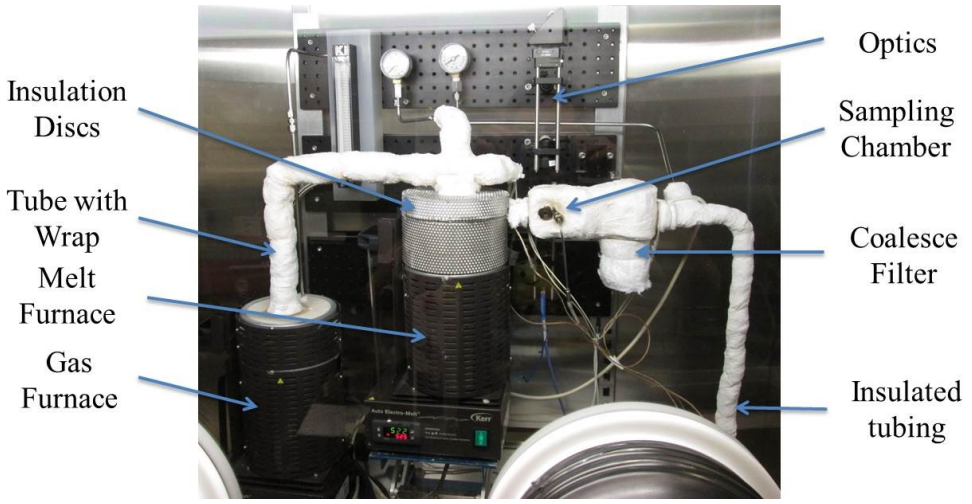

Figure 5.2: Initial high temperature aerosol-LIBS configuration with insulation and heating.

prior to operating the aerosol-LIBS system with molten salt.

Shakedown Testing and Optimization

For the initial testing, 41.5 g of eutectic LiCl-KCl salt with 5 wt% $CeCl_3$ was used. Optimization was done using the SBR for the Ce lines used in the aqueous study. In the optimization study, three repetitions of 250 shots each were taken and averaged to provide a representative spectrum for every explored condition.

During the first experiment, it was observed that the plasma location shifted slightly as observed before with the aqueous case. In addition, small bright spots, presumably light scattering from droplets in the laser path were observed. It is apparent that the aerosol gas stream mixed into the entire sampling chamber volume while particle interaction with the laser was distorting the plasma formation (this was being observed in the aqueous case as well).

In order to better understand the nebulizer operation, the nebulizer gas pressure was explored at a laser energy of 65±5 mJ. Since there was no pressure measurement at the sampling chamber itself, the differential pressure between the nebulizer and sampling chamber was unknown. However, it was observed that as the gas pressure prior to the nebulizer in-

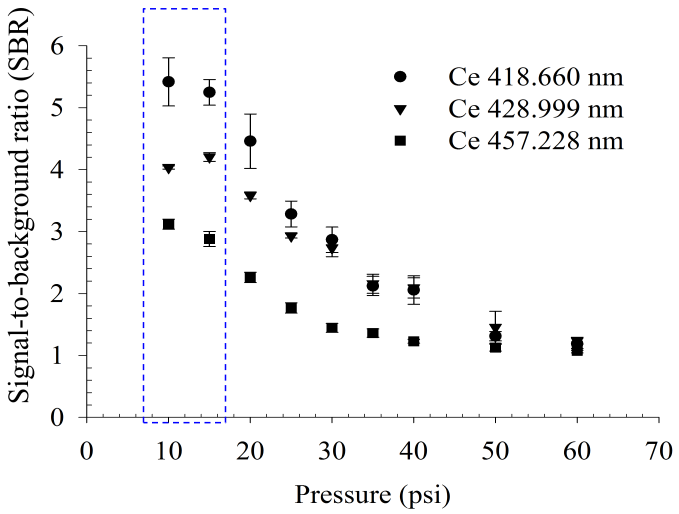

Figure 5.3: The SBR as a function of the argon gas pressure in a 3-jet nebulizer.

creased from 10 psi to 60 psi, the flow rate of the aerosol-gas stream would increase from 0.63 L/min to 1.5 L/min, respectively. These flow rates were significantly lower than anticipated flow rates in the initial design. The SBR as a function of the pressure is shown in Figure 5.3 for a 3-jet nebulizer for the 418.660 nm, 428.999 nm, and 457.228 nm lines. The results indicate that the LIBS signal decreases significantly with increasing pressure. This may be a result of increased particle interference with higher pressures. Below approximately 10 psi, the nebulizer becomes unstable. Thus, a gas operating pressure of 10 to 15 psi has been determined to be an optimal range.

After this first test, a pressure gauge was placed in the temperature port of the sampling chamber and the pressure drop for the above pressures was recorded to be approximately 1.5 psi to 2 psi across the studied pressure range. Figure 5.4 shows the SBR as a function of the laser energy used while operating at a gas pressure of 10 psi showing that the SBR increases linearly up to about 90 mJ where the trend reaches its asymptotic value. Laser energies beyond 140 mJ were not studied, but it was anticipated that the SBR plateau would eventually drop off to lower values. Interestingly, the %RSD between the three repetitions dropped with respect to the laser energy from 10% to 4.5% from the 40 mJ case to the 140

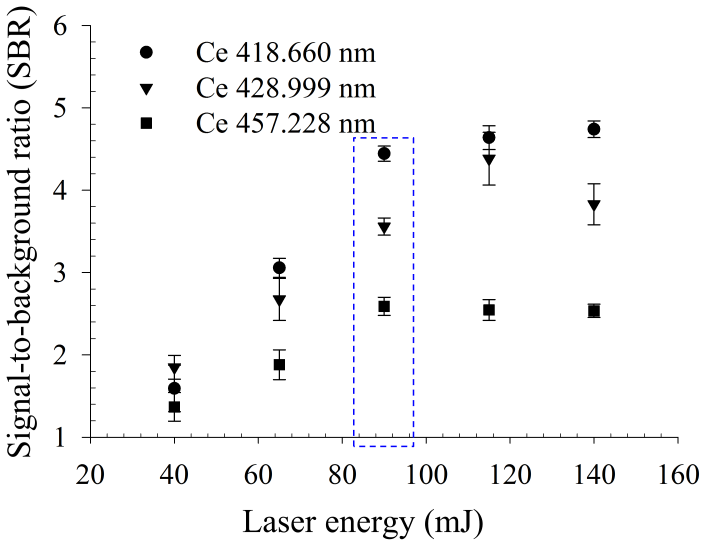

Figure 5.4: Optimization of the laser energy.

mJ case, respectively. This is partially a result of a more stable laser at higher energies. In most cases, the goal is to maximize the SBR when optimizing; however, in order to operate at a safer, less energy intensive range for the laser, a different approach was used. In this case, the intersection between the upward slope and the plateau (90 mJ) was identified as the optimal value since it provided the lowest laser energy while still achieving high SBR's.

Following initial testing, salt droplets were observed between the nebulizer lid and the jar, indicating that the seal had failed. Of the 41.5 g of salt added, only 35 g of material were recovered from the nebulizer jar and system components. There are several potential explanations for the missing material contents; these could be either (1) it leaked through the nebulizer seal and was deposited into the furnace, (2) it deposited in the tubing or heat exchanger prior to the HEPA filter, or (3) salt droplets were small enough that they were trapped in the gas stream and passed through the HEPA filter and into the exhaust system. More likely, all three scenarios could play parts in the missing material contents. It should be noted that there was only a small gap (0.085 inch) between the bottom of the nebulizer tip and the bottom of the jar; this could decrease the flow of the fluid being drawn into the gas jet.

Figure 5.5: Photo showing the inside of the nebulizer lid with the graphite cord placement.

After this initial molten salt test, several modifications to the system were further explored to improve performance. First, a new nebulizer shaft was installed in order to increase the distance between the nebulizer tip and the bottom of the jar. Secondly, a 0.5 μm coalescence filter was used in place of the 1.0 μm filter. The hope in these modifications was to create better flow characteristics in the system and to reduce the amount of missing material per run. To prevent salt leaking around the nebulizer seal, several methods were explored to improve the graphite cord placement. It was determined that placing the square cord flat across the o-ring groove (see Figure 5.5) provided the best results.

In the next shakedown test at 3 wt% $CeCl_3$, the modifications to the aerosol-LIBS system as well as a 1-jet nebulizer tip were explored as a function of the carrier gas pressure. The geometry of the nebulizer tip was exactly the same, but with two fewer jets than the 3-jet case. One effect of fewer jets was that the gas flow rate and salt consumption in the nebulizer jar would be approximately 2/3 less. This allowed for a LIBS measurement while consuming less material. Results for this study are shown in Figure 5.6. Here, the SBR has a maximum between 10 and 15 psi where the signal at 10 psi is significantly lower than that at 14 psi; this is different from the observation made with the 3-jet system. When the 1-jet and 3-jet systems were being compared directly, as shown in Figure 5.7, the 1-jet system has a lower

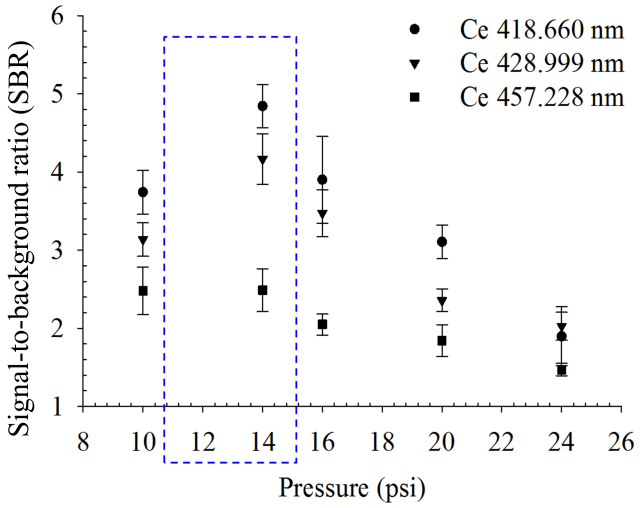

Figure 5.6: SBR as a function of the nebulizer gas pressure for a 1-jet system.

signal in general. The exact reason for this is unknown since several modifications to the system were done prior to this test. However, at approximately 15 psi the variation between the two systems is not large. The %RSD's for the different pressures were 13.3%, 6.6%, 30%, 9.3%, and 9.9%, for the 10, 14, 16, 20, and 24 psi pressures, respectively. As a result of increased signal and a reduction on the %RSD's, approximately 14 psi is the optimal pressure for the 1-jet system.

With the addition of the 0.5 μm filter, the pressure drop across the filter increased over what was observed for the 1.0 μm case. For the highest pressure recorded (24 psi), the pressure at the gauge was 30 psi with a 6 psi pressure drop across the filter. The 6 psi pressure in the jar and sampling chamber region increased salt leaking through the nebulizer main seal. However, all but 1 g of the added material was recovered following the experiment.

Near the end of this second experiment, the heat tape used to heat the length of tubing between the gas pre-heat and the nebulizer failed. This is a common problem with heat tape as a result of poor contact between the thin heating element and the tubing, creating hot spots above the safe operating temperature. After this failure, the temperature reading at the nebulizer inlet dropped to 130°C. As a result, the signal decreased slightly, but the

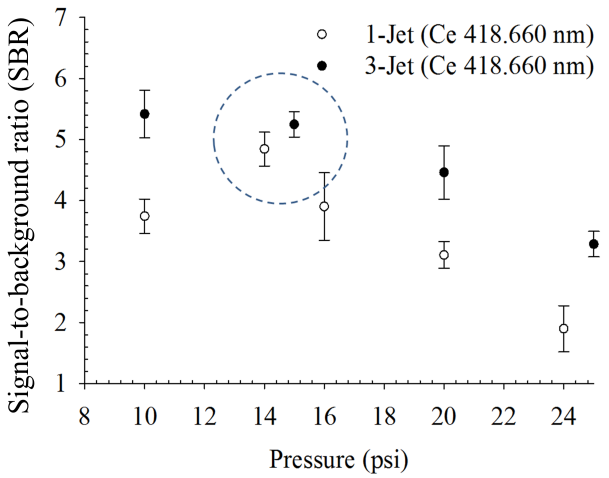

Figure 5.7: Comparison between the 3-jet and 1-jet nebulizer systems as a function of gas pressure.

system continued to function well overall. This heat tape is prone to failure (two failed prior to closing the glovebox during the initial testing), and replacing the heat tape within the glovebox proved to be challenging due to limited dexterity and dust formation. Since the signal did not change significantly, this heating element was omitted from the system to reduce complexity and replacement downtime.

Several observations were made about the aerosol-LIBS system following these initial shakedown tests: (1) the quartz windows had developed a thin film or etch that needed to be removed in order to maintain a good optical path, (2) the Deacon 770-L seal material at 500°C continued to off gas and eventually disappeared, thus leading to increased leaking of threaded joints and increased oxide formation and corrosion, (3) the system needed to be more easily disassembled for cleaning between runs, and (4) increased filtration was necessary to prevent the loss of material. For these reasons, along with the continued particle interaction with the laser, it was deemed necessary to make additional modifications to the aerosol-LIBS design.

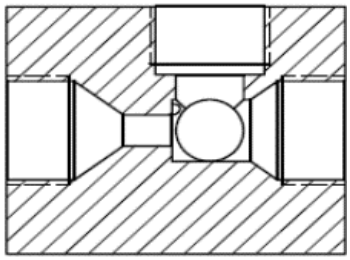

Figure 5.8: Cross section of the improved sampling chamber design.

5.1.2 Final System Design

The main modification to the system was made to the sampling chamber. Figure 5.8 shows a cross section of the new design. In this design, the NPT fittings were all replaced with welded joints eliminating off-gases from the seal materials as well as potential leaks. To reduce the number of aerosol droplets that interfere with the laser light, a sudden expansion was implemented into the sampling chamber to reduce the spread of the aerosol until after the sampling volume. The inside diameter of the nozzle portion was 6.3 mm and the inside diameter of the chamber was 12.5 mm. As a result of this design, significantly fewer particles are expected to fill the sampling chamber volume. The nozzle design was compared with the previous sampling chamber design using an aqueous system with LED lighting. Figure 5.9(a) shows the flow through the old sampling chamber. Here, the aerosol-gas stream expanded into the chamber and was shearing off at the exit creating eddies. Figure 5.9(b) shows the improved nozzle design under the same conditions. In this new modification, the flow was significantly more stable. In order to better visualize the phenomenon in these tests, the windows were not in place, and as a result, the actual flow within the chamber might be different. However, it illustrated the advantage of the new design.

Another change to the sampling chamber was in relation to the optical windows. A 1/2 NPT sight glass window from TATE-JONES Inc, was found that uses a 19 mm diameter quartz window insert (6.3 mm thick) sandwiched between Grafoil seals which were compressed to form a seal by a threaded ring. The inside diameter of the threaded ring provided

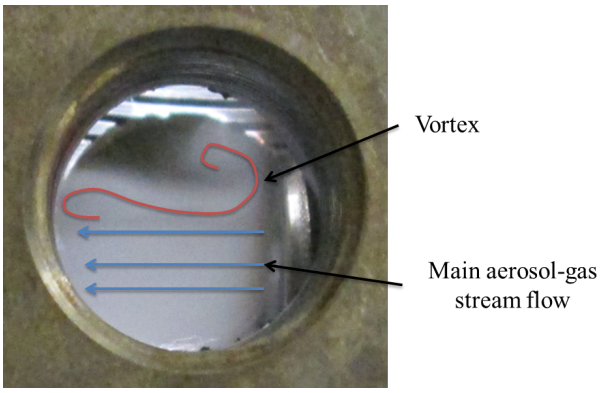

(a)

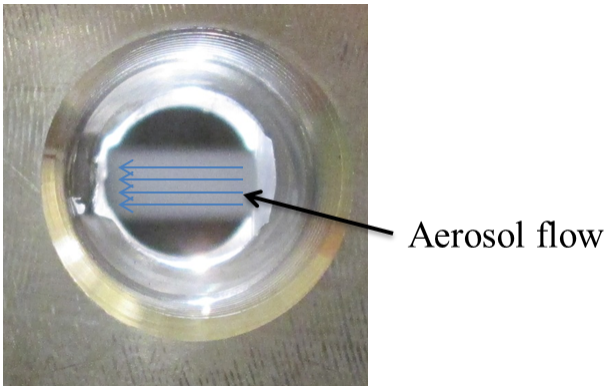

(b)

Figure 5.9: (a) Aqueous test of the old sampling chamber design and (b) the aqueous test done using the sudden expansion.

a clear optical window that was 12.7 mm in diameter. To streamline the sampling chamber and to eliminate the NPT threads, a threaded pocket similar to the NPT sight glass windows was built into the sampling chamber itself. With this design, the threaded ring, which was not in contact with the salt in any way, could be removed easily along with the window and seals. This design offered several key advantages: (1) the windows did not extrude out of the chamber and thus insulation could be easily added and removed between experiments without significant dust formation, (2) the windows could easily be replaced/cleaned after each experimental run and (3) the inside of the sampling chamber could be accessed for easy cleaning and salt sampling. Sapphire windows of the same diameter (but 3 mm thick) were purchased from Meller-Optics and used interchangeably with the quartz windows.

The modifications to the sampling chamber design itself should reduce particle interaction; however, in addition to those changes, a 3X beam expander was developed and installed into the optical configuration. Here, the Q-smart 450 Nd:YAG laser was mounted vertically on the outside of the glovebox and the laser light was directed via mirrors into the glovebox through a quartz window located in the glovebox wall. A laser mirror within the glovebox directed the laser light downwards through a 3X beam expander that was made by aligning a -25 mm plano-concave lens and a 50 mm plano-convex lens (25 mm apart). Expanding out the laser would reduce the impact that a single droplet will have on the overall energy as well as decrease the likelihood of a premature breakdown. This should reduce the effect of a shift in the plasma location from shot-to-shot. Following the 3X beam expander, the laser light was focused through a 75 mm focal lens into the sampling chamber. The focused laser light created a plasma in the center of the sampling chamber. Light from the plasma was collected via a f = 75 mm lens and then focused (f = 100 mm lens) into the 4 m long fiber optic cable. This optical path is shown in Figure 5.10. The fiber optic cable carried the light to a Michelle 5000 spectrometer and iStar ICCD detector located outside of the glovebox.

To reduce the leaking of the nebulizer lid and jar, custom grafoil seals of 48.2 mm inside diameter by 53.6 mm outside diameter by 3.1 mm thick were purchased from Industrial

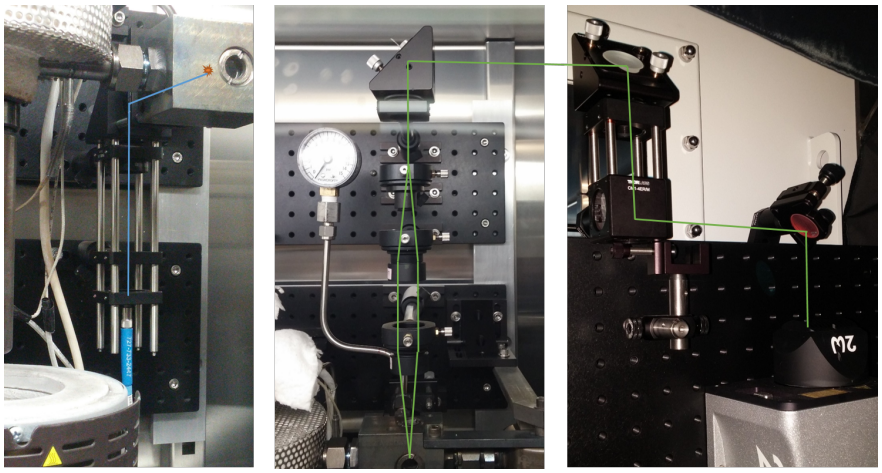

Figure 5.10: Photos showing the optical configuration: (right) laser mounting and quartz window, (center) laser mirror and 3X beam expander into the sampling chamber, and (left) plasma light collection path into the fiber optic.

Packing and Seal, Inc. Prior to use, these seals were held at 500°C for 6 hours to out-gas any impurities possibly contained in the material. The threaded joint between the nebulizer shaft and tip was sealed using a fine sliver from the graphite impregnated cord that was approximately 10 inches long. This fine graphite cord was wrapped around the threads prior to attaching the nebulizer tip. When the nebulizer tip was attached, this material was compressed between the threads to create a stable seal.

To address the issue of material loss, an additional filter from United Filtration Inc, was purchased and placed in series with the first filter. The first filter in the series was the 1.0 μm filter and acts as a coalescence filter to remove the molten droplets from the gas stream. The second filter was a 0.5 μm filter and was set to capture particles after they had frozen. In addition to this change, the gas cooling heat exchanger, which would be needed if operating at 20 L/min, was removed from the system because the actual flow rates were significantly less (0.3 L/min to 1.5 L/min), and enhanced cooling was unnecessary. In the removal of the heat exchanger, a large quantity of salt was found deposited in the tubing (leading to the HX) from the previous experiments.

Most of the insulation used in the previous design was maintained. However, in this design, the insulation surrounding the sampling chamber and the 1.0 μm filter was constructed

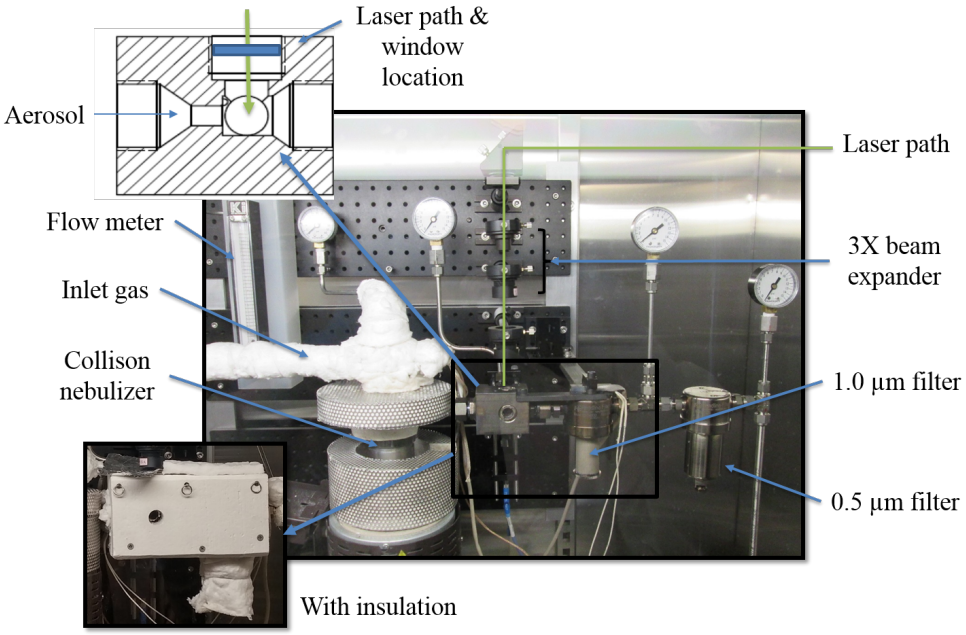

Figure 5.11: Photo of the final molten salt aerosol-LIBS design.

of 25 mm thick alumina silicate insulation board that had been constructed to form a box. Placement and removal of the insulation was easily accomplished using 10 cm stainless steel pins. The lid of the box was placed on top of the sampling chamber and the insulation box was slid up around the sampling chamber and held with the stainless steel pins. To reduce dust formation, stainless steel mesh was placed on the inside surfaces of the box. Small gaps in the insulation were filled with alumina silicate fibers. Figure 5.11 shows a picture of the final design of the aerosol-LIBS system complete with the insulation box described above.

5.2 Molten Salt Cerium Experiments

5.2.1 Material and Methods

Molten salt experiments using $CeCl_3$ as a surrogate material were done in a LiCl-KCl eutectic salt to test the final aerosol-LIBS design. Salt samples were made using $CeCl_3$ (99.99%),

LiCl (99.99%), and KCl (99.95%) purchased from Alfa Aesar. The LiCl and KCl salts were mixed at the eutectic ratio (44 wt% LiCl and 56 wt% KCl) and the $CeCl_3$ composition was varied from 0 wt% to 5 wt%. Salts were prepared in the inert atmosphere glovebox by first mixing the LiCl and KCl beads together and allowing them to dry at 300°C for 2 to 12 hours in a stainless steel crucible. Following this drying process, the furnace was ramped up to 500°C to melt the salt for 1 hour before it was removed and allowed to freeze. The $CeCl_3$ was then added to the top of the frozen LiCl-KCl salt and then remelted for at least 3 hours to ensure a homogeneous mixture. To reduce the amount of salt required overall, only 30 g of total salt per experiment was used. Since the nebulizer shaft and tip were fixed to the nebulizer lid via a stainless steel swagelok fitting, the gap between the bottom of the jar and the nebulizer tip could not be adjusted. Thus, any solid material in the jar would prevent a proper seal from being made between the jar and nebulizer lid. As a result, the empty jar was first sealed and then the solid salt sample was added through the nebulizer spout. Because the prepared salt ingot was too large to be loaded in this way, a pair of pliers (wire cutters) was used to break up the ingot into 2 mm to 4 mm chunks that could fit through the spout.

Throughout operation of the aerosol-LIBS system, the pressure drop across the 1.0 μm filter increased initially to approximately 4-5 psi as a steady state condition (typically after 10 minutes). The nebulizer operation was controlled by adjusting the input pressure to maintain a 12 psi pressure differential between the nebulizer input and sampling chamber. The operating temperatures of the system are shown in Table 5.1. The laser energy used was 50 mJ, which is significantly lower than the 90 mJ optimal; however, to prevent damage to the sapphire and quartz windows, a lower laser energy was required.

In the first experimental set, the gate delay was studied between 100 ns and 25 μs. For each variation, 3 repetitions were completed, each comprised of 250 laser shots at 2 Hz. The gate width was 300 μs. The 250 spectra from each repetition were averaged to provide a single representative spectrum. Following the optimization test, experiments were conducted

Table 5.1: Operating temperatures of the different components in the Aerosol-LIBS system.

Gas pre-heat furnace	550°C
Gas inlet of the nebulizer	130°C
Salt in the nebulizer	470°C
Sampling chamber	260°C
1.0 μm filter	500°C
0.5 μm filter	60°C

Table 5.2: Table of the different molten salt experiments conducted at different wt% of $CeCl_3$.

Experiment number	wt% $CeCl_3$	Date conducted
MS4	3.0	March 25, 2016
MS5	3.0	April 5, 2016
MS6	0	May 10, 2016
MS8	0.1	June 2, 2016
MS9	0.5	June 4, 2016
MS10	1.0	June 7, 2016
MS11	1.0	June 16, 2016
MS12	3.0	June 24, 2016
MS14	5.0	July 1, 2016

to generate calibration curves for $CeCl_3$. In this experimental series, 300 shots were recorded and averaged over 7 repetitions. A summary of the experiments conducted is shown in Table 5.2. The experiments are named MS#, where MS stands for Molten Salt. The first three experiments were done in the initial testing and shakedown period as described above. In experiment MS7, a new optical port configuration was tested that yielded extremely low intensities and poor %RSD's. As a result, MS7 was not included in this study. Experiment MS13 was also not included because there was significant oxide formation due to an oxygen spike in the glovebox and the spectral results and carrier gas flow were unreliably low even after normalization. Two sets of data were collected for MS14; the first was collected in the first hour of running and the second after 5 hours of running.

Following each experiment, the system was disassembled and all of the salt deposited on the different surfaces was scraped free and recovered. All of the recovered salt mass and system components were weighed for material accountancy. With the addition of the second filter, typically all but 0.25 g of material could be accounted for. This amount, was likely

contained in the larger stainless steel components as a surface film (this was difficult to remove via scraping). The large components could not be weighed with enough precision to account for this salt. The salt recovered in the different locations was reserved for ICP-MS analysis. After the different components were scraped of salt, they were washed in nanopure water and dried in acetone. In addition, the sapphire windows were removed following each experiment and washed with nanopure water and acetone.

Salt samples reserved from the various locations within the aerosol-LIBS system were prepared for the ICP-MS analysis. These samples were made by weighing out between 0.01 and 0.03 g of salt and dissolving it into 10 mL of 2 % nitric acid for at least 2 hours. Following each dissolution, samples were diluted between 500X and 1000X in order to get the Li concentration in the solution to below 500 μg/L. Prepared samples were run using the Agilent 7900 ICP-MS instrument.

5.2.2 Results and Discussion

Experiments were conducted to explore the spectral decay with respect to the gate delay of the spectrometer. In the first experiment, the gate delay was varied from 100 ns to 9 μs. This range was expected to yield the optimal gate delay; however, results indicated that perhaps a larger gate delay was necessary. Consequently, a second experiment was conducted ranging the gate delay from 1 μs to 25 μs. Results from the two gate delay experiments done at 3 wt% $CeCl_3$ are shown in Figure 5.12. As the gate delay increases, the SBR increases until 16 μs and then slowly decreases. As a result, 16 μs was selected as the optimal value.

A representative spectrum obtained from the molten salt aerosol-LIBS system is shown in Figure 5.13. Here, the Li and K peaks can be easily identified along with multiple Ar peaks (not marked in the Figure). Notable cerium peaks are the Ce 418.660 nm, Ce 428.990 nm, and the Ce 457.228 nm lines. These lines were selected using the NIST database due to their intensity and low interference with other lines.

As a result of the modifications made to the aerosol-LIBS design, the plasma location

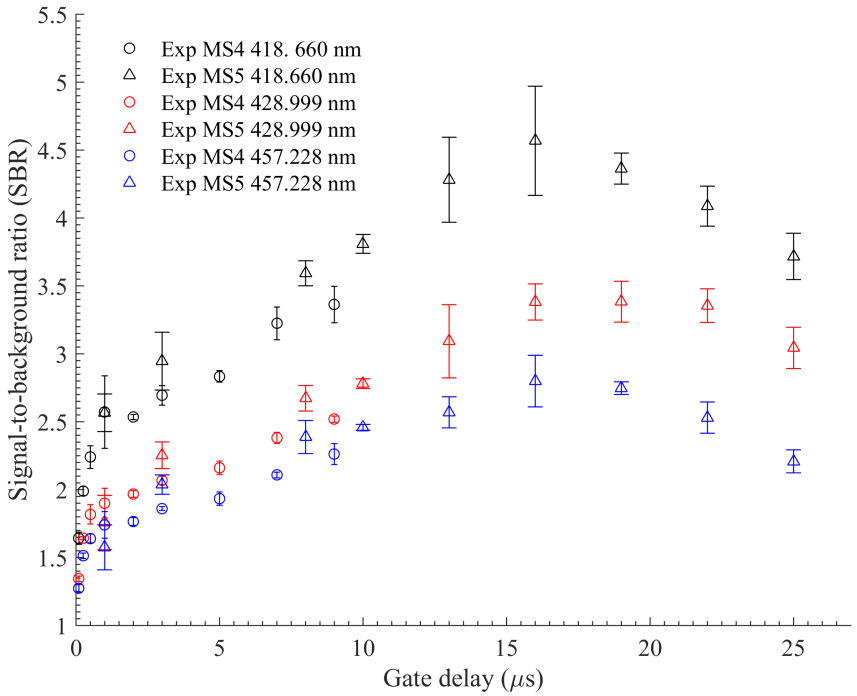

Figure 5.12: Optimization of the gate delay with respect to the SBR.

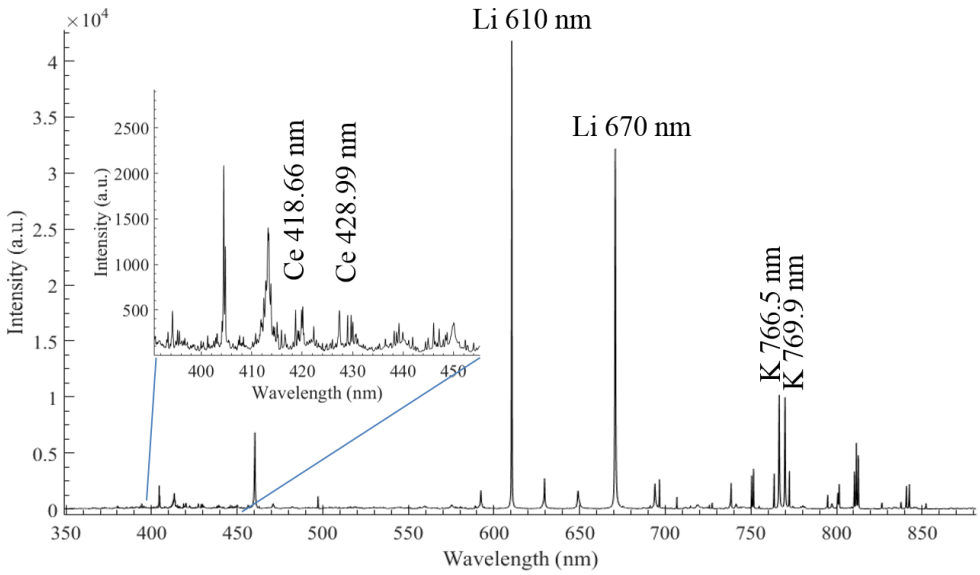

Figure 5.13: A representative spectrum collected in the 3 wt% $CeCl_3$-LiCl-KCl salt at a 16 μs gate delay.

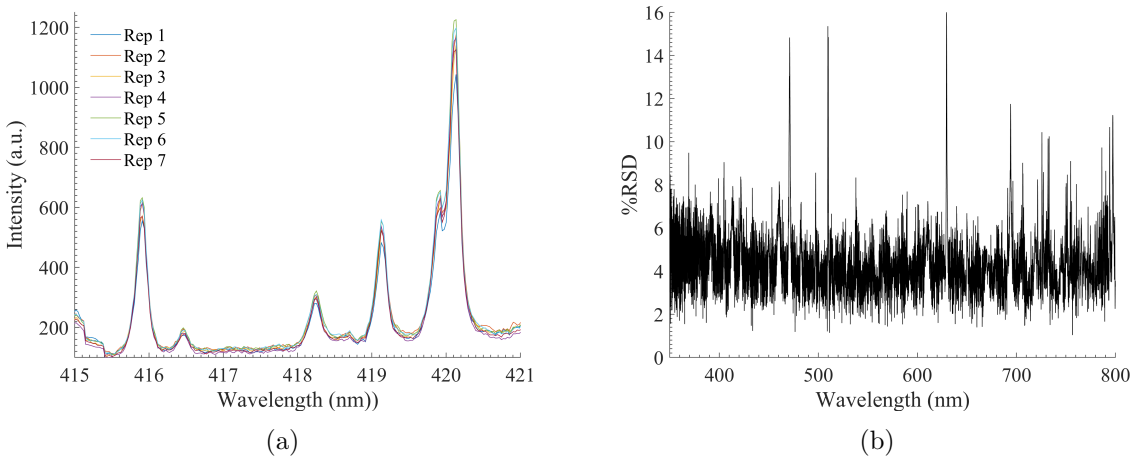

Figure 5.14: (a) Spectra near the 418.660 nm line at 0.1 wt% $CeCl_3$ (b) the %RSD between the 7 repetitions studied with no normalization.

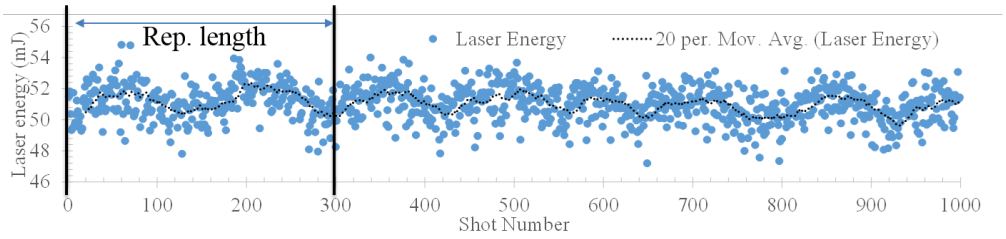

Figure 5.15: The laser energy as a function of the shot number.

varied less and fewer particle interactions were observed. A representation (MS8 at 0.1 wt% $CeCl_3$) of typical overall repeatability of the system is shown in Figure 5.14. The variation between repetitions is small as observed in Figure 5.14(a) for the spectral region near the Ce 418.660 nm line. For this experiment, the %RSD values for the spectral region from 350 nm to 800 nm are on an average of 4.8% (see Figure 5.14(b)). This has a slight improvement over the aqueous system. It is anticipated that the largest source of variation in the system comes from fluctuations in the laser energy. Indeed, Figure 5.15 shows the laser energy fluctuation with respect to the shot number. There is approximately 10% variation from shot to shot; however, there is also a large sinusoidal oscillation with a period of 150 shots. To reduce variation as a result of the oscillation, two periods or 300 shots have been used in this study.

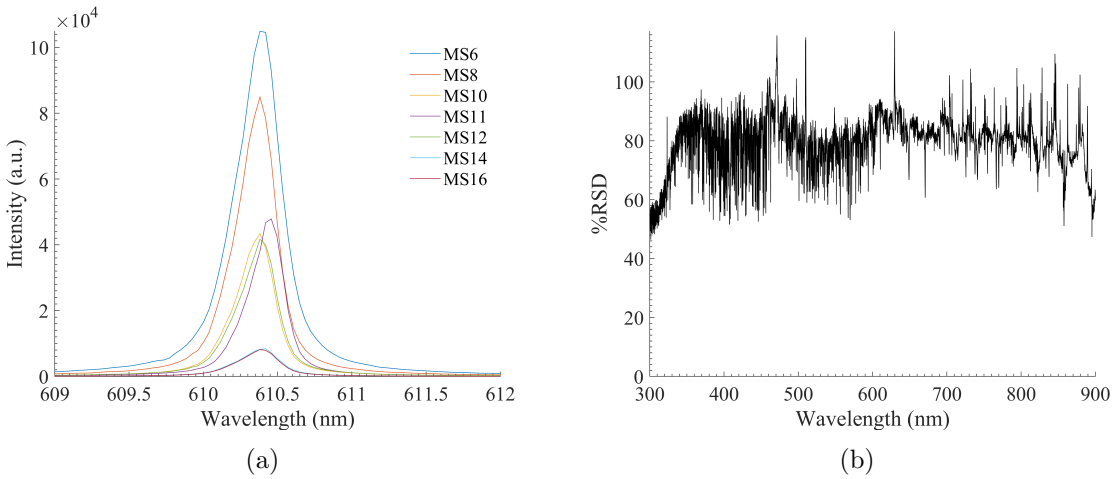

Figure 5.16: (a) The Li 610.3 nm line for the different experiments run over a period of 3 months and (b) the %RSD between the experiments over time.

Next, the repeatability of the system over time was explored. Figure 5.16(a) shows the signal response over time. It is clear that the overall intensity of the spectra decreases with time. This is due to degradation of the optical setup as a result of dust, insulation off-gas, and vibrations. The surface films on the optics were removed periodically; however, some loss in signal resulted over time. Figure 5.16(b) shows the %RSD over time between the mean spectra under different experiments. This illustrates that the signal loss is across the entire spectrum. The high %RSD values between 300 and 500 nm make sense due to the change in the Ce concentrations. For this study to have a meaningful discussion from a calibration perspective, a normalization method is necessary. For application of the aerosol-LIBS technique to measure molten salts in the electrorefiner, a method is needed to reduce the degradation effect on the optics. This may require the periodic replacement of optical components or a gas protective layer between the system and the optics.

Elements in the sample that are candidates to use for normalization are Li and K since they are present in large quantity and their concentrations do not change significantly from experiment to experiment. The K peaks at 766.5 and 769.9 nm can be used; however, Hanson et. al[9] reported that the K lines were prone to self-absorption. Therefore, Li lines were used

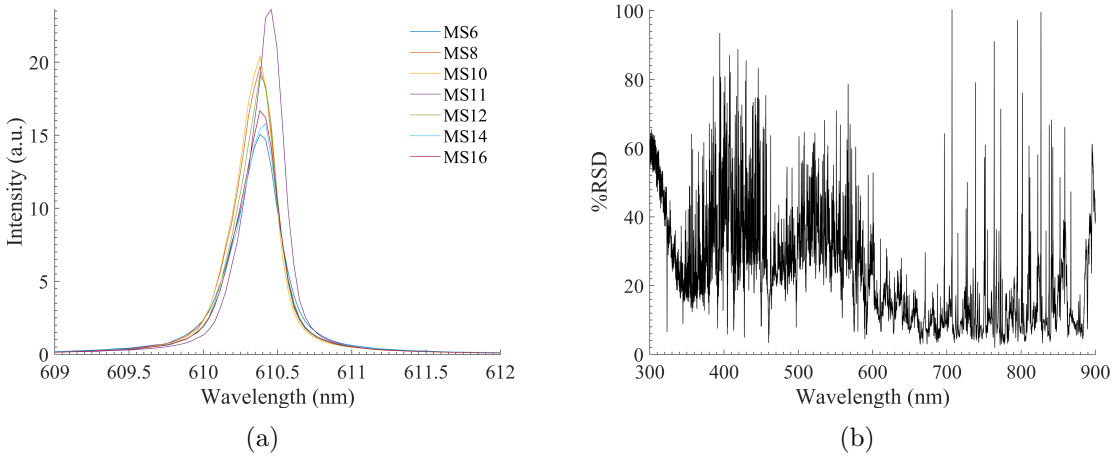

Figure 5.17: (a) The normalized Li 610.3 nm line for the different experiments run over a period of 3 months and (b) the %RSD between the normalized experiments over time.

as an internal standard to normalize the spectra. In this case, each individual spectrum was divided by the averaged intensity from 459 nm to 461 nm. This wavelength range covered the Li 460 nm peak. Figure 5.17 shows the normalized spectra and %RSD values for the experiments. The spectra still had high %RSD's where the majority of the Ce lines were as a result of the varying concentrations; however, the region between 600 nm to 900 nm had significantly reduced %RSD's with an average of 15%.

Based on the normalization method, it is important to check the precision of the measurement by evaluating the %RSD values between repetitions for the different experiments. Table 5.3 shows the calculated %RSD between the repetitions using both the peak area and the peak intensity. With the exception of the MS6 and MS8 (0 wt% and 0.1 wt%) results tabulated for the peak areas (see Table 5.3, first two rows), the %RSD results were on the order of 2-10% whereas the %RSD values were under 7% based on the peak intensity analysis.

Results from the ICP-MS analysis are shown in Table 5.4. In many instances, salt samples were not collected from the system and ICP-MS measurements were not obtained and labeled 'n/a'. The bulk measurement came from the nebulizer jar following the experiment. The

Table 5.3: The %RSD between the different repetitions taken for the $CeCl_3$ experiments.

%RSD from peak area			
	Ce 418.660 nm	Ce 428.999 nm	Ce 457.228 nm
MS6	210.0	57.9	107.7
MS8	24.8	20.0	32.0
MS9	4.8	9.0	13.3
MS10	4.9	3.8	9.4
MS11	5.0	5.0	6.5
MS12	3.5	3.3	4.7
MS14 (a)	5.5	4.5	7.0
MS14 (b)	6.9	7.1	8.4
%RSD from peak intensity			
	Ce 418.660 nm	Ce 428.999 nm	Ce 457.228 nm
MS6	3.2	5.6	1.6
MS8	6.0	6.3	4.6
MS9	3.3	5.5	2.9
MS10	5.3	4.8	3.3
MS11	2.8	3.7	1.9
MS12	4.0	2.3	3.5
MS14 (a)	4.7	3.6	3.7
MS14 (b)	6.7	5.7	6.0

sampling chamber and filter measurements were scraped from these respective components. Of the data collected, the general trend was that the concentration of Ce would drop slightly throughout the system. That is, the further the aerosol traveled from the nebulizer, the lower the concentration of Ce would be in the aerosol stream.

Univariate Calibration Curves

Spectra from each experimental repetition were analyzed using the MATLAB GUI shown in Appendix A. Figures 5.18, 5.19, and 5.20 show the calibration curves generated from the peak areas and peak intensities. Concentrations shown in those curves are obtained from the ICP-MS bulk measurements. The data point at 0.22 wt% Ce (MS9) does not follow the same linear trend as the other data points. This deviation might be from the fact that MS9 was run at a slightly higher energy range (55-60 mJ); thus, this point showed a slightly higher intensity response despite after being normalized. The R^2 values, regression fits, and

Table 5.4: ICP-MS results from the Ce molten salt experiments, n/a values were not collected or no materials were available from the system for testing.

Experiment #	Bulk (wt% Ce)	Sampling Chamber (wt% Ce)	1.0 μm Filter (wt% Ce)	0.5 μm Filter (wt% Ce)
MS5	1.676	n/a	n/a	n/a
MS6	0.0004	n/a	0.004	n/a
MS8	0.0315	n/a	0.0065	n/a
MS9	0.2245	n/a	0.1195	n/a
MS10	0.500	n/a	0.2625	n/a
MS11	0.450	0.489	n/a	n/a
MS12	1.612	1.484	1.277	n/a
MS14	2.637	2.589	2.330	2.605

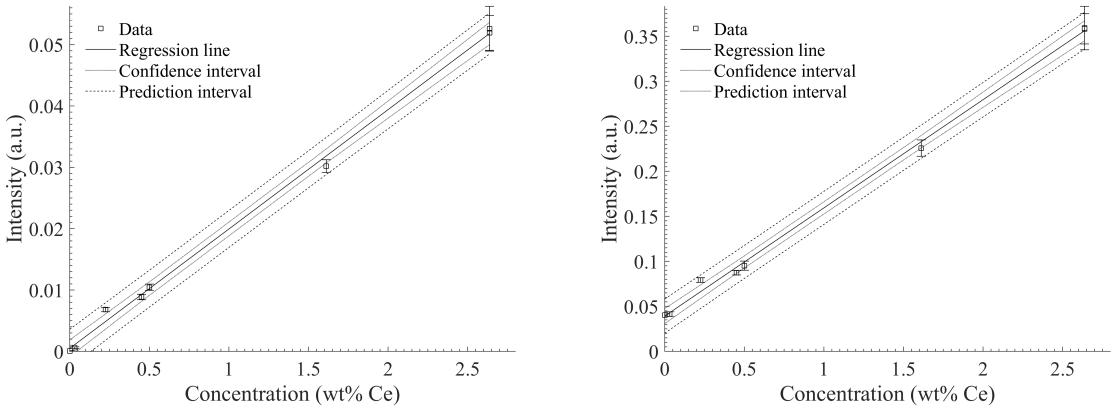

Figure 5.18: Calibration curves for the molten salt Ce experiments using (a) peak areas and (b) peak intensities for the Ce 418.660 nm line.

LOD for the three curves are summarized in Table 5.5. Between the different lines, the slope for the 418.660 nm line was the steepest followed by the 428.999 nm line. This outcome indicates that the 418.660 nm line has the greatest sensitivity and the best overall LOD is 148 ppm obtained from the 418.660 nm curve generated using the peak area method.

The above calibration curves were cross validated using a LOOCV approach. This analysis was applied and conducted to explore the accuracy of the calibration curves. For the sample left out, the % error was calculated between the predicted and ICP-MS measured concentrations. Being that there are fewer points, the regression coefficients did shift slightly

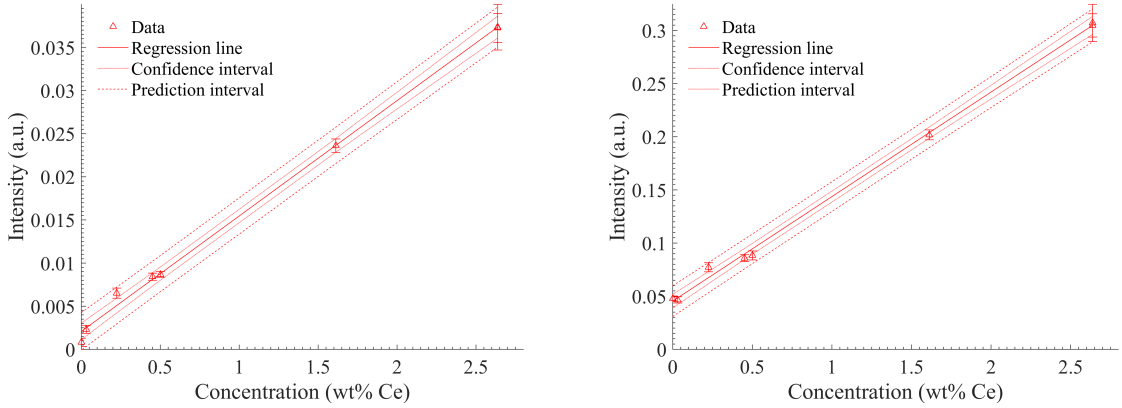

Figure 5.19: Calibration curves for the molten salt Ce experiments using (a) peak areas and (b) peak intensities for the Ce 428.999 nm line.

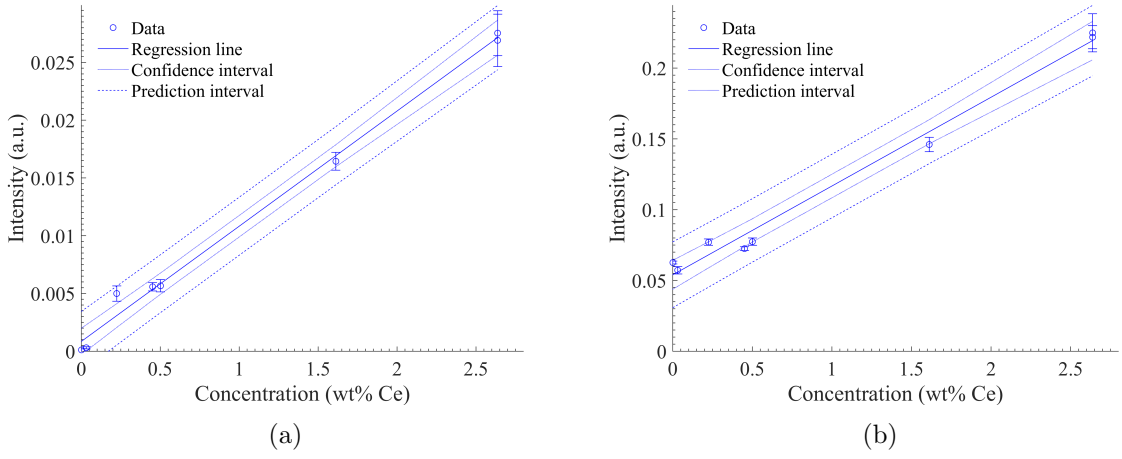

Figure 5.20: Calibration curves for the molten salt Ce experiments using (a) peak areas and (b) peak intensities for the Ce 457.228 nm line.

Table 5.5: Regression coefficients and LOD for the univariate calibration curves for Ce in molten salt. Generated using the normalized spectra.

Peak Area	R^2	$S_{y/x}$	b_1	b_0	LOD (wt%)	LOD (ppm)
418.660 nm	0.9976	0.0011	0.01945	0.00049	0.0148	148
428.999 nm	0.9975	7.965e-04	0.01337	0.00209	0.1060	1060
457.228 nm	0.9938	9.529e-04	0.00997	0.00084	0.0339	339
Peak Intensity						
418.660 nm	0.9977	0.0070	0.12014	0.03922	0.0328	328
428.999 nm	0.9980	0.0053	0.09832	0.04539	0.0811	811
457.228 nm	0.9875	0.0085	0.06271	0.05398	0.0485	485

Table 5.6: % Error between the predicted concentration and the ICP-MS concentration for the LOOCV analysis. % errors for MS6 are not shown but are greater than 2,000%.

Peak Area								
Peak (nm)	MS8	MS9	MS10	MS11	MS12	MS14(a)	MS14(b)	RMSECV
418.660	110	54	2.6	5.4	6.3	0.36	2.7	647
428.999	57	58	1.78	5.9	0.2	0.55	0.079	659
457.228	366	103	4.1	6.2	3.6	2.5	1.6	1048
Peak Intensity								
418.660	54	59	8.9	13	4.3	1.2	1.7	625
428.999	82	54	15	10	1.6	0.013	1.5	578
457.228	80	78	30	41	10	2.5	6.0	1503

as points were left out. The greatest variation was when the lowest concentration points were left out, and then, the change was marginal. Results of the LOOCV study are shown in Table 5.6. The % error's for the lower concentration range (MS6, MS8 and MS9 sampling results) are very poor though residuals are small. However, for samples containing at least 1 wt% $CeCl_3$, the % error's are mostly within an acceptable range. When comparing between the curves calculated from the peak areas and peak intensities, the peak area method has better % errors overall. The RMSECV between the different curves are similar between the peak area and peak intensity cases overall.

To determine the best univariate calibration curve, all of the FOM were evaluated. In this case, the Ce 418.660 nm line performed best overall and thus will be evaluated here. The precision and repeatability of the measurements were significantly better in the lower range for the peak intensity response. However, in the mid and upper range the differences

between the two are minor with the peak intensity %RSD's being slightly better overall. In terms of accuracy, the peak area calibration curve performed better overall. That being the case, the low concentrations studied here (0 wt% and 0.1 wt%) were too low to be accurately measured with the aerosol-LIBS system at this stage. The LOD outcomes between the two systems were slightly better for the peak area calibration curve (148 ppm vs. 328 ppm). As a result of the above FOM, the 418.660 nm line performed better overall and would be recommended for use in future analysis. For this line, the RMSECV was calculated to be 0.0647 wt% or 647 ppm.

PLS Calibration Model

For all the experimental runs, a multivariate PLS model was generated using the PLS_Toolbox in MATLAB. Here, seven repetitions per experiment were divided into a calibration set (4 repetitions) and a validation set (3 repetitions). The calibration set had 33 spectra and the validation set had 20 spectra. Prior to processing the spectra in the model, each spectrum was normalized with respect to the Li 460 nm line. The number of latent variables was chosen to reduce the RMSECV. Figure 5.21 shows the relationship between the LV values and the RMSECV. The PLS_toolbox suggested 5 LV be used; however, seven were selected in order to further reduce the RMSECV to 0.0622 wt% Ce (that is, 622 ppm). This may mean the model is slightly over-fit. Figure 5.22 shows the calibration curve generated using this model. Overall, the model fits very well with some spread in the data as a result of the deviations between repetitions. In addition, the MS9 data point fits the linear trend as a result of using the entire spectrum and multiple data points in the modeling method.

The validation spectra set was used to explore the accuracy of the model. Figure 5.23 shows the fit of the validation data set with respect to the PLS model. Visually, the PLS model has performed well. When comparing the residuals between the measured and predicted values as shown in Figure 5.24(a), it is apparent that the majority of the results are within approximately 0.1 wt%. The RMSEP is 0.0762 wt% Ce or 762 ppm. Figure 5.24(b)

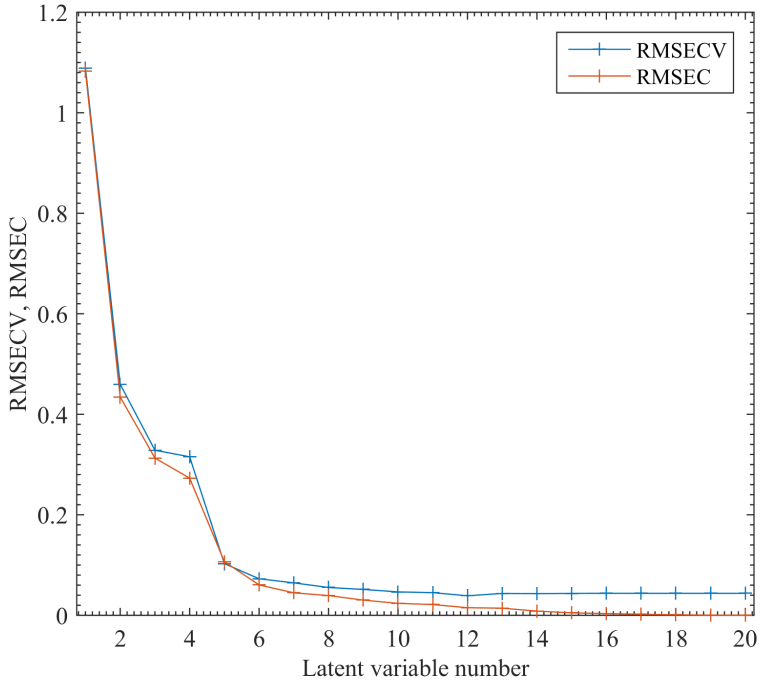

Figure 5.21: PLS model response as a function of the latent variables and the RMSECV.

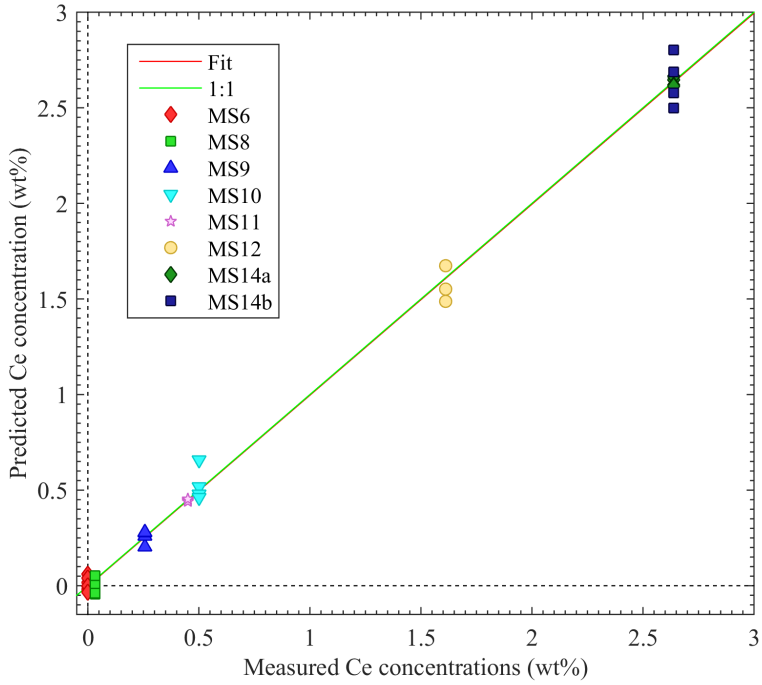

Figure 5.22: PLS model calibration curve for Ce in molten salt.

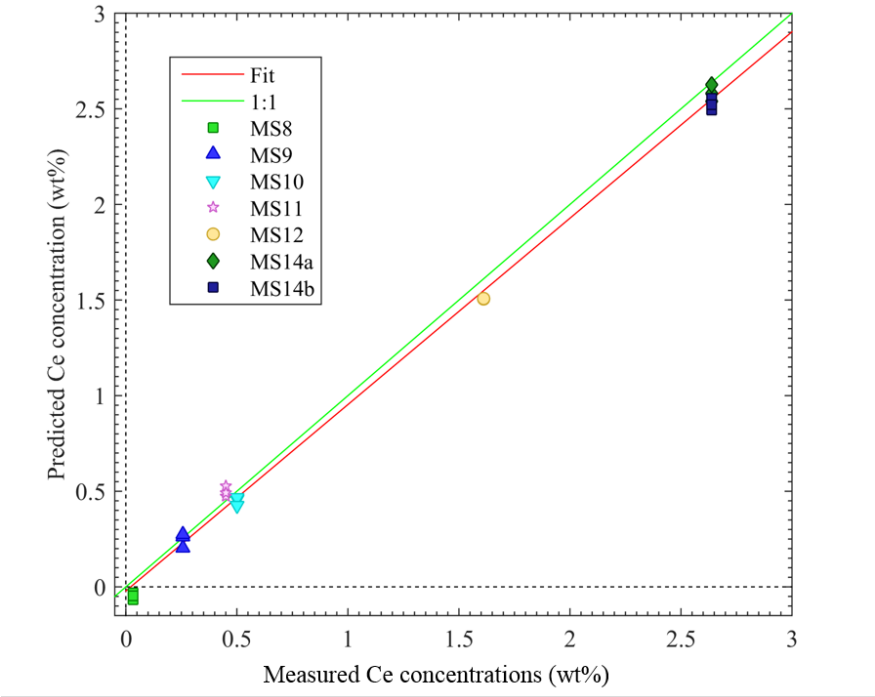

Figure 5.23: Validation curve for the PLS model

shows the % error between the predicted and measured concentrations. The average % error between the repetitions were 254%, 10%, 10%, 10%, 6.6%, 2.1%, and 4.3% for the MS8, MS9, MS10, MS11, MS12, MS14(a), and MS14(b) experiments, respectively. This result indicates that the model, on average, can predict the concentration to within 10% for concentrations around 1 wt% $CeCl_3$ or greater.

Between the univariate and multivariate calibration models, the difference between the predictions were small. The RMSECV values were 647 ppm and 622 ppm for the univariate and multivariate approaches, respectively. Both the univariate and PLS calibration models could not accurately quantify Ce in samples containing less than 1 wt% $CeCl_3$, though the only data points below this limit were at 0.03 wt% Ce (MS8) and 0.22 wt% Ce (MS9). As discussed above, MS9 did not fit well with the rest of the data due to being run at a higher laser energy; so this data point might not provide a good representation of the system accuracy. At MS8, the concentration was too low to be measured with any confidence. As a

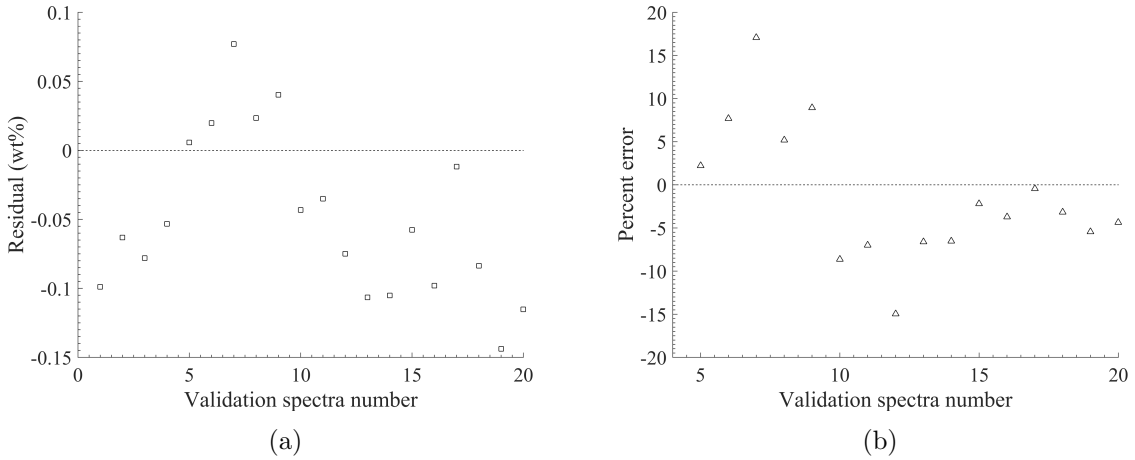

Figure 5.24: (a) The residuals between the predicted and measured concentrations for the validation data and (b) the percent error between the predicted and measured data. The first three data points had approximately 300% error and were not shown in the figure.

result, the true concentration range that can accurately be measured is likely between the 0.03 wt% Ce (MS8) and 0.45 wt% Ce (MS11). However, above this range, the analytical models performed well. Undoubtedly, analytical results would be better without the significant degradation in the spectral response over time; yet, despite the degradation, good results were achieved through the normalization method.

The analytical results for Ce in molten salt were compared to Ce work found in the literature. Martin and co-workers[90] studied Sr, Cs, and Ce in a $CaCO_3$ matrix to simulate fission product and actinide elements. Here, the authors used the PCA approach and were able to detect and distinguish between 100 ppm and 500 ppm concentrations (though the difference between these concentrations was small). Gong et al.[91] studied CeO_2 in a KCl matrix using a stand-off LIBS system. The LOD were estimated to be 460 ppm Ce and 610 ppm Ce for open path and through a shielded window, respectively. The aerosol-LIBS system had a LOD of 148 ppm which is within the reported range for Ce.

The question to be raised is if this concentration range is sufficient for analysis of ER salt in pyroprocessing. Typical rare earth concentrations within the ER are on the order of 1-2 wt%. This means that the aerosol-LIBS system described above could in fact perform

a quantitative analysis of the salt with accuracy on the order of 10% for most of the rare earth elements, assuming there are no specific spectral interferences associated with working with a multi-element sample. In addition, if the amount of a given element was below the measurable limit, it would be possible to monitor that element qualitatively (with amounts greater than the LOD) to observe shifts over time. The power of PLS, though not demonstrated with this simple salt matrix, was the ability to model multi-element systems with more accuracy than the univariate approach because the entire spectrum was used in the modeling. In the ER salt, where multiple fission products, rare earths, and actinides are present, the spectra would be complex and PLS modeling will be essential for analytical measurements.

5.3 Summary and Conclusions

The aerosol-LIBS system was successfully transitioned to high temperature operation of molten salt within an inert atmosphere glovebox. Initial shakedown testing of the system yielded several areas where modifications were needed. As a result, significant changes to the design were made. Specifically, in the sampling chamber and laser optics. Initial testing identified important design and operational criteria–such as the optimal laser energy. In addition, the optimal flow and pressure for a 1-jet and 3-jet nebulizers were also determined.

In the final aerosol-LIBS system design, Ar gas was heated to 550°C prior to being transferred through a length of insulated, but un-heated, tubing to the nebulizer. The salt was held at 470°C where it was nebulized using a 1-jet system. The sampling chamber had a sudden expansion to direct the aerosol flow and reduce particle interference with the laser light. In addition, the sampling chamber used sapphire windows with grafoil seals. To reduce material loss in the system, a series of two filters were used, the first with a 1.0 μm element and the other with a 0.5 μm element. The laser light at 50 mJ was expanded using a 3X beam expander before being focused into the sampling chamber via a 75 mm lens. This

design resulted in a stable aerosol generation and plasma formation.

The Ce concentration effect was studied between the range of 0.1 to 5 wt% $CeCl_3$. The precision and accuracy of the aerosol-LIBS analysis system was assessed using univariate and multivariate modeling approaches. The precision of the LIBS measurements were between 2 and 10% with a mean around 4% for the mid to upper concentration ranges studied. The samples at different concentrations showed a strong linear agreement overall between the spectral response and the concentration. In the univariate approach, the Ce 418.66 nm line had the best overall accuracy (approximately 5%) and lowest LOD down to 148 ppm and a RMSECV of 647 ppm. The PLS model had a RMSECV of 622 ppm and the validation results showed an accuracy of approximately 10%. Both calibration techniques performed well overall and showed that Ce in molten salt could be quantitatively measured in salt samples containing at least 1 wt% $CeCl_3$. This test has demonstrated that the molten salt aerosol technique is a viable method for measuring material concentrations within a molten salt despite challenges with degradation of the optics over time.

The successful completion of the surrogate Ce work (Phase III) has yielded an aerosol-LIBS system design that is capable of high temperature operation that is viable over time with normalization. As a result, no major alterations to the system are recommended prior to proceeding to the final phase working with UCl_3.

Chapter 6

Molten UCl_3-LiCl-KCl Salt Aerosol

The $CeCl_3$ experiments demonstrated that the aerosol-LIBS system has great promise for the on-line measurement and monitoring of molten salts used in the ER. However, additional studies are necessary using heavy elements which tended to be problematic due to the large number of spectral lines in LIBS analysis. In this case, depleted uranium (DU) was selected to further explore the aerosol-LIBS system as an analytical approach in pyroprocessing salt monitoring for safeguards applications.

6.1 Materials and Methods

Prior to working with uranium salt aerosol, a DU metal sample was analyzed using LIBS. The main purpose of this experiment was to gain insights to the complex U spectrum and to compare it with DU metal LIBS spectra reported in the literature. For this experiment, the same optical setup as described in Chapter 5 was used. In this case, the DU metal was placed where the sampling chamber would go. As a result, the optics were not optimized for a solid material and the resulting laser spot size was approximately 1 mm in diameter (which is quite large). As part of this work, the gate delay was explored at 1 μs, 5 μs, and 16 μs. Each studied gate delay comprised of 5 spots (repetitions), each consisting of 150 laser pulses. Figure 6.1 shows the DU metal sample used in this study.

For the aerosol experiments, the aerosol-LIBS system design and equipment were not changed in the transition from Phase III to Phase IV (Note: please see Chapter 5 for details of the design, optical configuration, and equipment). However, the optical components

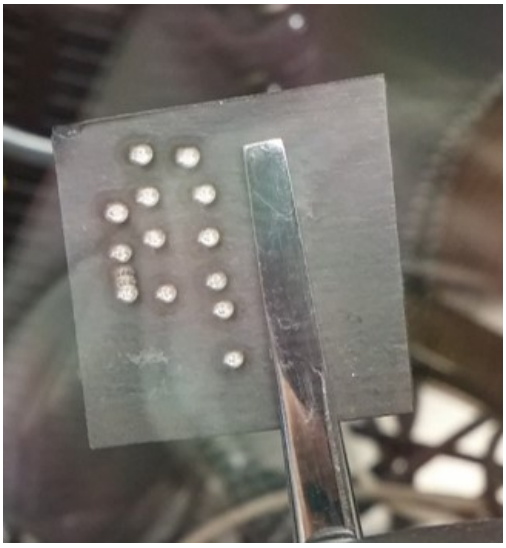

Figure 6.1: DU metal sample with the 15 sampling locations. The spot size is approximately 1 mm in diameter.

(lenses and mirrors) within the glovebox were removed and cleaned prior to the molten salt U experiments. With the re-assembly of the components, the alignment shifted slightly, resulting in a 20% loss in signal. In addition, with the re-assembly of the 3X beam expander, the beam profile shifted–resulting in hot spots which damaged the sapphire windows over time. Partial re-alignment was done to reduce the hot spots and increase the LIBS signal. However, due to challenges of working within the glovebox environment, the system was not re-aligned to the exact condition of operation as the cerium case.

Operating procedures and some system parameters were adjusted as a result of working with DU within the glovebox. The primary change was related to the disassembly and cleaning of components following each experiment. To reduce the spread of radioactive material and to decrease U waste, the system components were not removed from the glovebox and washed with nanopure water. The one exception to this was the sapphire windows, after being wiped with chem-wipes in the glovebox, the windows were transferred out and frisked with a Geiger counter to ensure no contamination. Following this, the windows were cleaned with water and acetone, inspected for damage, and then transferred back into the glovebox for re-assembly. The residual salts adhered to the stainless steel components following an

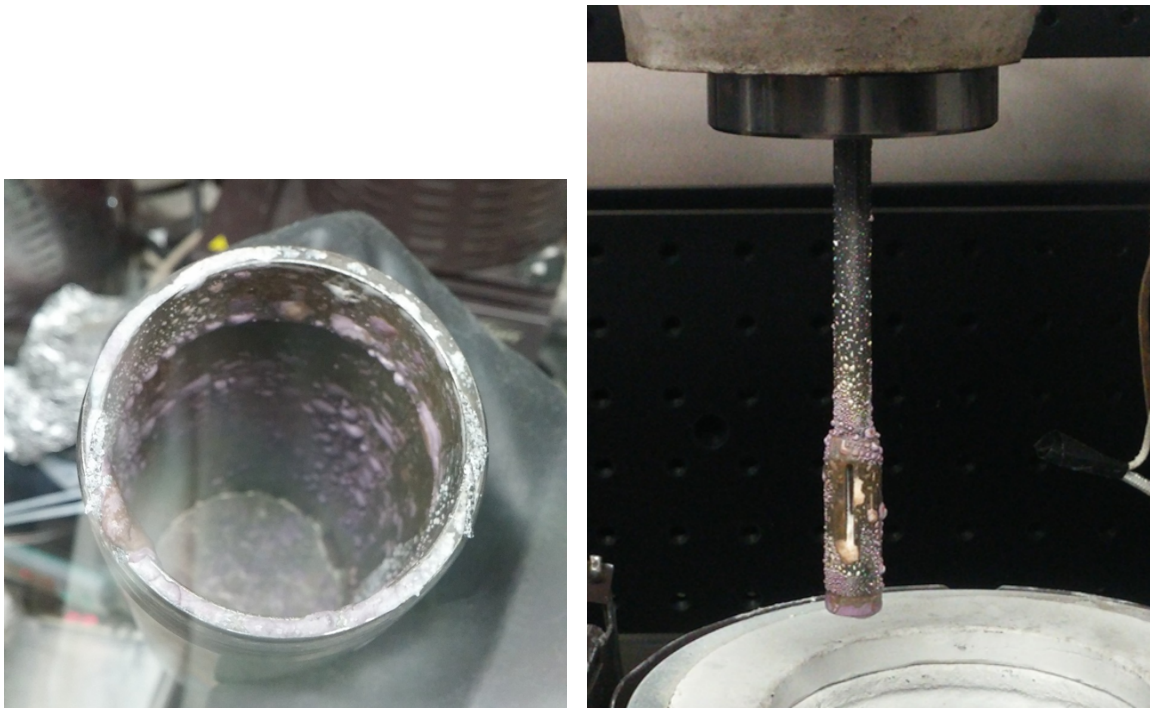

(a) (b)

Figure 6.2: Residual UCl_3-LiCl-KCl on (a) the nebulizer jar and (b) the nebulizer tip.

experiment were removed manually using hand scraping tools. Figure 6.2 shows examples of system components with adhered salt prior to scraping. In the scraping step, the majority of the material was removed; however, small amounts of salt deposited within the tubing remained. This salt, as well as dust generated from scraping, was removed using parafilm. The 1.0 μm filter could not be cleaned by scraping because of salt adhered within the different stainless steel layers. To prevent salt buildup and increased pressure drop, this filter was replaced for every experiment. The 0.5 μm filter was not replaced since the fine powder salt collected outside the filter was easily removed.

Depleted UCl_3 salt (74.4 wt% in LiCl-KCl eutectic) was acquired from the Idaho National Laboratory. Other salts used were LiCl (Alfa Aesar, 99.99%) and KCl (Alfa Aesar, 99.95%). The LiCl and KCl salts were mixed at the eutectic ratio (44 wt% LiCl and 56 wt% KCl) and dried at 250°C for 2-12 hours in a stainless steel crucible. After drying, the LiCl and KCl salts were melted at 500°C for 1 hour before being removed to cool. The depleted UCl_3

(a) (b)

Figure 6.3: (a) Molten UCl_3-LiCl-KCl at 500°C and (b) the solid salt product after melting.

salt was then added on top of the solid LiCl-KCl salt prior to melted at 500°C for 3 hours to ensure a homogeneous ternary salt had formed. Figure 6.3(a) shows a picture of the prepared salt while still molten. Before the ternary salt had solidified, a cold stainless steel rod was inserted into the salt to draw a small sample for ICP-MS analysis. Often a thin oxide layer was observed on the top surface of the salt. This oxide layer formed as a result of small amounts of O_2 and H_2O within the glovebox and from corrosion of the stainless steel crucible. Before collecting the ICP-MS sample, the oxide layer was pushed to the side revealing the clean salt below. Both the stainless steel rod and the oxide formation can be seen in Figure 6.3(a). Figure 6.3(b) shows the solidified salt. It should be noted that the salt has a dark purple color which is a characteristic of UCl_3. To load the prepared salt into the nebulizer through the spout, the salt was crushed using wire cutters as was done for the Ce case. Figure 6.4 shows the crushed ternary salt.

Following each experiment, salt samples were taken from 6 different locations throughout the aerosol-LIBS system. These locations are: (1) the nebulizer jar, (2) the nebulizer spout, (3) the sampling chamber nozzle, (4) the sampling chamber volume cell, (5) the 1.0 μm

Figure 6.4: Picture of the crushed UCl_3-LiCl-KCl salt prior to being loaded into the nebulizer.

filter, and (6) the 0.5 μm filter. The different sampling locations are shown in Figure 6.5 to provide a reference. The amount of salt recovered in these locations varied, in most cases at least 0.01 to 0.05 g of material were recovered. However, for the sampling chamber volume, typically 0.005 g was recovered. Salt concentrations at the different locations were measured using ICP-MS. For the ICP-MS sample preparation, between 0.005 and 0.03 g of material (0.02 g was standard) was put into 15 mL test tubes and dissolved in 10 mL of 5% nitric acid for at least 24 hours. Following dissolution, the samples were diluted between 100X and 3000X in order to get the expected concentration of uranium down below the EPA limit of 30 μg/L. The dilution factor varied based on the amount of salt originally dissolved and the expected concentration of the salt sample. The 5 wt% samples required a larger dilution factor to get below the EPA limit. In addition, samples from the sampling chamber with small amounts of dissolved salt, required less dilution.

For each of the UCl_3 concentrations studied, 6 repetitions were acquired, each comprised of 300 shots. The laser energy was set at 50$\pm$5 mJ and was operated at 2 Hz. The pressure was controlled in order to maintain a 12 psi differential pressure between the nebulizer inlet and the sampling chamber. With this pressure differential, the gas flow rate was constant at approximately 0.3 L/min.

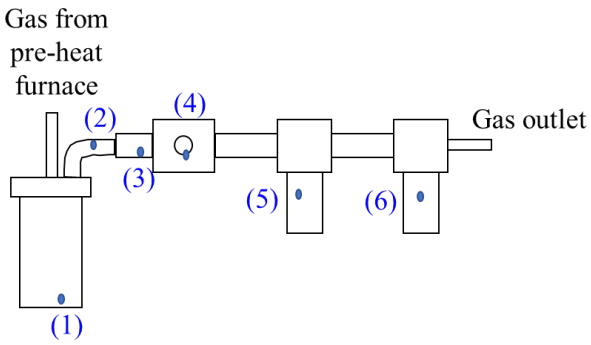

Figure 6.5: Schematic of the aerosol-LIBS systems showing the 6 different salt sampling locations for ICP-MS.

Table 6.1 provides a summary of the DU aerosol experiments conducted along with the date each test was performed. The first 5 experiments (MSU1 through MSU5) were run at 1 wt% UCl_3 in order to optimize the gate delay, to assess the observed U peaks, and to explore the effect of gas temperature and pressure. For the first three experiments, the gas pre-heat furnace was left off and the nebulizer pressure was varied at 12 psi, 20 psi, and 30 psi, respectively. The purpose of leaving the gas pre-heat furnace off was because the inlet temperature of the nebulizer was stable at 130°C with or without the pre-heat. In addition, because the gas flow rate was low, significant heat loss in the tubing between the pre-heat to the nebulizer was expected as well as substantial heat gain in the nebulizer tubing and jet. Following these pre-experimental runs, tests MSU4 through MSU9 were operated with the gas pre-heat furnace at 550°C with a 12 psi pressure differential across the nebulizer. In addition, the salt in these experiments contained 0.3, 1, 2, 3, and 5 wt% UCl_3 in LiCl-KCl.

6.2 Results and Discussions

6.2.1 DU Metal Spectra

Spectra obtained at 1, 5, and 16 μs gate delay from the DU metal sample are shown in Figure 6.6. The spectra show numerous U peaks between the 300 nm and 700 nm wavelengths. The peaks observed from 700 nm to 900 nm were from the Ar gas in the glovebox. The

Table 6.1: Summary of the UCl_3-LiCl-KCl experiments conducted.

Experiment number	wt% UCl_3	Date conducted
MSU1	1.0	July 23, 2016
MSU2	1.0	August 17, 2016
MSU3	1.0	August 24, 2016
MSU4	1.0	September 1, 2016
MSU5	1.0	September 30, 2016
MSU6	2.0	October 3, 2016
MSU7	3.0	October 5, 2016
MSU8	5.0	October 7, 2016
MSU9	0.3	October 8, 2016

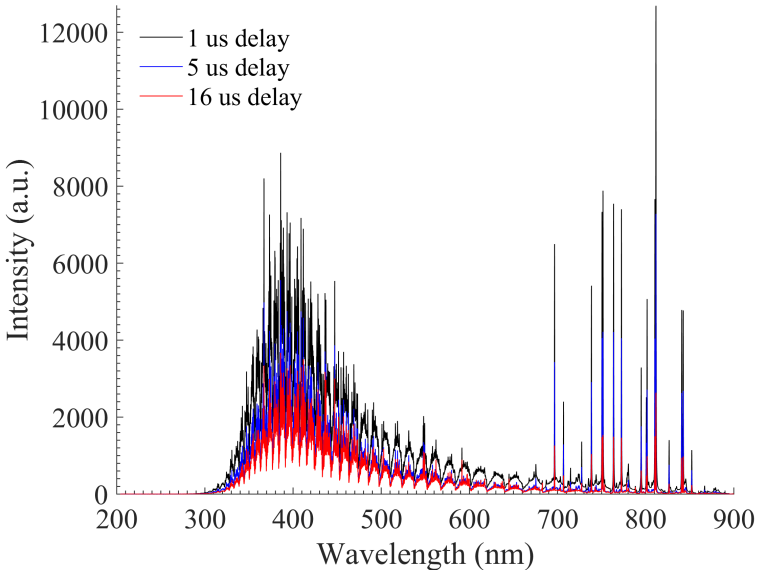

Figure 6.6: DU spectra generated at different gate delays.

spectrum obtained from the DU metal was compared to LIBS spectra obtained from Chinni et al.[18] for DU metal under argon gas. The two spectra were similar for wavelengths greater than 400 nm; however, below 400 nm the generated spectrum had significantly fewer lines and intensities. This issue was due to the fiber optic cable that had a poor optical transmission below 400 nm; thus, light in this spectral range had significantly reduced intensities. As a result, lower relative intensities for U lines in this region would be expected. Yet, dozens of spectral lines in the spectrum were compared to literature values in order to confirm results. The LIBS spectrum collected in this study agreed well with literature values.

Table 6.2: The SBR, SNR, and %RSD for the 385.96 nm spectral line from the DU metal sample.

Gate delay (μs)	SBR	SNR	%RSD
1	2.28	0.95	13.1%
5	2.59	1.31	8.1%
16	2.24	1.45	13.4%

The MATLAB GUI was used to determine the SBR, SNR, and the %RSD for the U 385.96 nm peak; these values are shown in Table 6.2. The SBR showed a maximum at 5 μs, though the magnitudes between the different SBR values were not significantly different. The SNR followed a different trend with the ratio increasing slightly as the gate delay increased. It appeared that the background was not strongly affected by the gate delay, though clearly the overall intensity was affected. With closer observation, the "background" observed in the spectrum decayed at nearly the same rate as the specific spectral lines, which was also noted by Chinni et al. [18]. There were a high density of U lines in the spectrum, due to Stark and Doppler broadening of the lines, the different peaks overlapped to create this apparent background. By using a spectrometer with high spectral resolution as was done by Barefield et al.[33], this broadening effect would be reduced, and less "background" and more spectral lines would be observed. As a result of the mid-range spectrometer used in this study, the SBR and SNR were not suitable for determining the optimal gate delay. In this case, the 1 μs gate delay was selected in order to maximize the signal intensity. This simple experiment, combined with the literature comparisons provided important insight to working with LIBS in a U sample.

6.2.2 Gas Temperature Effect

Following the DU metal study, UCl_3 salts were prepared and tested in the aerosol-LIBS system. After the MSU1 experiment, the salt in the nebulizer jar was purple-brown from oxide formation; however, salt collected everywhere else in the system was pure white suggesting low concentrations of UCl_3, as shown in Figure 6.7. This observation was confirmed using

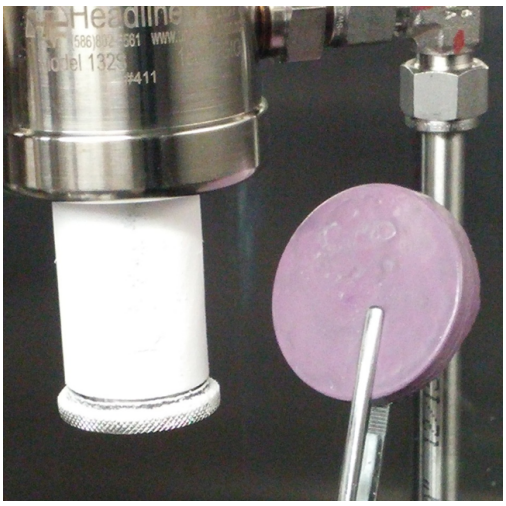

Figure 6.7: Photo showing the color difference between the bulk salt (purple) and 0.5 μm filter salt (white).

Table 6.3: ICP-MS results from MSU1 with 1 wt% UCl_3. Position locations shown in Figure 6.5.

Location in system	Location #	Concentration (wt% UCl_3)	Recovered mass(g)
Nebulizer jar	1	0.741	27.0625
Nebulizer spout	2	0.275	0.3487
Nozzle	3	0.287	0.0497
Sampling Chamber	4	0.108	0.0131
1.0 μm filter	5	0.077	0.7003
0.5 μm filter	6	0.062	1.6268

ICP-MS as shown in Table 6.3 and Figure 6.8. The UCl_3 concentration dropped drastically as the sampling location moved further from the nebulizer. This change in concentration throughout the system was also observed in the Ce experiments but to a lesser extent. This may be because the density of the UCl_3 salt aerosol is higher than that of $CeCl_3$; thus, a similar sized particle is more likely to fall from the slow aerosol gas stream. To test this postulation, MSU2 and MSU3 were operated at higher differential pressures and flow rates.

For MSU2, the pressure differential was maintained at 20 psi. Interestingly, the gas flow rate did not noticeably increase from the 10 psi case. For MSU3, the pressure differential was maintained at 30 psi. In this case, the gas flow rate increased to 0.6 L/min. The

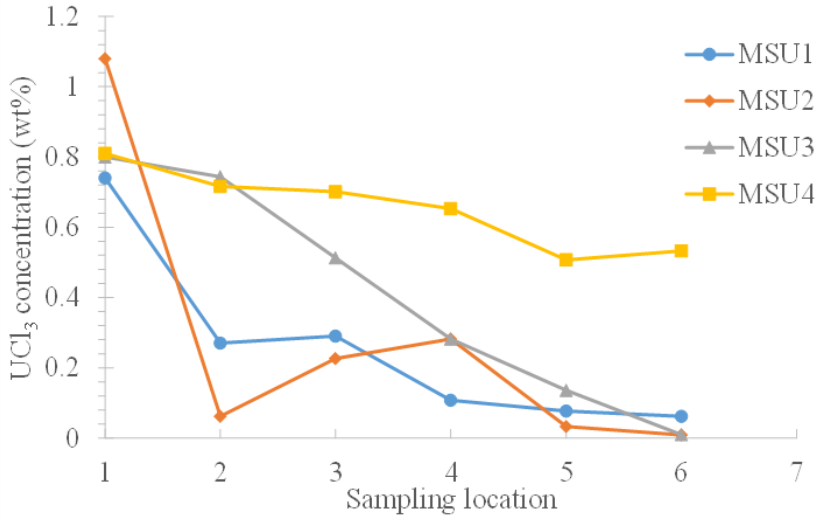

Figure 6.8: The concentration profiles of the system for the MSU1 through MSU4 experiments. Sampling locations are shown in Figure 6.5.

concentrations of UCl_3 at the different sampling locations are shown in Figure 6.8 indicating that the concentration profiles between MSU1 and MSU2 are different but have a similar trend. Though the pressures were different between these experiments, the gas flow rates were essentially the same. MSU3 has a different profile, indicating that the increased flow rate helps reduce the rate at which the UCl_3 falls from the aerosol gas stream. However, at the 0.5 μm filter, all three experiments had nearly the same low concentration.

Another significant observation between the first three U experiments is the overall stability of the aerosol-LIBS system. In the Ce experiments, the aerosol-LIBS system could be left operating for a number of hours (tested up to 14 hours) without significant change in the steady-state pressure and flow rate. During the testing of MSU1, nothing out of the ordinary was noticed with the stability of the system. However, with MSU2 the flow dropped to zero after two hours and with MSU3, the flow dropped to zero after 20 minutes. Presumably, the flow was reduced as a result of nebulizer tip clogging. This effect was never observed when the gas pre-heat was operating. Experiment MSU4 was run with identical conditions to MSU1 with an exception of the gas pre-heat being set at 550°C. The MSU4 concentration profile can be seen in Figure 6.8. Here, the profile does not drastically drop

to low values as was observed with the first three experiments. The MSU4 concentration profile is similar to the profiles observed in the Ce studies. In addition, the amount of oxide formation within the nebulizer was significantly reduced in MSU4. The mechanism creating the non-homogeneous concentration profile with cold carrier gas was not explored further because it remains outside the scope of the project; however, it may be the result of melt crystallization effects described for molten salt separations[43–47]. Future studies to explore the aerosol formation and characterization are recommended.

The above experiments showed that the actual temperature of the gas at the nebulizer inlet was not the same as the thermocouple reading at that point. That is, heat conduction through the thermocouple from the nebulizer body was controlling the measured temperature. Because of this, the actual temperature of the gas while using the gas pre-heat was unknown. Definitely, when the gas pre-heat furnace was operating, the gas temperature was high enough to prevent adverse effects and instabilities in the nebulizer. As a result, the remaining experiments were done using the gas pre-heat furnace set at 550°C.

The ICP-MS results for samples MSU5 through MSU9 are summarized in Table 6.4 showing the calculated concentrations of the sample based on the amount of UCl_3 that was added to the sample. There are some significant discrepancies between the calculated and measured concentrations. The differences may result from the salt sampling method and oxide formation. As noted above, a brownish oxide layer often formed on the top surface of the salt. If a significant portion of the oxide layer was sampled, the ICP-MS results would indicate higher resulting values than expected. A good example of this is the MSU5 bulk-melt measurement where the measured concentration was approximately 20% greater than the calculated. To prevent this, when sampling from the melt, the oxide layer was avoided in order to sample the clean salt below the layer. To better understand the actual composition, a portion of the salt was later crushed and sampled to provide a more even distribution of the salt and oxide layer. With this modification, the difference between the calculated and ICP-MS results were similar and in most cases, not significantly different.

Table 6.4: ICP-MS results from the U molten salt experiments, the calculated concentration is the expected value based on the amount of salts added.

Sampling location	MSU9 (wt% U)	MSU5 (wt% U)	MSU6 (wt% U)	MSU7 (wt% U)	MSU8 (wt% U)
Calculated	0.2015	0.6911	1.3823	2.0735	3.4557
Bulk-melt	0.0234	0.8817	1.2317	1.9763	3.0285
Bulk-crush	0.0423	0.6604	1.2474	1.9128	3.2353
Nebulizer spout	0.0613	0.4507	1.2615	1.6964	2.9352
Nozzle	0.0223	0.4537	1.0909	1.9165	2.9424
Sampling Chamber	0.0684	0.5015	1.3342	1.6411	2.6801
1.0 μm filter	0.0598	0.0603	0.4711	1.0061	2.8042
0.5 μm filter	0.0866	0.1290	0.9503	1.6569	2.7517

The one exception was the MSU9 experiment where only 20% of the calculated amount was being measured. However, this measurement value was similar for all of the other sampling locations for MSU9. With this experiment, there was some brown oxide residue left in a ring around the outside of the stainless steel crucible. Being that there was such a small amount of UCl_3 in the sample to start, this residue might account for the difference between the calculated and measured concentrations. Because the crushed ICP-MS measurements were the most consistent with observed and calculated results, they were used as the accepted true values for this study.

6.2.3 LIBS Measurements of UCl_3

The MSU1 through MSU4 experiments were analyzed using LIBS, but results were varied as a result of the non-homogeneous aerosol formation and transport. MSU4 was significantly more stable and data sets collected during this experiment were used for peak selection and gate delay optimization. The average spectrum generated from the 6 repetitions was normalized (using the mean of the entire spectrum) and compared to the normalized average spectrum of pure LiCl-KCl salt (MS6). Both tests were conducted at a 16 μs gate delay. This comparison highlighted differences in the spectra as shown in Figure 6.9. Using this approach, multiple U lines were identified and verified from the literature[18, 29, 33, 69].

Table 6.5: Observed U peaks in the UCl_3 salt samples.

Wavelength (nm)	Ionization State	Wavelength (nm)	Ionization State
357.70	I	394.28	II
358.09	I	400.52	I
358.45	I	401.77	II
359.37	I	406.25	II
360.63	II	409.01	II
365.92	I	417.16	II
367.01	II	435.57	I
374.64	II	436.21	I
381.19	I	437.20	I
381.41	II	439.39	I
385.46	II	457.68	I
385.96	II	502.74	I
386.52	II	562.08	I
387.10	I	607.73	I
387.85	I		

Table 6.5 shows some of the observed lines. The strongest U peaks identified were the U II 367.01 nm, U II 385.96 nm, and U I 387.10 nm lines. Interestingly, these peaks were within the region where poor transmission through the fiber optic cable was expected. With a different fiber optic cable, it was anticipated that even greater spectral responses could be achieved for these lines.

During MSU4, the gate delay was varied between 3 μs and 25 μs to determine the optimal value. Figure 6.10 shows the comparison between the different gate delay values. As would be expected, the overall intensity of the spectra decreases as the gate delay increases. However, it appears that there is significant background present at the shorter gate delay values. When the SBR's were calculated for these spectra, the trend was relatively flat which was consistent with the DU metal work. Figure 6.11 shows the intensity decay of several U lines with respect to a region with no U lines. From this comparison, it was apparent that the background was decaying at nearly the same rate as the peaks themselves. A similar response was observed for the DU metal case. As a result, the 3 μs gate delay was selected in this work as it had the strongest intensity overall. The actual optimal parameter may be

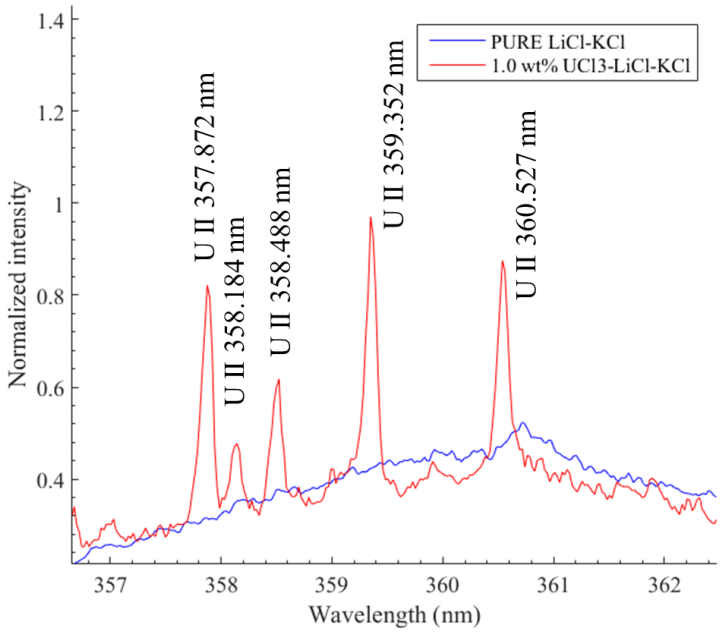

Figure 6.9: Comparison between the MSU4 spectrum and the MS6 spectrum generated using pure LiCl-KCl salt.

at a shorter gate delay than studied here.

Figure 6.12 shows the entire spectrum generated for the 1 wt% UCl_3 (MSU4) experiment at a 3 μs gate delay. The spectrum was dominated by the Li, K, and Ar lines as observed before with both the aqueous and Ce work. In the close up region, a cyclic pattern in the apparent background was observed. This was a result of transmission efficiencies of the echelle grating. The intensity of the U peaks was quite small compared to the apparent background and the Li, K, and Ar peaks. Definitely, increasing the spectral resolution would help with the apparent background. Results show that as the resolution increases, less light is available and the overall intensity may decrease. Another approach to increase the intensity in the U line regions would be to change out the fiber optic cable used. Whereas this change would increase the intensity, it was not tested due to challenges of resealing the glovebox with an additional fiber optic cable.

To explore the analytical precision of the U aerosol results, the %RSD values between the 6 spectra measured per experiment were calculated. The average %RSD values in the range from 350 nm to 800 nm were between 2.5% and 8% for the un-normalized spectra. MSU8 (5

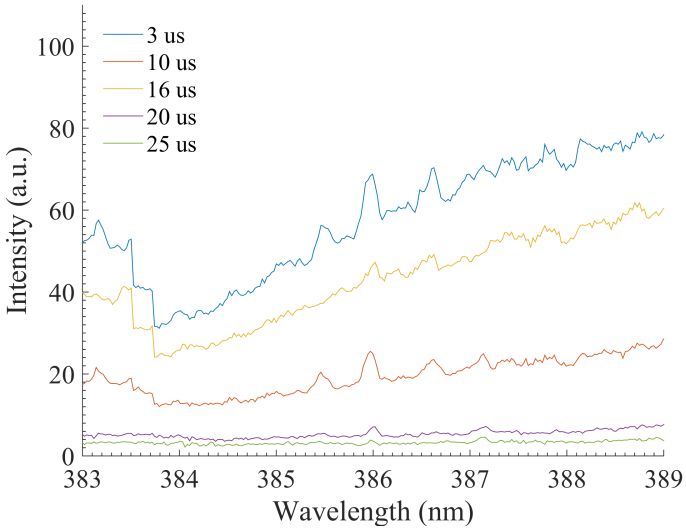

Figure 6.10: Comparison between the spectra as a function of the gate delay.

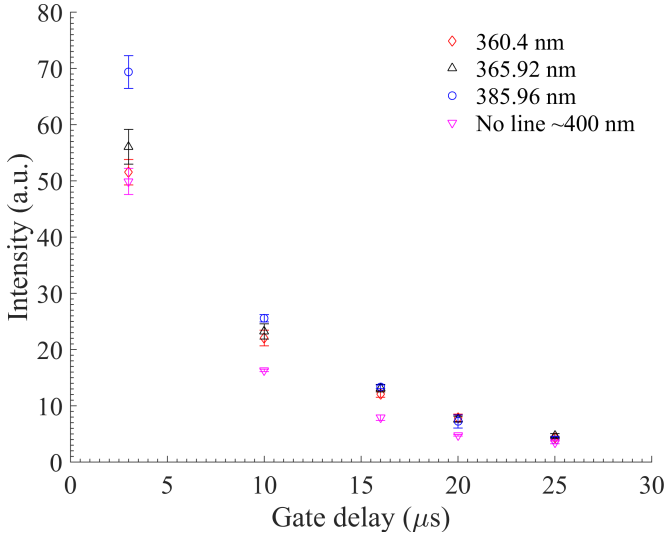

Figure 6.11: Comparison between the spectra as a function of the gate delay.

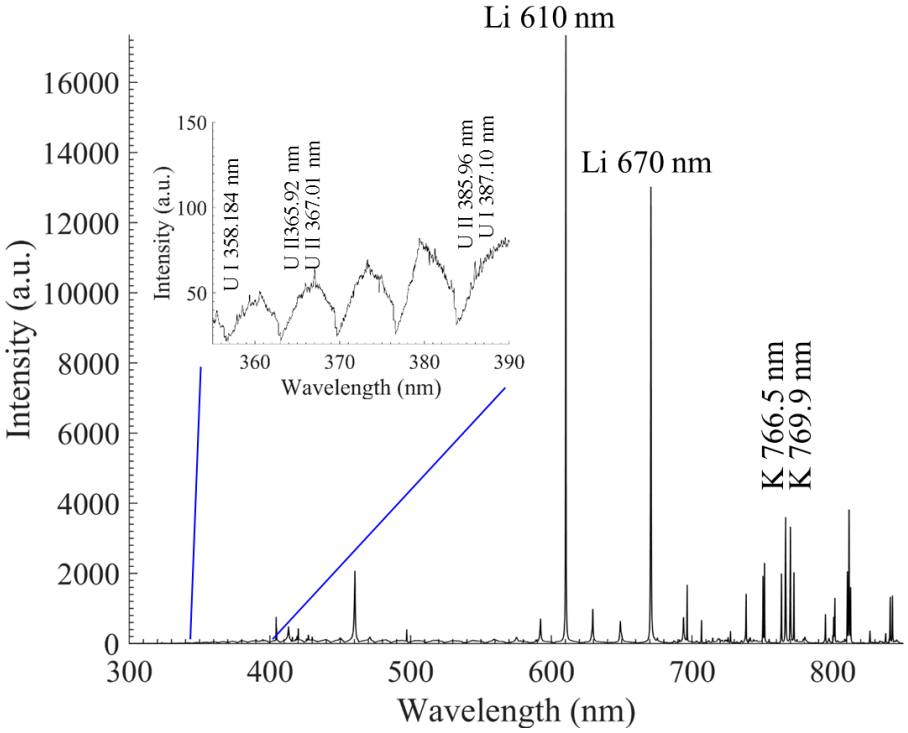

Figure 6.12: Typical spectrum obtained for UCl_3 in molten salt aerosol at 3 μs gate delay.

wt% UCl_3) and MSU9 (0.3 wt% UCl_3) had the best and worst %RSD values, respectively. These extreme cases are shown in Figure 6.13.

Figure 6.14(a) shows the %RSD between the mean spectra from MSU5 through MSU9. The %RSD averaged approximately 25% between 550 nm to 800 nm indicating an improvement over the Ce study. However, by normalizing each spectrum with respect to the average intensity of the Li 610.3 nm peak, the %RSD between the different experiments dropped to around 10 to 15% (see Figure 6.14(b)). The high variation in the spectra between 350 nm and 450 nm was a result of the varying U concentrations between experiments. The MATLAB GUI was used to calculate the spectral response for the normalized 367.01 nm, 385.96 nm, and the 387.10 nm lines. Table 6.6 gives a list of the %RSD values for the selected U peaks. Between the three spectral lines explored, the %RSD does not vary significantly; however, it does vary from experiment to experiment. The limiting factor for the precision in this study was the fluctuation in laser energy, particle interaction with the laser light,

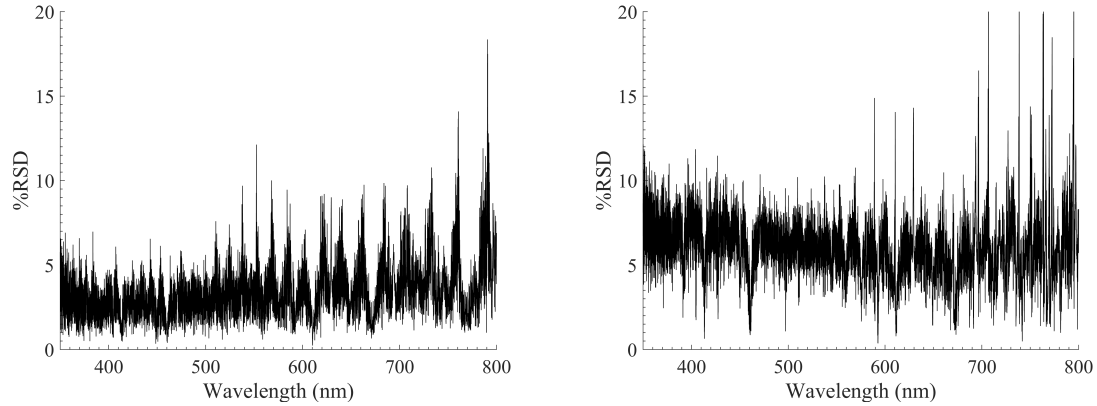

Figure 6.13: (a) %RSD for the 5 wt% UCl_3 (MSU8) case and (b) the %RSD for the 0.3 wt% UCl_3 (MSU9) case.

Table 6.6: %RSD values for the peak intensities for select peaks between the 6 repetitions.

	U 367.01 nm	U 385.96 nm	U 387.10 nm
MSU9	7.3	7.2	7.7
MSU5	5.2	4.5	4.7
MSU6	3.2	3.5	2.6
MSU7	2.5	2.7	3.1
MSU8	2.3	2.2	2.7

and damage to the sapphire windows over time. On average, the %RSD for the different experiments and lines was 4.5%, which was similar to the value obtained for the Ce study.

Univariate Calibration Curves

To further assess the aerosol-LIBS system, univariate calibration curves were generated using the peak areas and intensities for the 367.01 nm, 385.96 nm, and 387.10 nm lines. The calibration curves for these lines are shown in Figures 6.15, 6.16, and 6.17, respectively. Table 6.7 summarizes the R^2 values, regression coefficients, and LOD for the different lines. The spectral responses for the different U lines with respect to the concentration were linear but there were significant differences between the peak area and peak intensity curves. The curves generated using the peak areas have better R^2 values and visually appear more linear.

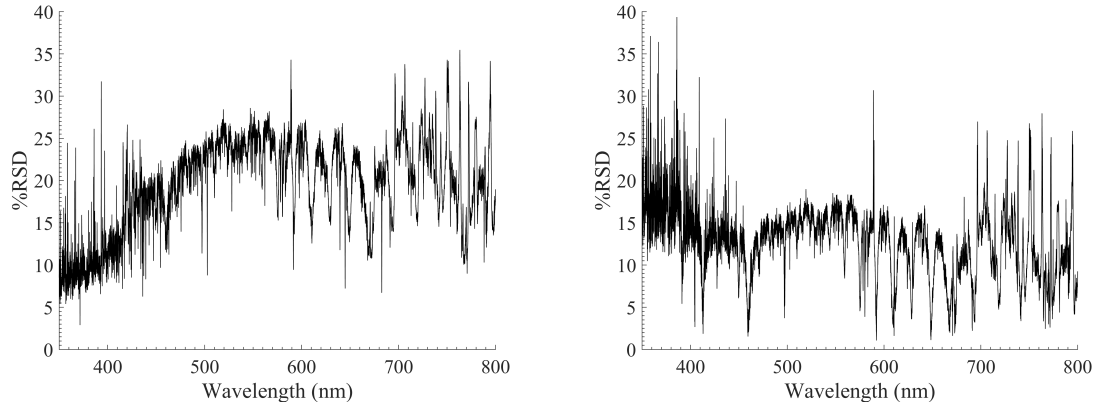

Figure 6.14: %RSD for the U spectra over time (MSU5-MSU9) (a) without normalization and (b) with normalization.

Table 6.7: Regression coefficients and LOD for the univariate calibration curves for U in molten salt.

Peak Area	R^2	$S_{y/x}$	b_1	b_0	LOD (wt%)	LOD (ppm)
367.01 nm	0.9917	0.0322	0.2488	-0.01504	0.0647	647
385.96 nm	0.9938	0.0319	0.2857	0.01772	0.1215	1215
387.10 nm	0.9732	0.0264	0.1122	-0.00857	0.1923	1923
Peak Intensity						
367.01 nm	0.9698	0.6025	2.408	4.329	0.4286	4286
385.96 nm	0.9655	0.7777	2.899	4.728	0.3906	3906
387.10 nm	0.9061	0.7707	1.687	4.972	0.7508	7508

In addition, the LOD values were much lower for the peak area cases. One reason for this was because the background was subtracted for the peak area cases; thus, the change with respect to the concentration (sensitivity) was more apparent. From the LOD alone, the peak intensity curves would not be recommended for analytical analysis. For the peak area curves, the U 367.01 nm line had the best LOD of 647 ppm. The U 385.96 nm line had a higher LOD at 1132 ppm despite having a steeper slope. This was because the 385.96 nm line had a large standard deviation for the MSU9 experiment. As a result, it appeared that the U 367.01 nm line would provide the best analytical results.

To assess the accuracy of the calibration curves, a the LOOCV analysis was done. The challenge with this was that there were only five data points to start with, performing a

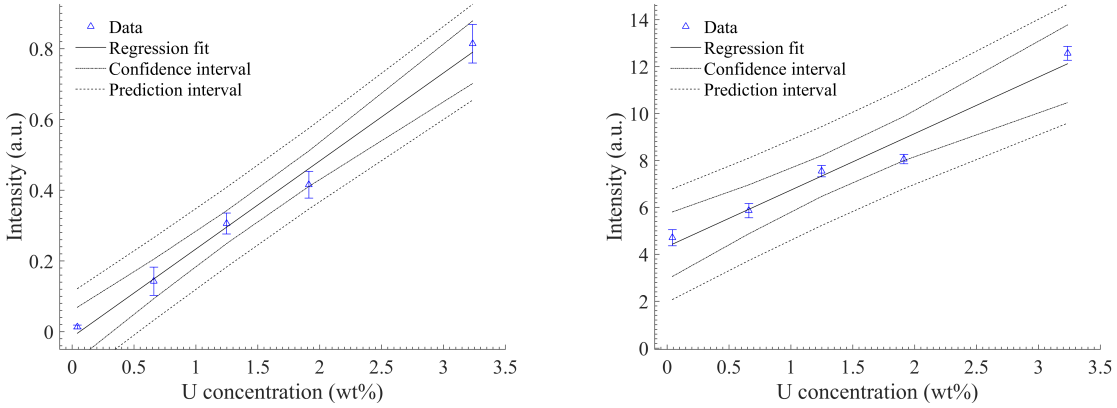

Figure 6.15: Calibration curves for the molten salt U experiments using (a) peak areas and (b) peak intensities for the U 367.01 nm line.

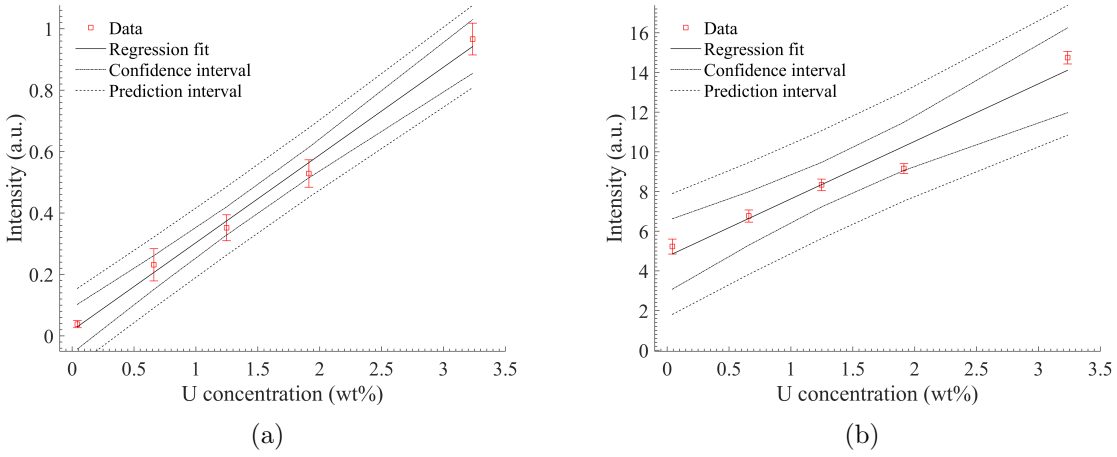

Figure 6.16: Calibration curves for the molten salt U experiments using (a) peak areas and (b) peak intensities for the U 385.96 nm line.

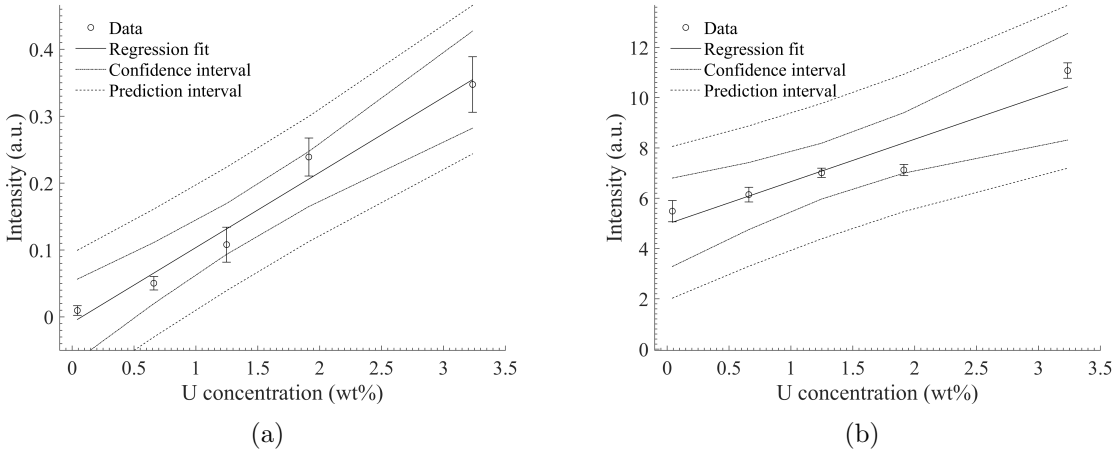

Figure 6.17: Calibration curves for the molten salt U experiments using (a) peak areas and (b) peak intensities for the U 387.10 nm line.

LOOCV analysis would leave only four active points which could affect the overall response. The effect of leaving one sample out on the linear regression was explored and indeed the slope and y-intercepts varied as one of the samples was left out. However, the resulting four point regression curve fits into the confidence intervals of the five point regression line as shown in Figure 6.18. The largest variation in the study came from leaving out the first point (MSU9) and the last point (MSU8). The RMSECV and % errors calculated from the LOOCV analysis are shown in Table 6.8. Results indicate that the % error values for the MSU9 samples are poor; however, this is as expected because the concentration (0.0423 wt% U) is lower than the calculated LOD. Indeed, the spectral response at this concentration yielded no apparent uranium lines and this experiment was basically a blank sample from the aerosol-LIBS analysis standpoint. The % errors for the other samples left out vary in magnitude, with the best results being generated for the mid-range concentrations. Here, the U 367.01 nm line gave the best % error of 4.2%. However, in the upper concentration range the 385.96 nm line provided greater accuracy. Between the LOD and the accuracy FOM, the U 367.01 nm line performed best and was the recommended univariate calibration curve for future analysis. This line had a RMSECV of 0.229 wt% U. This study demonstrated

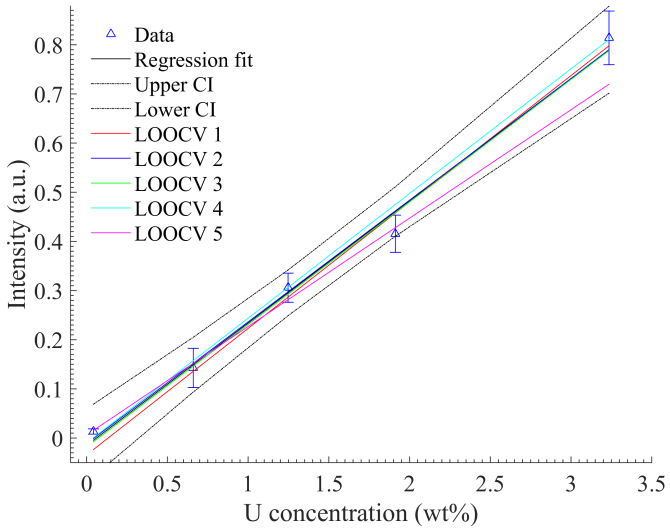

Figure 6.18: Representative response in the regression fits for the LOOCV analysis. Data generated for the U 367.01 nm line using peak area.

Table 6.8: % Error between the predicted concentration and the ICP-MS concentration for the LOOCV analysis.

Peak Area						
Peak (nm)	MSU9	MSU5	MSU6	MSU7	MSU8	RMSECV (wt%)
367.01	336	5.8	4.2	12.3	13.2	0.229
385.96	140	18	7.8	8.4	11.5	0.196
387.10	548	29	21	20	7.3	0.275
Peak Intensity						
367.01	531	5.1	8.8	24	28	0.476
385.96	591	8.8	0.4	25	36	0.577
387.10	1132	7.1	3.8	41	84	1.293

that measurements of U in molten salt could be made with reasonable accuracy for samples containing at least 1 wt% UCl_3. The true limit to how low the aerosol-LIBS system could accurately quantify U in molten salts was likely lower than 1 wt% UCl_3; however, without additional data points in this region, the exact measurement limit was unknown.

One limitation to the calibration curves reported was the limited number of data points available. With more data points (at least 6), better analytical results could be obtained. The error estimation and the confidence intervals depended on the number of data points used in the analysis. With more points, the uncertainty estimation decreased and variations

within the experimental setup would more likely to be accounted for. Additional points would also reduce variation in the LOOCV and better cross validation results would be achievable. In addition, more experiments in the lower concentration range would provide a better estimate on the measurement limit of the aerosol-LIBS system.

PLS Model

The U experiments were analyzed using the PLS_toolbox in MATLAB. Because there were few data points, and only 6 repetitions per experiment were done (30 spectra total), the data was not divided into calibration and validation sets. One of the MSU9 repetitions had an unusually high Q residual with respect to the Hotelling value (generalization of Students t distribution) and was left out of the calibration. As a result, 29 data points were used in the PLS analysis. Figure 6.19 shows the LV with respect to the RMSECV for the generated model. In this model, 6 LV were selected which yields a RMSECV of 0.111 wt% U or 1110 ppm. Figure 6.20 shows the PLS calibration curve. The spectral response is linear with some variation between the sample repetitions.

Being that no validation data set was used, the accuracy of the model was verified using an additional cross validation approach within the PLS_toolbox. To be consistent with the univariate approach, a LOOCV method was used. Here, the RMSECV was calculated to be 0.0850 wt% or 850 ppm U, which is slightly lower than the venetian blind approach. This was expected because with the LOOCV, 100% of the samples were left out and uncertainty was reduced. The average results of the LOOCV tests are listed in Table 6.9. For the MSU9 experiment, the % error is 105%, which is too high to be useful for analytical measurements. However, being that the MSU9 concentration was lower than the calculated LOD and no U response was measured in the spectra, this result is not unexpected. The % errors for the other U concentrations are within the acceptable range for analytical measurements.

Between the univariate and PLS calibration approaches, the PLS model had a significantly better RMSECV (0.085 wt% vs. 0.229 wt%). One reason for this was that the

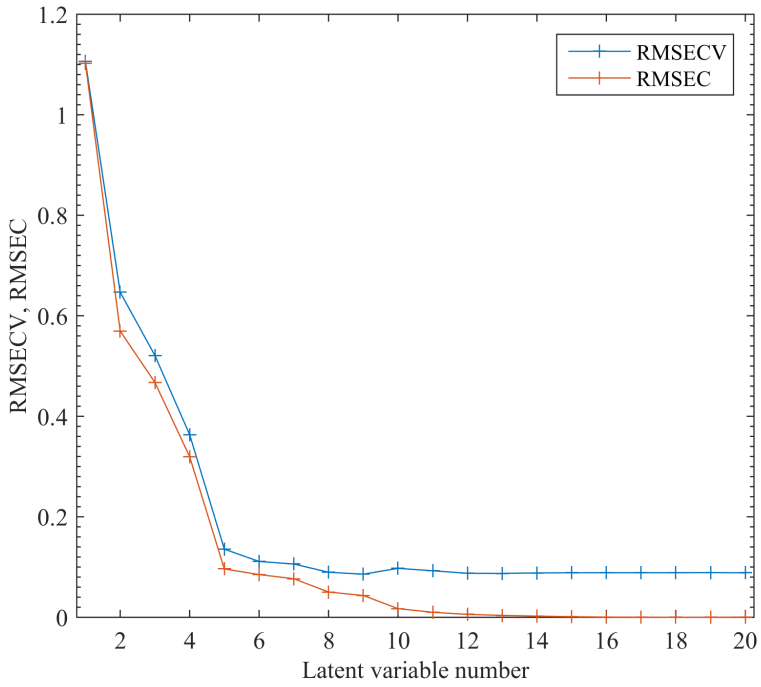

Figure 6.19: The RMSECV with respect to the number of LV used in the PLS model.

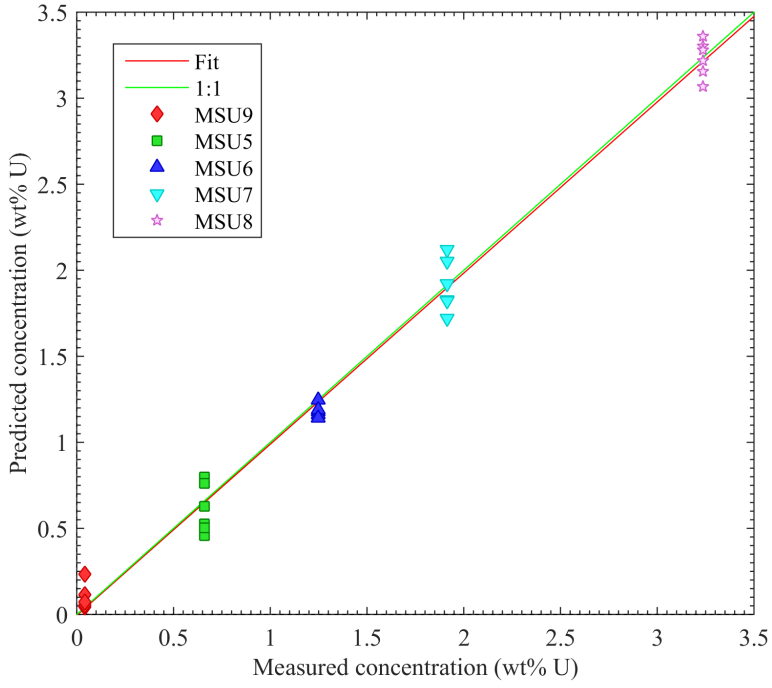

Figure 6.20: PLS calibration curve generated from the measured LIBS spectra.

Table 6.9: % Error between the predicted concentration and the ICP-MS concentration for the PLS leave-one-sample-out analysis.

Experiment	% error
MSU9	105%
MSU5	12.3%
MSU6	5.3%
MSU7	4.1%
MSU8	2.3%

spectral response for U in these experiments was very small. When looking at individual peaks (univariate), the variation due to the %RSD between the spectra combined with the weak signal created high variation and lower correlation between the measured response and the concentration. On the other hand, the PLS model used the entire spectrum, and LV that best describe the response were selected for the modeling. As a result, the PLS model performed significantly better and was recommended for future analytical measurements of UCl_3 in molten salts.

6.2.4 Aerosol-LIBS System Assessment

Uranium results obtained from the aerosol-LIBS system in molten salts were compared to other U studies found in the literature. The LOD was the most widely reported FOM and was used for the comparison. Singh et al.[27] found the LOD for U in liquid aerosol to be 1359 ppm. Also in liquids, Wachter and Cremers[19] determined the LOD to be approximately 100 ppm. On a substrate, Sarkar and co-workers[25] found the LOD of U to be 18 ppm. Finally, Chinni et al.[18] found the LOD of U in soils to be 0.26 wt% at close range and 0.5 wt% at a distance of 30 m. From these studies, it can be seen that results vary for the LOD of U in different materials and methods. The LOD determined using the aerosol-LIBS system was 647 ppm, which was located within the mid-range of values reported in the literature. To date, the 647 ppm LOD was the only reported LOD for U in a molten salt.

Typical concentrations of different components within the ER have been reported by Phongikaroon and Simpson[6] and Bean[92]. Table 6.10 shows the compositions of the ER

Table 6.10: Composition of ER salt[6].

Composition (wt%)			
LiCl (21.22)	$SrCl_2$ (1.25)	$NdCl_3$ (5.14)	$PuCl_3$ (5.09)
KCl (26.99)	UCl_3 (2.81)	$PmCl_3$ (0.07)	$AmCl_3$ (0.02)
NaCl (23.77)	$BaCl_2$ (1.67)	$SmCl_3$ (0.99)	$PrCl_3$ (1.51)
RbCl (0.44)	$LaCl_3$ (1.60)	$EuCl_3$ (0.07)	YCl_3 (0.92)
CsCl (3.20)	$CeCl_3$ (3.04)	$GdCl_3$ (0.04)	$NpCl_3$ (0.14)

salt following electrorefining (the amount of UNF reprocessed up to this point was not reported). The salt compositions reported by Bean were for a small batch process in which 269.45 g of UNF was electrorefined in 790 g of 9 wt% UCl_3-LiCl-KCl salt. Following electrorefining, 817 ppm of U-235, 18,030 ppm (1.8 wt%) U-238, 876 ppm Pu-239, and 199 ppm Pu-240 were contained in the salt. In both reported studies, greater than 1 wt% UCl_3 was present in the salt which was well above the calculated LOD and within the range of aerosol-LIBS system's capability to provide good analytical measurements. This indicates that monitoring U in the ER would be feasible via this method. Definitely, additional work should be done to explore multi-component salts with complex spectra to further assess the capability of the approach.

6.3 Summary and Conclusions

With the successful testing of the aerosol-LIBS system using $CeCl_3$ in Phase III (delivered in Chapter 5), salt samples containing UCl_3 were analyzed in this phase of the work. The main system design had not been modified; however, the optics were cleaned and adjusted and several procedural changes were made in the transition to U. When working with U, the system components could not be removed from the glovebox and washed as was done previously with the Ce experiments. Thus, cleaning was done using extensive scraping and material removal via parafilm. In addition, new 1.0 μm filters were used in every experiment to prevent changes in the steady-state pressure drop across the system.

The first three U experiments were run to explore the effect of the gas pre-heat temper-

ature with respect to the gas pressure and flow rate. Results indicated that without the gas pre-heat at 550°C, the U concentration within the system components decreased as the distance from the nebulizer increased. This effect was controlled by adjusting the gas flow rate. Concentration profiles with the gas pre-heat were similar to those obtained for the Ce cases.

The %RSD values for the different U experiments were on an average of 4.5%. Considering the optical degradation of the sapphire windows overtime and the large laser energy fluctuation, this %RSD result was reasonable. From the univariate calibration curves, the U 367.01 nm line using the peak areas yielded the best results with a RMSECV of 0.229 wt% and a LOD of 647 ppm U. The PLS model performed significantly better than the univariate case with a RMSECV of 0.085 wt%. This is a result of using more LV to model the analytical response with respect to the concentration. Results from both the univariate and PLS model showed that samples containing at least 1 wt% UCl_3 could be measured with reasonable accuracy.

From the typical ER salt compositions reported, the aerosol-LIBS system should be capable of detecting, monitoring, and quantifying U within the salt at near real-time. The successful competition of this phase strongly supported the aerosol-LIBS approach as a viable method for measuring the electrorefiner salt used during pyroprocessing of used nuclear fuel.

Chapter 7

Summary and Recommendations

7.1 Summary

7.1.1 Purpose, Motivation, and Background

- Nuclear power is an essential component in the United States energy portfolio because it is capable of meeting the nation's growing demand for energy in a safe, environmentally friendly manner. Currently in the United States, a once through fuel cycle is used. With this, the UNF is to be stored in a geological repository. This approach is wasteful since 95% of the material is useful U. By recycling the UNF, the waste can be reduced substantially while ensuring a more sustainable nuclear future. The PUREX process is used worldwide to recycle UNF; however, this process is not proliferation resistant and is not fully compatible with metallic fuel recycle.

- Pyroprocessing has been proposed as an attractive and proliferation resistant alternative to traditional UNF recycling (PUREX process). In this process, U is electrochemically dissolved at the anode, transported through a molten salt electrolyte, and deposited on a cathode. The U product is then scraped from the cathode for reuse. As part of this process, fission products, rare earth, and actinides accumulate in the salt. This presents material accountability and safeguards concerns. Currently, material tracking of special nuclear materials in pyroprocessing is done using ICP-MS; whereas this process yields good analytical measurements, it is time consuming and real-time

measurements are not possible.

- LIBS is an analytical approach that has the potential to monitor special nuclear materials in pyroprocessing in near real-time. In LIBS, a laser pulse is used to create a plasma on the surface of a material, as the plasma cools, elements return to ground states with the emission of light. Each element emits light at characteristic wavelengths. When the light from the plasma is collected, the resulting spectra can yield qualitative and quantitative information about the composition of the sample. LIBS is an attractive approach for pyroprocessing safeguards because it can be done in near real-time with little to no sample preparation, and quantitative results can be obtained.

- The purpose of this dissertation was to explore and assess a LIBS analytical technique to monitor special nuclear materials used in pyroprocessing of UNF. The focus was on the development of an aerosol-LIBS system which was tested using an aqueous media, molten $CeCl_3$-LiCl-KCl salt, and UCl_3-LiCl-KCl salt. Success of this work will advance the material accountability and safeguards of pyroprocessing of UNF.

7.1.2 Literature Review

- LIBS has been used to accurately measure actinides in a number of different materials and phases. Many researchers and scientists have explored U directly in liquids, including aerosols and found the LOD to be between 100 ppm and 1,359 ppm. In addition, many studies have done a liquid drying approach to measure U concentrations on substrates. A substantial amount of work has been done to measure oxide fuels (U, Pu, Am, and Np fuels) for quality control purposes. In many cases, a high resolution spectrometer was used to better understand the complex spectra that results from the heavy elements.

- Only a handful of LIBS studies have been conducted in a molten salt to date. Of these, Cr, Co, Mn, Ce, Eu, Pr, U, Pu, and Np were studied. These cases show the strong

potential for LIBS in molten salts; however, all of these studies were conducted using a static surface configuration which can lead to homogeneity and splashing concerns.

- Several LIBS studies have been conducted using a solid LiCl-KCl salt to measure Ce, Gd, and U. While these studies show good analytical results, a major concern was the non-homogeneous nature of the solid salt due to fractional crystallization.

- There are multiple approaches for LIBS analysis in liquids, these are:

    1. Static liquid configuration–the laser light is directed downwards onto the top surface of the liquid to create the plasma. Whereas this was the simplest approach to implement, it was limited by surface perturbations, bubble formation, surface layers, and splashing.

    2. Sub-surface bulk measurements–the laser pulse is focused at a point below the surface of the liquid to create the plasma, Often, a double pulse system was used to enhance signal. The main drawback of this approach was that a transparent liquid is required.

    3. Liquid jet approach–the laser pulse is focused onto the surface of a liquid jet. This mitigated many of the challenges associated with surface perturbations and splashing. The main drawback to this approach from a molten salt perspective was system clogging.

    4. Aerosol configuration–the laser pulse is focused into a liquid aerosol gas stream. The drawback to this approach was particle interaction with the laser pulse. The main advantage was reduced splashing, increased laser utilization, and better homogeneity of the sampling.

- Based on findings from the literature and an assessment of the different liquid configurations, it appeared that the aerosol approach would provide the best analytical results due to increased sample homogeneity and reduced splashing.

7.1.3 Equipment and Methodology

Equipment

- The laser used in this study was a Nd:YAG laser (Quantel USA) that was operated at 532 nm. Here, the laser energy fluctuated ±10%. Light was directed into the aerosol gas stream via laser mirrors and focal lenses. Light from the plasma was collected via a fiber optic cable (Ocean Optics). This cable had poor light transmittance between 280 nm and 450 nm. Above this wavelength range, the transmittance was 75%. The spectrometer used was a Mechelle 5000 echelle type spectrometer with an iStar 334T ICCD detector. The spectral resolution was 4,000 for this spectrometer.

- Experiments were conducted in an inert atmosphere glovebox (Innovative Technology). The O_2 and H_2O levels were monitored and controlled down to 0.1 ppm. A custom quartz port was installed into the glovebox wall allowing for easy laser transport into the glovebox. In addition, laser blackout curtains were installed to adhere to laser safety standards.

- ICP-MS analysis was conducted using a 7900 instrument from Agilent Technologies.

Methodology

- To assess the performance of an analytical method, standard FOM were used to evaluate the precision, accuracy, and LOD of the approach. To assess these metrics, appropriate peak selection, normalization, and calibration curves were developed.

- Typically, multiple peaks for a given element were present in the spectrum and it was important to select peaks that had the greatest sensitivity and lowest interferences for spectral analysis. The methods used in this work to assess the strength of a peak were the SBR and the SNR. Peak selection and optimization of parameters were done with respect to the SBR.

- The analytical precision measurement in this work was the %RSD between the repetitions acquired per sample. The %RSD was applied in two general ways: (1) to the entire spectrum to gain a general trend for the overall repeatability of the measurement and (2) to individual peaks to gain insight to the repeatability of the analytical response using that line.

- Normalization of the spectra was accomplished using an internal standard. In this case, each entire spectrum was normalized using one of the peaks from the internal standard.

- Calibration curves showed the spectral response of the analytical system with respect to the sample composition. Using this curve, the concentrations of unknown samples were determined. Two methods for generating calibration curves were:

    1. Univariate calibration: In this approach, the spectral response from a single variable (one spectral peak) was compared to the concentration. The slope of the line indicated the sensitivity of the spectral response to the change in concentration. Using linear regression, the slope, y-intercept, and coefficient of determination were calculated. The uncertainty of the regression line was determined using the standard deviation in the y direction and was shown using confidence intervals. From the calibration curve slope and the blank sample standard deviation, the LOD was calculated. This represented the limiting concentration that could be detected with 33% confidence.

    2. Multivariate calibration: A chemometric approach via PLS was used to determine the best variables (LV) to model the analytical response with respect to the concentration. Rather than using one spectral peak, the entire spectrum was used which resulted in a more robust calibration curve. The advantage of this calibration approach had been shown for complex spectral and multi-elemental analysis. In this work, the commercial software PLS_toolbox was used in the MATLAB

environment.

- To assess the performance of the calibration curves and to estimate the expected error of the measurement, cross validation and blind testing were performed. Two cross validation approaches were used, venetian blinds and LOOCV. The cross validation was performed using the actual calibration data set by leaving one or multiple points out and analyzing them as unknowns. The metric used to assess the cross validation was the RMSECV. Lower values of the RMSECV indicated lower estimated errors. Validation of the curve was done using additional data points not used in the calibration. This is often done using unknown samples. In this work, unknown samples were not always available so the spectral repetitions were divided into calibration and validation sets for the PLS analysis. The methods to assess the validation were the RMSEP and the % error. Lower values showed better curve performance.

7.1.4 Aerosol-LIBS System Design and Aqueous Testing

Aerosol-LIBS System Design

The basic aerosol-LIBS concept consisted of: (1) the carrier gas pre-heat prior to the nebulizer, (2) molten salt nebulization using a Collison nebulizer, (3) LIBS testing through a sampling chamber, (4) aerosol removal, and (5) cooling prior to releasing the carrier gas to the exhaust system. Each of this system stages could be summarized as follows:

1. Gas pre-heat: Argon gas was used as the carrier gas and the gas flow was monitored using a Key Instruments flow meter. The heating requirement for the gas was evaluated and a 1,350 W Kerr Lab furnace was selected as the heating source. A heating coil was handmade from 6.3 mm diameter stainless steel tubing. This coil was 7 cm in diameter and 14 cm tall and contained 4.3 m of tube length. The pressure drop at the assumed 20 L/min flow was 11.5 psi.

2. Nebulizer: The Collison nebulizer was selected for molten salt aerosol generation because of the strong stainless steel construction which made it more temperature and corrosion resistant. In addition, the liquid material was not forced through the jet which made this nebulizer more clog resistant. High temperature (500°C) sealing methods were explored and a Swagelok fitting, graphite cord, and Deacon 770-L thread sealant were identified as feasible methods to seal the nebulizer stem, jar, and tip, respectively.

3. LIBS sampling: Here, a laser mounting mechanism, optics, and sampling chamber were designed. The Nd:YAG laser was mounted to the outside of the glovebox as well as a breadboard being mounted on the inside wall. Laser light was directed into the aerosol stream via a sampling chamber. The sampling chamber was designed of solid stainless steel with ports drilled for aerosol introduction and removal, light delivery, light collection, pressure, and temperature measurements. Sight windows from Rayotek were used to isolate the aerosol stream from the optics.

4. Aerosol removal: A stainless steel filter (United Filtration Inc.) was identified as a coalesce filter. Here, a 1.0 μm filter was selected. High temperature flexatalic seals were purchased, allowing the system to operate at high temperatures.

5. Gas cooling: To cool the carrier gas to room temp prior to the exhaust system, a miniature tube in tube heat exchanger from Exergy was identified. In this case, the cold side of the heat exchanger would be water at 35°C.

Aqueous Aerosol Testing

Materials and Methods

- Aqueous samples were prepared using deionized water with additives of Ce, Gd, and Nd. A total of 36 samples were made–varying the Ce and Gd concentrations from 100 ppm to 10,000 ppm. The Nd concentration was left constant at 1,000 ppm. To explore sample matrix effects and interferences, three concentrations sets were explored, each

containing Low, Mid, and High concentrations of the other element. For each sample, ten repetitions were collected, each comprising of 200 laser pulses.

- The laser energy, gate delay, and gate width were 55±5mJ, 6 μs, and 20 μs, respectively.

Results and Discussions

- The aerosol size distribution was measured using a SMPS system. The resulting size distribution was bimodal, where the lower distribution had a CMD of 1.4 μm with a GSD of 1.2 and the upper distribution had a CMD of 4.2 μm with a GSD of 1.0.

- Spectral normalization was done using the H 656.3 nm line and three peaks for Ce and three peaks for Gd were identified for the analysis. These lines are: 418.660 nm, 428.999 nm, and 457.228 nm for Ce and 374.347 nm, 404.986 nm, and 409.861 nm for Gd.

- The %RSD between the repetitions of the measurements averaged 4.4% for the Ce 418.660 nm line and 3.8% for the Gd 409.861 nm line. The greatest sources of the variation were from the laser energy fluctuation and particle interaction with the laser pulse. This interaction was observed visually as point source flashes in the laser path within the sampling chamber.

- Univariate calibration curves for the different Ce lines were made using the peak areas and peak intensities. Between the different curves, the Ce 418.660 nm curve generated using the peak intensity showed the least variation as a function of the Gd concentration. As a result, all 36 samples were combined to form a single calibration curve with an R^2 value of 0.994 and a LOD of 189 ppm. The cross validation using a LOOCV method yielded an RMSECV of 390 ppm. Validation using two blind samples was done and the RMSEP was calculated to be 503 ppm.

- For Gd, univariate calibration curves were also generated. In this case, the Gd 409.861 nm curve using the peak area showed the least variation between the Low, Mid, and

High Ce concentrations. As a result, a single calibration curve using all 36 samples was made. This curve had an R^2 value of 0.992 and a LOD of 316 ppm. Cross validation using a LOOCV method yielded an RMSECV of 421 ppm. A validation using two blind samples was done and the RMSEP was calculated to be 645 ppm.

- In addition to the univariate curves, PLS calibration curves were generated using the PLS_toolbox software. Here, the ten repetitions were divided and then averaged to provide 36 samples for the calibration and the other half of the repetitions being averaged for the validation set. The Ce model had 7 LV which led to a RMSECV of 406 ppm. The validation set yielded a RMSEP of 519 ppm. For Gd, 7 LV were also used and the RMSECV was 417 ppm and the RMSEP was 536 ppm.

- For both the univariate and multivariate approaches, the % errors for the 100 ppm case were high (this was as expected because it lied below the LOD). The other concentrations ranges had reasonable % errors from the cross validation and unknown samples.

- Table 7.1 shows a summary of the aqueous aerosol-LIBS results for Ce and Gd. The difference between the univariate and multivariate models were not distinctively noticeable for this work.

- The aqueous work has demonstrated the effectiveness and feasibility of the aerosol-LIBS system design for analytical measurements at room temperature.

7.1.5 Molten Salt System Design and Testing with $CeCl_3$

Molten Salt Experimental Design & Shakedown

- To reduce the number of particles interacting with the incoming laser light, the sampling chamber was redesigned so that the plasma formation occurred at the top of

Table 7.1: Summary of the aqueous aerosol-LIBS results.

	Ce	Gd
%RSD	4.4%	3.8%
Univariate		
b_1	3.16E-05	4.66E-06
b_0	0.0313	2.38E-04
R^2	0.994	0.992
LOD (ppm)	189	316
RMSECV (ppm)	390	421
RMSEP (ppm)	503	645
Multivariate		
LV	7	7
RMSECV (ppm)	406	417
RMSEP (ppm)	519	536

the aerosol gas stream. The sight windows into the sampling chamber were 3/8 NPT quartz windows (Rayotek Inc.) with a 6 mm diameter aperture.

- Heating and insulation of the system were designed. Two Kerr Lab furnaces were used: one to heat the gas prior to the nebulizer and the other to heat and melt the salt within the nebulizer. A heating tape was used (initially) to heat the length of tubing from the gas pre-heat to the nebulizer. Cartridge heaters were used to heat the sampling chamber and the coalesce filter. The insulation used was 1/2 inch (12.7 mm) ceramic blanket material that was wired on to the system and then covered using an insulation repair wrap.

- Initial testing of the system using a 5 wt% $CeCl_3$-LiCl-KCl salt demonstrated that the Collision nebulizer worked for molten salts. In addition, the optimal gas pressures and laser energies were found to be 10-15 psi and 90 mJ, respectively. During this test, a significant amount of material had passed through the 1.0 μm filter and was lost in the cooling system.

- Prior to the second shakedown test, several modifications were made to improve the system performance. The nebulizer seal placement was explored and it was found that

a more evenly distributed seal worked best to prevent salt leaking. In addition, the 1.0 μm filter was replaced with a 0.5 μm filter to prevent material loss. The second test was done using 3 wt% $CeCl_3$ salt. Here, a 1 jet nebulizer was used and the optimal pressure was found to be 12-15 psi. Following this test, a significant amount of leaking was observed at the nebulizer lid and the Deacon 770-L thread sealant had continued to off-gas despite being already cured. This contributed to oxide formation and increased salt leaking as the seal degraded.

- A new sampling chamber was designed to eliminate the need for the Deacon 770-L seal material. In this design, Swagelok fittings were welded to the sampling chamber. Pockets were machined into the sampling chamber that sealed sapphire windows with a 12 mm aperture. In addition, the sampling chamber had a sudden expansion prior to the LIBS analysis which reduced the mixing of aerosol particles in the sampling volume. To further reduce particle interaction with the laser pulse, or at least the effect of the interaction, a 3X beam expander was used. To reduce the amount of material that passed through the filters, two filters were set up in series. The first was a 1.0 μm filter and the second was a 0.5 μm filter. With all of these changes, a new insulation (alumina fiber board) was carved and assembled around the system so it could easily be removed with dust free between experiments. The last improvement was purchasing a custom grafoil seal to be used for the main nebulizer seal.

Cerium Aerosol-LIBS Experiments

Materials and Methods

- Samples containing between 0 to 5 wt% $CeCl_3$ in a eutectic LiCl-KCl salt (44 wt% LICl and 56 wt% KCl) were prepared. Here, the LiCl-KCl salts were mixed, dried, then melted at 500°C prior to adding the $CeCl_3$. These prepared salts were crushed and then loaded into the nebulizer through the spout.

- The system operating temperatures for the gas pre-heat, nebulizer inlet, molten salt, sampling chamber, 1.0 μm filter, and the 0.5 μm filter were 550°C, 130°C, 470°C, 260°C, 500°C, and 60°C, respectively. The operating pressure was maintained at 12 psi and the laser energy was 50 mJ

- The gate delay was studied between 100 ns and 25 μs. In this study, three repetitions comprising of 250 laser pulses were done. The SBR was used and the optimal gate delay was found to be 16 μs. This value was used for the remainder of the Ce work.

Results and Discussions

- The %RSD for a typical experiment was found to be approximately 4.8%; however, the signal intensity across the entire spectra decreased from experiment to experiment. This led to an 80% %RSD between the different experiments. To make the results more meaningful, the spectra were normalized using the Li 460 nm peak. With the normalization, the %RSD between the different experiments was on average 15%. The %RSD values for the individual spectral lines were calculated to be on an order of 5%.

- Univariate calibration curves were made using the peak areas and intensities of the 418.660 nm, 428.999 nm, and 457.228 nm lines. In general the peak area curves had lower LOD and similar RMSECV. The best calibration curve was the 418.660 nm curve using the peak area response. For this curve, the LOD and RMSECV were 148 ppm and 647 ppm, respectively.

- In the multivariate calibration, 7 LV were used to form the model yielding the RMSECV of 622 ppm. With the validation set, the RMSEP was calculated to be 762 ppm. A summary of the univariate and multivariate results are shown in Table 7.2. Results between the univariate and multivariate calibration approaches were similar.

- The analytical results found in this study are similar to results found in the literature. Being that the Ce and other rare earth elements in the ER had concentrations around

1 wt%, it was anticipated that the aerosol-LIBS system was capable of accurately monitoring and quantifying pyroprocessing salts.

Table 7.2: Summary of the Ce aerosol-LIBS results.

%RSD	5%
Univariate	
b_1	0.0195
b_0	4.9E-03
R^2	0.9976
LOD (ppm)	148
RMSECV (ppm)	647
Multivariate	
LV	7
RMSECV (ppm)	622
RMSEP (ppm)	762

7.1.6 Molten UCl_3 in Molten Salt

Materials and Methods

- To explore the complex U signal, DU metal was analyzed using the same setup as used for the aerosol-LIBS system. After removing the sampling chamber, the DU metal was positioned in its place. Three gate delays were explored at 1 μs, 5 μs, and 16 μs. Each gate delay was a compilation of 5 different spots (repetitions), each comprising of 150 laser pulses. Each spot size was approximately 1 mm in diameter.

- For the aerosol-LIBS experiments, the overall system was not modified; however, the optics were removed and cleaned which resulted in miss-alignment and consequently, a 20% reduction in signal and hot spots in the laser beam profile. These hot spots caused optical damage and degradation to the sapphire window over time.

- To prevent the spread of contamination and to reduce U waste, system components were not removed from the glovebox. One exception was the sapphire windows which

were wiped with chem-wipes prior to being transferred out and for cleaning and inspection. These windows were frisked with a geiger counter to ensure no material was being spread outside the glovebox. The rest of the components were hand scraped to remove residual salts. The 1.0 μm filter was changed for every experiment to prevent buildup of material and increased pressure drop.

- Depleted UCl_3 content (from the Idaho National Laboratory) was used to prepare 9 samples with UCl_3 concentrations ranging from 0.3 wt% to 5 wt%. Here, the LiCl and KCl salts were dried at 250°C prior to being melted at 500°C. Following melting, the UCl_3 was added and melted to form a ternary salt. Melting was done for 3 hours to ensure a homogeneous salt.

- Salt samples were collected from the melt using a stainless steel rod. The oxide layer was not sampled. This led to variation in the ICP-MS results which were overcome by using a crushed sample approach. In addition to the bulk salt, samples were taken from different locations within the system to measure the concentration distribution of U in the salt. Samples measured via ICP-MS were prepared in a 5% nitric acid solution and then diluted between 100X and 3000X to get below the EPA limit of 30 μg/L of U.

- For these experiments, a total of six repetitions per sample were taken, each comprising of 300 laser pulses at 2 Hz. The operating pressure was 12 psi and the laser energy was 50 mJ.

- The first three experiments were operated without the gas pre-heat to assess the nebulizer inlet gas temperature effect. The remaining six experiments were conducted with the gas pre-heat to explore the gate delay and concentration effect of the aerosol-LIBS system with heavy elements.

Results and Discussions

- Results from the DU metal tests were consistent with spectra found in the literature. The only deviation in the results was in the region lower than 400 nm where the fiber optic cable used had substantially reduced optical transmission. It was found that the background observed in the spectra did not decay at a different rate as the spectral lines. The observation was an effect of low spectral resolution and a high density of U lines. With this finding, the SBR was not ideal for determining the optimal timing and the shortest gate delay was selected to increase signal intensity.

- For the U aerosol experiments, the first three tests were done without the gas pre-heat. It was observed that without this heating, the U concentration in the system decreased as the distance from the nebulizer increased. Changing the gas flow rate resulted in different concentration profiles with a higher flow rate of gas yielding a flatter slope. However, for the pressures and flow rates studied, the concentration of U at the 0.5 μm filter was low. The exact mechanism for this was not explored. The remaining experiments were conducted with the gas pre-heat set at 550°C yielding relatively flat concentration profiles.

- The spectrum obtained from the 1 wt% UCl_3 salt was normalized and compared to the pure LiCl-KCl salt spectrum from the previous Ce study. From the comparison, spectral features unique to the U composition were highlighted. Using this approach, numerous spectral lines were observed in the spectrum and verified in the literature. Three prominent peaks were selected for analysis; the U II 367.01 nm, U II 385.96 nm, and U I 387.10 nm lines.

- The gate delay was studied between 3 μs and 25 μs. Here, the same background effect that was observed for the DU metal experiment was present. As a result, the 3 μs gate delay was selected to maximize the intensity.

- Normalization was done using the Li 610.3 nm line. With this normalization, the average %RSD value between the different repetitions was 4.5% with lower values

being calculated for the experiments containing higher concentrations of U. The overall %RSD between the different experiments in the region with no U lines was 15%.

- The univariate calibration curves were generated using the peak areas and intensities. All of the curves had a linear trend; however, the peak area curves had substantially better R^2 values and LOD. The best curve was generated from the 367.01 nm peak which had an R^2 value of 0.9917 and a LOD of 0.0647 wt% (647 ppm). The RMSECV for this curve was 0.229 wt%.

- The PLS model was generated using all of the collected spectra for calibration. Using 6 LV, the curve RMSECV (venetian blinds) was 0.111 wt% which is 66% better than the univariate case. The LOOCV cross calibration yielded even better results with a RMSECV of 0.085 wt%. In this case, the PLS model was recommended for future use over the univariate calibration approach. Table 7.3 shows a summary of the U results.

- The aerosol-LIBS results for U were compared to the literature and the 647 ppm LOD calculated was in the mid-range for reported value ranges.

- It was shown from the literature that U concentrations within the ER after electrorefining would typically be between 1 to 2 wt% UCl_3. In these concentration ranges, the aerosol-LIBS system could be used for near real-time quantification and monitoring of U.

- With the successful testing of molten LiCl-KCl salts containing Ce and U, the aerosol-LIBS approach appeared to be a strong alternative to the current ICP-MS sampling approach for material accountability and safeguards of pyroprocessing salts.

7.2 Recommendations

- Aerosol characterization: The focus of this work was on the spectral response of the aerosol-LIBS system. Definitely, advances in the spectral signal and repeatability can

Table 7.3: Summary of the U aerosol-LIBS results. The RMSECV for the PLS model was calculated in two ways, venetian blinds and LOOCV.

%RSD	4.5%
Univariate	
b_1	0.2488
b_0	-0.015
R^2	0.9917
LOD (wt%)	0.0647
RMSECV (wt%)	0.229
Multivariate	
LV	6
RMSECV (wt%)	0.111 or 0.085

be achieved by understanding the effect of the aerosol density and size distribution on LIBS. Due to the difficulty of matching a surrogate fluid for molten salt, high temperature tolerant characterization methods would need to be utilized. In addition, it is possible that the Collison nebulizer does not deliver the ideal aerosol characteristics for a LIBS measurement. As a result, it is recommended that alternative nebulizers be explored. Nebulizers for these extreme conditions are limited, but it appears that cone spray and v-groove type nebulizers may perform well with high solids and elevated temperatures. In addition, a spray chamber following the aerosol generation, to sort the aerosol particle size prior to sampling, may enhance the LIBS measurement.

- Multi-component analysis: In this work, only single-component systems were studied in molten salt. Electrorefiner salt will contain a large range of elements, many of which are rare earth and actinides, where a high density of spectral lines will complicate the spectra. To better assess the feasibility of LIBS as an analytical technique, multi-component testing using the aerosol-LIBS system is recommended.

- Sampling chamber: Throughout this work, particle interaction (scattering) with the laser pulse was observed which led to higher %RSD values. In addition, the optical windows in the sampling chamber would degrade over time due to dust on the windows. To mitigate these challenges, it is recommended that a new sampling chamber be

redesigned to specifically address these issues. One approach could be to use a sheath gas around the incoming aerosol stream.

- System orientation: In this work, the system was oriented horizontally with the laser light entering from the top with the bottom of the sampling chamber acting as the beam stop. This had several consequences: (i) particles in the gas stream would drop out as a result of gravity and deposit on the bottom of the tubing, and (ii) the incoming laser light hitting the bottom of the sampling chamber would disperse dust into the chamber. By orienting the entire system vertically with the aerosol flow going downwards, gravity would work to the advantage. In addition, with this configuration, the laser beam stop could be outside of the sampling chamber to prevent material splashing.

- Optical considerations: In all of the conducted high temperature studies, signal degradation occurred, presumably due to miss-alignment and surface films forming on the optics. These issues must be addressed. The first challenge can be mitigated by designing more stable platforms where the optics can be removed and replaced without optical miss-alignment. The second can be mitigated by using protective gas layers (flowing) around the optics.

Chapter 8

References

1. Robert G, C. & Tsoulfanidis, N. The Nuclear Fuel Cycle: Analysis and Management. *American Nuclear Society, La Grange Park, Illinois* (1990).

2. Shultis, J. K. & Faw, R. E. Fundamentals of Nuclear Science and Engineering. *CRC Press, Boca Raton* (2008).

3. Andrews, A. Nuclear Fuel Reprocessing: U. S. Policy Development. *Congressional Research Service, Order Code: RS22542* (2008).

4. Laidler, J., Battles, J., Miller, W., Ackerman, J. & Carls, E. Development of Pyroprocessing Technologies. *Progress Nuclear Energy* **31,** 131 (1997).

5. Garcia, H. E., Lineberry, M. J., Aumeier, S. E. & McFarlane, H. F. Proliferation Resistance of Advanced Sustainable Nuclear Fuel Cycles. *Nuclear Plant Journal* **20,** 18–27 (2002).

6. Phongikaroon, S. & Simpson, M. Equilibrium Model for Ion Exchange between Multivalent Cations and Zeolite-A in a Molten Salt. *AIChE Journal* **52,** 1736–1743 (2006).

7. Pasquini, C., Cortez, J., Silva, L. M. C. & Gonzaga, F. B. Laser Induced Breakdown Spectroscopy. *Journal of the Brazilian Chemical Society* **18,** 463 (2007).

8. Effenberger, A. J. *Methods for Measurement of Heterogeneous Materials with Laser-Induced Breakdown Spectroscopy (LIBS)* ProQuest/UMI. (Publication No. 3369015.) PhD thesis (University of California, San Diego, 2009).

9. Hanson, C., Phongikaroon, S. & Scott, J. R. Temperature effect on laser-induced breakdown spectroscopy spectra of molten and solid salts. *Spectrochimica Acta Part B: Atomic Spectroscopy* **97,** 79–85 (2014).

10. Weisberg, A., Lakis, R., Simpson, M. F., Horowitz, L. & Craparo, J. Measuring Lanthanide Concentrations in Molten Salt Using Laser-Induced Breakdown Spectroscopy (LIBS). *Applied Spectroscopy* **68,** 937–948 (2014).

11. Smith, N. A., Savina, J. A. & Williamson, M. A. Application of Laser-Induced Breakdown Spectroscopy to Electrochemical Process Monitoring of Molten Chloride Salts. *IAEA: Symposium on International Safeguards, Vienna, Austria, Oct. 20-24* (2014).

12. Koch, L. J. Experimental Breeder Reactor II: An Integrated Experimental Fast Reactor Nuclear Power Station. *American Nuclear Society, La Grange Park, Illinois* (2008).

13. Willit, J. L., Miller, W. E. & Battles, J. E. Electrorefining of Uranium and Plutonium - A Literature Review. *Journal of Nuclear Materials* **195,** 229–249 (1992).

14. Nawada, H. P. & Fukuda, K. Role of Pyro-Chemical Processes in Advanced Fuel Cycles. *Journal of Physics and Chemistry of Solids* **66,** 647–651 (2005).

15. Inoue, T. & Koch, L. Development of Pyroprocessing and its Future Direction. *Nuclear Engineering and Technology* **340,** 183–190 (2008).

16. Miziolek, A. W., Palleschi, V. & Schechter, I. Laser-Induced Breakdown Spectroscopy (LIBS) Fundamentals and Applications. *Cambridge University Press, Cambridge, UK* (2006).

17. Brech, F. & Cross, L. Optical Microemission Stimulated by a Ruby MASER. *Applied Spectroscopy* **59,** 59 (1962).

18. Chinni, R. C., Cremers, D., Radziemski, L. J., Bostian, M. & Navarro-Northrup, C. Detection of Uranium using Laser-Induced Breakdown Spectroscopy. *Applied Spectroscopy* **63,** 1238–1250 (2009).

19. Wachter, J. R. & Cremers, D. A. Determination of Uranium in Solution Using Laser-Induced Breakdown Spectroscopy. *Applied Spectroscopy* **41,** 1042–1048 (1987).

20. St-Onge, L., Kwong, E., Sabsabi, M. & Vadas, E. B. Rapid Analysis of Liquid Formulations Containing Sodium Chloride using Laser-Induced Breakdown Spectroscopy. *Journal of Pharmaceutical and Biomedical Analysis* **36,** 277 (2004).

21. Barreda, F., Trichard, F., Barbier, S., Gilon, N. & Saint-Jalmes, L. Fast Quantitative Determination of Platinum in Liquid Samples by Laser-Induced Breakdown Spectroscopy. *Analytical and Bioanalytical Chemistry* **403,** 2601–2610 (2012).

22. Tambay, R. & Thareja, R. Laser-Induced Breakdown Studies of Laboratory Air at 0.266, 0.355, 0.532, and 1.06 μm. *Journal of Applied Physics* **70,** 2890–2892 (1991).

23. Martin, M. Z., Cheng, M. & Martin, R. C. Aerosol Measurement by Laser-Induced Breakdown Spectroscopy: A Review. *Aerosol Science and Technology* **31,** 409 (1991).

24. Cahoon, E. M. & Almirall, J. R. Quantitative Analysis of Liquids from Aerosol and Microdrops using Laser Induced Breakdown Spectroscopy. *Analytical Chemistry* **84,** 2239–2244 (2012).

25. Sarkar, A., Alamelu, D. & Aggarwal, S. K. Determination of Thorium and Uranium in Solution by Laser-Induced Breakdown Spectrometry. *Applied Optics* **47,** G58–G64 (2008).

26. Sarkar, A., Alamelu, D. & Aggarwal, S. K. Gallium Quantification in Solution by LIBS in the Presence of Bulk Uranium. *Optics & Laser Technology* **44,** 30 (2012).

27. Singh, J. P., Yueh, F., Zhang, H., Carney, K. P. & Krsul, J. A Preliminary Study of the Determination of Uranium, Plutonium, and Neptunium by Laser-Induced Breakdown Spectroscopy. *U. S. Department of Energy, DIAL 10575* (1996).

28. Sirven, J., Pailloux, A., M'Baye, Y., Coulon, N., Alpettaz, T. & Gosse, S. Towards the Determination of the Geographical Origin of Yellow Cake Samples by Laser-Induced Breakdown Spectroscopy and Chemometrics. *Journal of Analytical Atomic Spectrometry* **24,** 451–459 (2009).

29. Judge, E. J., II, J. E. B., Berg, J. M., Clegg, S. M. & Havrilla, G. J. Laser-Induced Breakdown Spectroscopy Measurements of Uranium and Thorium Powders and Uranium Ore. *Spectrochimica Acta Part B: Atomic Spectroscopy* **83-84,** 28–36 (2013).

30. Fichet, P., Mauchien, P. & Moulin, C. Determination of Impurities in Uranium and Plutonium Dioxides by Laser-Induced Breakdown Spectroscopy. *Applied Spectroscopy* **53,** 1111–1117 (1999).

31. Zheng, H., Yueh, F. Y., Miller, T., Singh, J. P., Zeigler, K. E., & Marra, J. C. Analysis of Plutonium Oxide Surrogate Residue using Laser-Induced Breakdown Spectroscopy. *Spectrochimica Acta Part B: Atomic Spectroscopy* **63,** 968–974 (2008).

32. Sarkar, A., Alamelu, D. & Aggarwal, S. K. Laser-Induced Breakdown Spectroscopy for Determination of Uranium in Thorium-Uranium Mixed Oxide Fuel Materials. *Talanta* **78,** 800 (2009).

33. Barefield, J. E., Judge, E. J., Berg, J. M., Willson, S. P., Le, L. A. & Lopez, L. N. Analysis and Spectral Assignments of Mixed Actinide Oxide Samples Using Laser-Induced Breakdown Spectroscopy (LIBS). *Applied Spectroscopy* **2013,** 433–440 (67).

34. Smith, C., Martinez, M., Veirs, D. & Cremers, D. Pu-239/Pu-240 isotope ratios determined using high resolution emission spectroscopy in a laser-induced plasma. *Spectrochimica Acta Part B: Atomic Spectroscopy* **57,** 929–937 (2002).

35. Doucet, F. R., Lithgow, G., Kosierb, R., Bouchard, P. & Sabsabi, M. Determination of Isotope Ratios using Laser-Induced Breakdown Spectroscopy in Ambient Air at Atmospheric Pressure for Nuclear Forensics. *Journal of Analytical Atomic Spectrometry* **26,** 536–541 (2011).

36. Tampo, M., Miyabe, M., Akaoka, K., Oba, M., Ohba, H., Maruyama, Y. & Wakaida, I. Enhancement of Intensity in Microwave-Assisted Laser-Induced Breakdown Spectroscopy for Remote Analysis of Nuclear Fuel Recycling. *Journal of Analytical Atomic Spectrometry* **29,** 886–892 (2014).

37. Emmert, L. A., Chinni, R. C., Cremers, D. A., Jones, C. R. & Rudolph, W. Comparative Study of Femtosecond and Nanosecond Laser-Induced Breakdown Spectroscopy of Depleted Uranium. *Applied Optics* **50,** 313–317 (2011).

38. Hanson, C. *Laser-Induced Breakdown Spectroscopy - Temperature Effects on Spectra of Molten Salt Systems* PhD thesis (University of Idaho, Idaho Falls, Idaho, 2013).

39. Bryce, K., Williams, A. N., Kim, S. H. & Phongikaroon, S. Laser-Induced Breakdown Spectroscopy(LIBS) Detections of Gadolinium in Solid LiCl-KCl Salt Samples. *American Nuclear Society–Winter, Washington DC, Nov.* (2015).

40. Park, D., Han, B., Park, S. & Ku, J. Quantitative Analysis of Uranium Spectra in Molten Eutectic LICl-KCl+UCl3 using LIBS. *International Pyroprocessing Research Conference, Jeju Island, Korea, Sept.* (2016).

41. Yoo, B., Kim, S. H. & Lee, J. Quantitative Analysis of Molten Salt by Laser-Induced Breakdown Spectroscopy. *GLOBAL 2015, Paris, France, Sept.* (2015).

42. Kim, S. H., Lee, J. & Phongikaroon, S. The Remote Compositional Analysis of Molten Salt (KF-LiF-ZrF4) by Probe Assisted In-Situ LIBS System. *American Nuclear Society-Winter, Washington DC, Nov.* (2015).

43. Cho, Y., Park, G., Lee, H. & Kim, I. Concentration of Cesium and Strontium elements involved in a LiCl Waste Salt by Melt Crystallization Process. *Nuclear Technology* **171,** 325 (2010).

44. Choi, J., Cho, Y., Lee, T., Eun, H., Kim, J., Kim, I., Park, G. & Kang, J. Inclusion Behavior of Cs, Sr, and Ba Impurities in LiCl Crystal Formed by Layer-Melt Crystal-

lization: Combined First-Principals Calculations and Experimental Study. *Journal of Crystal Growth* **371,** 84–89 (2013).

45. Williams, A. N., Phongikaroon, S. & Simpson, M. Separation of CsCl from Ternary CsCl-LiCl-KCl salt via a Melt Crystallization Technique for Pyroprocessing Waste Minimization. *Chemical Engineering Science* **89,** 258–263 (2013).

46. Versey, J. R., Phongikaroon, S. & Simpson, M. Separation of CsCl from LiCl-CsCl molten salt by Cold Finger Crystallization. *Nuclear Engineering and Technology* **46,** 395–406 (2014).

47. Williams, A. N., Pack, M. & Phongikaroon, S. Separation of Strontium and Cesium from Ternary and Quaternary Lithium Chloride-Potassium Chloride Salts via Melt Crystallization. *Nuclear Engineering and Technology* **47,** 867–874 (2015).

48. Yun, J., Klenze, R. & Kim, J. Laser-Induced Breakdown Spectroscopy for the On-Line Multielement Analysis of Highly Radioactive Glass Melt. Part I: Characterization and Evaluation of the Method. *Applied Spectroscopy* **56,** 437–448 (2002).

49. Yun, J., Klenze, R. & Kim, J. Laser-Induced Breakdown Spectroscopy for the On-Line Multielement Analysis of Highly Radioactive Glass Melt. Part II: Analysis of Molten Glass Samples. *Applied Spectroscopy* **56,** 852–858 (2002).

50. Gruber, J., Heitz, J., Arnold, N., Bauerle, D., Ramaseder, N., Meyer, W., Hochortler, J. & Koch, F. In Situ Analysis of Metal Melts in Metallurgic Vacuum Devices by Laser-Induced Breakdown Spectroscopy. *Applied Spectroscopy* **58,** 457–462 (2004).

51. Cremers, D. A., Radziemski, L. J. & Loree, T. R. Spectrochemical Analysis of Liquids Using the Laser Spark. *Applied Spectroscopy* **38,** 721–729 (1984).

52. Pearman, W., Scaffidi, J. & Angel, S. M. Dual-Pulse Laser-Induced Breakdown Spectroscopy in Bulk Aqueous Solution with an Orthogonal Beam Geometry. *Applied Optics* **42,** 6085–6093 (2003).

53. Cheung, N. H. & Yeung, E. S. Single-shot Elemental Analysis of Liquids based on Laser Vaporization below Breakdown. *Applied Spectroscopy* **47,** 882–886 (1993).

54. Lucas, J. M., Sabsabi, M. & Heon, R. *US patent* US 6,909,505 B2

55. Kumar, A., Fang, F. Y. & Singh, J. P. Double-Pulsed Laser-Induced Breakdown Spectroscopy with Liquid Jets of Different Thicknesses. *Applied Optics* **42,** 6047–6051 (2003).

56. Feng, Y., Yang, J., Fan, J., Yao, G., Ji, X., Zhang, X., Zheng, X. & Cui, Z. Investigation of Laser-Induced Breakdown Spectroscopy of a Liquid Jet. *Applied Optics* **49,** 70–74 (2010).

57. Yaroshchyk, P., Morrison, R. J. & D. Bod and, B. L. C. Quantitative Determination of Wear Metal in Engine Oils using Laser-Induced Breakdown Spectroscopy: A Comparison between Liquid Jets and Static Liquid. *Spectrochimica Acta Part B: Atomic Spectroscopy* **60,** 986–992 (2005).

58. Fisher, B. T., Johnson, H. A., Buckley, S. G. & Hahn, D. W. Temperol Gating for the Optimization of Laser-Induced Breakdown Spectroscopy Detection and Analysis of Toxic Metals. *Applied Spectroscopy* **55,** 1312–1319 (2001).

59. Carranza, J. E., Fisher, B. T., Yoder, G. D. & Hahn, D. W. On-line Analysis of Ambient Air Aerosols using Laser-Induced Breakdown Spectroscopy. *Spectrochemica Acta Part B: Atomic Spectroscopy* **56,** 851 (2001).

60. Carranza, J. E. & Hahn, D. W. Sampling Statistics and Considerations for Single-Shot Analysis using Laser-Induced Breakdown Spectroscopy. *Spectrochemica Acta Part B: Atomic Spectroscopy* **57,** 779–790 (2002).

61. Diwakar, P. K., Looper, K. H., Matiaske, A. & Hahn, D. W. Laser-Induced Breakdown Spectroscopy for Analysis of micro and nanoparticles. *Journal of Analytical Atomic Spectrometry* **27,** 1110–1119 (2012).

62. Huang, J. S., Ke, C. B., Huang, L. S. & Lin, K. C. The Correlation between Ion Production and Emission Intensity in the Laser-Induced Breakdown Spectroscopy of Liquid Droplets. *Spectrochimica Acta Part B: Atomic Spectroscopy* **57,** 35 (2002).

63. J. Huang C. Ke, K. L. Matrix Effect on Emission/Current Correlated Analysis in Laser-Induced Breakdown Spectroscopy of Liquid Droplets. *Spectrochimica Acta Part B: Atomic Spectroscopy* **59,** 321 (2004).

64. Poulain, D. E. & Alexander, D. R. Influences on Concentration Measurements of Liquid Aerosols by Laser-Induced Breakdown Spectroscopy. *Applied Spectroscopy* **49,** 569–579 (1995).

65. Schechter, I. Direct Aerosol Analysis by Time Resolved Laser Plasma Spectroscopy – Improvement by single shot Measurements. *Analytical Science and Technology* **8,** 779–786 (1995).

66. Kumar, A., Yueh, F. Y., Miller, T. & Singh, J. P. Detection of Trace Elements in Liquids by Laser-Induced Breakdown Spectroscopy with a Meinhard Nebulizer. *Applied Optics* **42,** 6040–6046 (2003).

67. Martin, M. & Cheng, M. Detection of Chromium Aerosol Using Time-Resolved Laser-Induced Plasma Spectroscopy. *Applied Spectroscopy* **54,** 1279–1285 (2000).

68. Alvarez-Trujillo, L., Ferrero, A. & Laserna, J. J. Preliminary Studies on Stand-off Laser-Induced Breakdown Spectroscopy Detection in Aerosols. *Journal of Analytical Atomic Spectrometry* **23,** 885–888 (2008).

69. Kramida, A., Ralchenko, Y., J., R. & Team, N. A. *NIST Atomic Spectra Database (version 5.3)* <`http://physics.nist.gov/asd`> (2015).

70. Spiegel, M. R. & DiFranco, D. Statistics. *McGraw-Hill, New York, NY* (1996).

71. Cremers, D. A. & Radziemski, L. J. Handbook of Lase-Induced Breakdown Spectroscopy, Second Edition. *John Wiley & Sons, UK* (2013).

72. Navidi, W. Statistics for Engineers and Scientist. *McGraw-Hill, New York, NY* (2008).

73. Bevington, P. R. & Robinson, D. K. Data Reduction and Error Analysis for the Physical Sciences. *McGraw-Hill, New York, NY* (2003).

74. Shi, Q., Niu, G., Lin, Q., Xu, T., Li, F. & Duan, Y. Quantitative Analysis of Sedimentry Rocks using Laser-Induced Breakdown Spectroscopy: Comparision of Support Vector Regression and Partial Least Squares Regression Chemometric Methods. *Journal of Analytical Atomic Spectrometry* **30,** 2384 (2015).

75. Andrade, J. M., Cristoforetti, G., Legnaioli, S., Lorenzetti, G., Palleschi, V. & Shaltout, A. A. Classical Univariate Calibration and Partial Least Squares for Quantitative Analysis of Brass Samples by Laser-Induced Breakdown Spectroscopy. *Spectrochimica Acta Part B: Atomic Spectroscopy* **65,** 658–663 (2010).

76. Gottfried, J. L., Harmon, R. S., F. C, D.-L. & Miziolek, A. W. Multivariate Analysis of Laser-Induced Breakdown Spectroscopy Chemical Signatures for Geomaterial Classification. *Spectrochimica Acta Part B: Atomic Spectroscopy* **64,** 1009–1019 (2009).

77. Laville, S., Sabasbi, M. & Doucet, F. R. Multi-elemental Analysis of Solidified Mineral Melt Samples by Laser-Induced Breakdown Spectroscopy Coupled with a Linear Multivariate Calibration. *Spectrochimica Acta Part B: Atomic Spectroscopy* **62,** 1557–1566 (2007).

78. Tripathi, M. M., Esteller, K. E., Yueh, F. & Singh, J. P. Multivariate Calibration of Spectra Obtained by Laser-Induced Breakdown Spectroscopy of Plutonium Oxide Surrogate Residues. *Spectrochimica Acta Part B: Atomic Spectroscopy* **64,** 1212–1218 (2009).

79. Yaroshchyk, P., Death, D. L. & Spencer, S. J. Comparison of Principle Components Regression, Partial Least Squares Regression, multi-Block partial Least Squares Regression, and Serial Partial Least Squares Regression Algorithms for the Analysis of Fe in Iron Ore Using LIBS. *Journal of Analytical Atomic Spectrometry* **27,** 92–98 (2012).

80. Zaytsev, S. M., Popov, A. M., Chernykh, E. V., Voronina, R. D., Zorov, N. B. & Labutin, T. A. Comparison of single- and Multivariate Calibration for Determination of Si, Mn, Cr, and Ni in High-Alloyed Stainless Steels by Laser-Induced Breakdown Spectrometry. *Journal of Analytical Atomic Spectrometry* **29,** 1417 (2014).

81. Clegg, S. M., Sklute, E., Dyar, M. D., Barefield, J. E. & Wiens, R. C. Multivariate Analysis of Remote Laser-Induced Breakdown Spectroscopy Spectra using Partial Least Squares, Principle Component Analysis and Related Techniques. *Spectrochimica Acta Part B: Atomic Spectroscopy* **64,** 79–88 (2009).

82. Geladi, P. & Kowalski, B. R. Partial Least-Squares Regression: A Tutorial. *Analtica Chimica Acta* **185,** 1–17 (1986).

83. Wold, S., Sjostrom, M. & Eriksson, L. PLS-Regression: A Basic Tool for Chemometrics. *Chemometrics and Intelligent Laboratory Systems* **58,** 109–130 (2001).

84. Yeniay, O. & Goktas, A. PLS-Regression: A Basic Tool for Chemometrics. *Hacettape Journal of Mathematics and Statistics* **31,** 99–111 (2002).

85. Reisfeld, B. & A. N, M. Computational Toxicology: Volume II, Methods in Molecular Biology. *Springer Science + Business Media, LLC* (2013).

86. May, K. R. The Collison Nebulizer: Description, Performance and Application. *Journal of Aerosol Science* **4,** 235 (1973).

87. Janz, G. J., Allen, C. B., Bansal, N. P., Murphy, R. M. & Tomkins, R. P. T. Physical Properties Data Compilations Relevant to Energy Storage. II. Molten Salts: Data on Single and Multi-Component Salt Systems. *National Bureau of Standards, U.S. Department of Commerce* (1979).

88. Munson, B. R., Young, D. F. & Okiishi, T. H.

89. Hinds, W. C. Aerosol Technology, Properties, Behavior, and Measurements of Airborne Particles. *John Wiley & Sons, Canada* (1999).

90. Martin, M. Z., Allman, S., Brice, D. J., Martin, R. C. & Andre, N. O. Exploring Laser-Induced Breakdown Spectroscopy for Nuclear Materials Analysis and In-Situ Applications. *Spectrochimica Acta Part B: Atomic Spectroscopy* **74-75,** 177–183 (2012).

91. Gong, Y., Choi, D., Han, B., Yoo, J., Han, S. & Lee, Y. Remote Quantitative Analysis of Cerium through a Shielded Window by Stand-Off Laser Induced Breakdown Spectroscopy. *Journal of Nuclear Materials* **453,** 8–15 (2014).

92. Bean, R. Project Report on Development of a Safeguards Approach for Pyroprocessing. *Idaho National Laboratory Report, INL/EXT-10-20057* (2010).

93. Bucenieks, I. E. High Pressure and High Flowrate Induction Pumps with Permanent Magnets. *Magnetohydrodynamics* **39,** 411–417 (2003).

94. Bucenieks, I. E., Sukhovich, E. P. & Shcerbinin, E. A Centrifugal Pump Based on Rotating Permanent Magnets. *Magnetohydrodynamics* **36,** 157–163 (2000).

95. Bucenieks, I. E. Perspectives of Using Rotating Permanent Magnets in the Design of Electromagnetic Induction Pumps. *Magnetohydrodynamics* **36,** 151–156 (2000).

96. Bucenieks, I. E. & Kravalis, K. Efficiency of EM Induction Pumps with Permanent Magnets. *Magnetohydrodynamics* **47,** 89–96 (2011).

97. *Evaluation of Parameters of Powerful Electromagnetic Induction Pumps on Permanet Magnets for Heavy Liquid Metals* (Rome, Italy, 2007).

98. Bucenieks, I. E., Kravalis, K. & Krishbergs, R. Pressure-Flow Rate Characteristics of Pumps with Permanent Magnets. *Magnetohydrodynamics* **47,** 97–104 (2011).

99. Bucenieks, I. E., Krishbergs, R., Kravalis, K., Lispbergs, G. & Shishko, A. Magnetic Field Distribution in the Rotor of the Permanent Magnets. *The 15th Riga and 6th PAMIR Conference on the Fundamental and Applied MHD* (2005).

100. Butzek, M. & Bucenieks, I. Proposed Mercury Pump for EES. *16th Meeting of the International Collaboration on Advanced Neutron Sources, Dusseldorf-Neuss, Germany* (2003).

101. Teotia, V., Malhotra, S., Singh, K. & Mahapatra, U. Analysis and Design of Electromagnetic Pump. *Proceedings of the COMSOL Conference 2010, Bangalore, India* (2010).

102. Peng, Y. & Zhao, L. Experimental Study on Alternating Magnetic Field Magnetohydrodynamic Pump. *Journal of Hydrodynamics* **20,** 591–595 (2009).

103. Kogawa, H., Haga, K., Wakui, T. & Futakawa, M. Development on Mercury Pump for JSNS. *Nuclear Instruments and Methods in Physics Research A* **600,** 97–99 (2009).

Appendix A

MATLAB Code

A.1 Import files from Andor Software

```
%% Reads in raw data files collected from the Andor 5000
   Spectrometer
% See asc file for parameters
% PROGRAM DESCRIPTION
% Calculates the mean spectra per repetition and the mean spectra
   between
% repetitions. Standard deviations between the repetitions are
   also
% calculated.
% Plots the repetitions and the %RSDs and saves as 300 dpi png
   file.
% Save variables lamba_MSU8 and spectra_MSU8 into a file named
% MSU8_Data_Import
% Created by Ammon N Williams

close all; clear all;

%% Import data files {filename.asc}
```

```
15 run1 = importdata('MSU8 Rep 1.asc');
16 run2 = importdata('MSU8 Rep 2.asc');
17 run3 = importdata('MSU8 Rep 3.asc');
18 run4 = importdata('MSU8 Rep 4.asc');
19 run5 = importdata('MSU8 Rep 5.asc');
20 run6 = importdata('MSU8 Rep 6.asc');
21
22 %% Set up Dummy Variables
23 lamba_1 = run1(1:end,1);
24 Spectra_1_1 = run1(1:end,2:end);
25 Spectra_1_2 = run2(1:end,2:end);
26 Spectra_1_3 = run3(1:end,2:end);
27 Spectra_1_4 = run4(1:end,2:end);
28 Spectra_1_5 = run5(1:end,2:end);
29 Spectra_1_6 = run6(1:end,2:end);
30
31 %% Calculate the mean spectra from the 300 shots
32 spectra_1(:,1) = mean(Spectra_1_1,2); %calculate the mean with
      respect to
33 % the column dimension 2
34 spectra_1(:,2) = mean(Spectra_1_2,2);
35 spectra_1(:,3) = mean(Spectra_1_3,2);
36 spectra_1(:,4) = mean(Spectra_1_4,2);
37 spectra_1(:,5) = mean(Spectra_1_5,2);
38 spectra_1(:,6) = mean(Spectra_1_6,2);
39
40 %% Combine all the repetitions into a single variable spectra
```

```
41 spectra(:,1:6) = spectra_1;
42
43 %% Calculate the mean spectra from all the repetitions, calculate
       the ...
44 % standard deviation between the repetitions
45 meanspectra_1(:,1) = mean(spectra,2);
46 stdev(:,1) = std(spectra,1,2);
47 percentRSD(:,1) = (stdev./meanspectra_1)*100;
48
49 %% Plot
50 figure(1);
51 hold on;
52 plot(lamba_1, spectra);
53 xlabel( 'Wavelength (nm))' );
54 ylabel( 'Intensity' );
55 legend('Rep 1','Rep 2','Rep 3','Rep 4','Rep 5','Rep 1');
56 set(gca,'XMinorTick','on','YMinorTick','on','fontsize',20)
57 print('Uranium_Rep_MS8', '-dpng', '-r300');
58
59 figure(2)
60 hold on
61 plot(lamba_1, percentRSD,'k');
62 xlabel('Wavelength (nm)');
63 set(gca,'XMinorTick','on','YMinorTick','on','fontsize',20)
64 print('Uranium_RSD_MS8', '-dpng', '-r300')
65
66
```

```
67 %% Saves the data
68 lamba_MSU8 = lamba_1;
69 spectra_MSU8 = spectra;
70 save MSU8_Data_Import lamba_MSU8 spectra_MSU8 spectra_1
```

A.2 Analyze Spectral Data

```
1  %% Loads Spectral Data from Exps, normalizes and calculates peak
       info
2  % Normalizes with repsct to the mean spectra in the user defined
       are of
3  % interest.
4  % Calculates the mean and standard deviations for indiviual and
       combined
5  % experimental data.
6  % Opens the FindXPeaks GUI to perform peak analysis
7  % Plots the different Exp spectra and combined %RSD
8  % Saves the normalized spectral data in MSU_NSpectra_Data
9  % Saves the peak analysis info in MSU_Values_XXX where XXX is the
       peak
10 % wavelength of interest, please specify.
11 % Created by Ammon N Williams
12
13 close all; clear all;
14 addpath('c:/Program Files/MATLAB') %sets the pathe to FindXPeak
15 load MS6_Data_Import
16 load MSU5_Data_Import
```

```
load MSU6_Data_Import
load MSU7_Data_Import
load MSU8_Data_Import
load MSU9_Data_Import

%% Normalize each spectra with respect to itself (use mean, not Area)
NX1 = 600; %Lower wavelength range for normalization range (nm)
NX2 = 811; %Upper wavelength range for normalization range (nm)
Xstart = size(lamba_MS6(lamba_MS6 < NX1),1); %Identifies the row n with a
% value just smaller than NX1 value.
Xend = size(lamba_MS6(lamba_MS6 < NX2),1); %Identifies the row n with a
% value just smaller than NX2 value.
MeanSpectra_MS6 = mean(spectra_MS6(Xstart:Xend,:));
% In this case, MS6 and MSU_ have different wavelength scales and must be
% addressed seperately.
Xstart = size(lamba_MSU1(lamba_MSU1 < NX1),1);
Xend = size(lamba_MSU1(lamba_MSU1 < NX2),1);
MeanSpectra_MSU5 = mean(spectra_MSU5(Xstart:Xend,:));
MeanSpectra_MSU6 = mean(spectra_MSU6(Xstart:Xend,:));
MeanSpectra_MSU7 = mean(spectra_MSU7(Xstart:Xend,:));
MeanSpectra_MSU8 = mean(spectra_MSU8(Xstart:Xend,:));
MeanSpectra_MSU9 = mean(spectra_MSU9(Xstart:Xend,:));

```

```
% Divide each spectra with respect to its own mean value from the
   range
% selected, for loops are used so that each repetition can be done
for i = 1:7 % 7 repetions
    Nspectra_MS6(:,i) = spectra_MS6(:,i)./MeanSpectra_MS6(1,i);
end
for i = 1:6 % 6 repetitions
    Nspectra_MSU5(:,i) = spectra_MSU5(:,i)./MeanSpectra_MSU5(1,i);
    Nspectra_MSU6(:,i) = spectra_MSU6(:,i)./MeanSpectra_MSU6(1,i);
    Nspectra_MSU7(:,i) = spectra_MSU7(:,i)./MeanSpectra_MSU7(1,i);
    Nspectra_MSU8(:,i) = spectra_MSU8(:,i)./MeanSpectra_MSU8(1,i);
    Nspectra_MSU9(:,i) = spectra_MSU9(:,i)./MeanSpectra_MSU9(1,i);
end
% Redefine varables
spectra_MS6 = Nspectra_MS6;
spectra_MSU5 = Nspectra_MSU5;
spectra_MSU6 = Nspectra_MSU6;
spectra_MSU7 = Nspectra_MSU7;
spectra_MSU8 = Nspectra_MSU8;
spectra_MSU9 = Nspectra_MSU9;
%% Calculate the mean normalized spectra between repetitions
meanspectra_MS6(:,1) = mean(spectra_MS6,2);
meanspectra_MSU5(:,1) = mean(spectra_MSU5,2);
meanspectra_MSU6(:,1) = mean(spectra_MSU6,2);
meanspectra_MSU7(:,1) = mean(spectra_MSU7,2);
meanspectra_MSU8(:,1) = mean(spectra_MSU8,2);
meanspectra_MSU9(:,1) = mean(spectra_MSU9,2);
```

```
66
67 %% Calculate the combined %RSD
68 % Combine all the mean spectra into a single variable
69 Spectra_U(:,1) = mean(spectra_MSU5,2);
70 Spectra_U(:,2) = mean(spectra_MSU6,2);
71 Spectra_U(:,3) = mean(spectra_MSU7,2);
72 Spectra_U(:,4) = mean(spectra_MSU8,2);
73 Spectra_U(:,5) = mean(spectra_MSU9,2);
74 mSpectra_U = mean(Spectra_U,2);% Calculate the mean of all the exp
       data
75 stdev_U(:,1) = std(Spectra_U,1,2);% Caluclate the standard
     deviation
76 percentRSD_U(:,1) = (stdev_U(:,1)./mSpectra_U(:,1))*100;%
     Calculate %RSD
77
78 %% Calculate the standard deviation and (%RSD) for select exp
79 stdev_MSU8(:,1) = std(spectra_MSU8,1,2);
80 percentRSD_MSU8(:,1) = (stdev_MSU8(:,1)./meanspectra_MSU8(:,1))
     *100;
81
82 %% Go to the GUI FindXPeak to select the start and end points of
     the
83 % peak, returns the Area, Peak Intesity, SBR and the SNR for the
     peak.
84 Peak_Wavelength = 387.1;% Peak wavelength in consideration
85 % See FindXPeak for more information
86 [AreaAndStd_MSU(1,:), Peakpoints] = ...
```

```
87      FindXPeak(lamba_MS6, spectra_MS6  , Peak_Wavelength, 7);
88  [AreaAndStd_MSU(2,:), Peakpoints] = ...
89      FindXPeak(lamba_MSU9, spectra_MSU9  , Peak_Wavelength, 6);
90  [AreaAndStd_MSU(3,:), Peakpoints] = ...
91      FindXPeak(lamba_MSU5, spectra_MSU5  , Peak_Wavelength, 6);
92  [AreaAndStd_MSU(4,:), Peakpoints] = ...
93      FindXPeak(lamba_MSU6, spectra_MSU6  , Peak_Wavelength, 6);
94  [AreaAndStd_MSU(5,:), Peakpoints] = ...
95      FindXPeak(lamba_MSU7, spectra_MSU7  , Peak_Wavelength, 6);
96  [AreaAndStd_MSU(6,:), Peakpoints] = ...
97      FindXPeak(lamba_MSU8, spectra_MSU8  , Peak_Wavelength, 6);
98
99  %% Plot
100 figure(1);
101 hold on;
102 plot(lamba_MSU9, meanspectra_MSU9,'m', ...
103     lamba_MSU5,meanspectra_MSU5,'k', ...
104     lamba_MSU6, meanspectra_MSU6,'b', ...
105     lamba_MSU7, meanspectra_MSU7,'c', ...
106     lamba_MSU8, meanspectra_MSU8,'r');
107 xlabel( 'Wavelength (nm)' );
108 ylabel( 'Normalized intensity (a.u.)' );
109 legend('0.3 wt% ','1 wt%','2 wt%','3 wt%','5 wt%','Location','
       NorthWest')
110 legend boxoff
111 % axis([384 388 0 .03]);
112 set(gca,'XMinorTick','on','YMinorTick','on','fontsize',18)
```

```
113 % print('Uranium_Concentration_Spectra', '-dpng', '-r300');
114
115 figure(2);
116 hold on;
117 plot(lamba_MSU7, percentRSD_U,'k');
118 xlabel( 'Wavelength (nm)' );
119 ylabel( '%RSD' );
120 axis([350 800 0 40])
121 set(gca,'XMinorTick','on','YMinorTick','on','fontsize',20)
122 print('Uranium_RSD_AllU', '-dpng', '-r300');
123
124 %% Saves the data
125 save MSU_Values_387  AreaAndStd_MSU
126 save MSU_NSpectra_Data lamba_MS6 spectra_MS6 ...
127     lamba_MSU5 spectra_MSU5 lamba_MSU6 spectra_MSU6 ...
128     lamba_MSU7 spectra_MSU7 lamba_MSU8 spectra_MSU8 ...
129     lamba_MSU9 spectra_MSU9
```

A.3 GUI Program

```
1 function [AreaAndStd, Peakpoints] = ...
2     FindXPeak(lamba, spectra , Xline, Reps)
3 %This function uses a GUI to identify peak start and end locations
    and then
4 % calculates the peak area, finds the intesity of the peak and
   then
5 % calculateds the standard deviation between the peak areas.
```

```
% INSTRUCTIONS
% Select the starting point and ending point of the peak in that order!
% NOTE: The data point to the LEFT of the click will be selected, no
% interpolation is done
%   Created 3\24\2015 by Ammon Williams
%   Modified 7\30\15 by Ammon Williams

%% Calculate the peak areas and intensity for each repation
nX = size(lamba(lamba < Xline),1);% Identifies the row number for the
% center of the peak Xline
for i = 1:Reps
    figure(1);
    dX = 30; % plot range
    plot(lamba(nX-dX:nX+dX,1), spectra(nX-dX:nX+dX,i),'-or', ...
        lamba(nX,1),spectra(nX,i),'xb'); %Plots the peak of interest using
    % plus or minus dX points on either side of nX
    xlabel('Wavelength');
    ylabel('Counts');
    legend('Select WHOLE Peak');
    grid on
    [j,k] = ginput(2); % Stores x, y coordinates from the GUI
    Xstart(i,1) = size(lamba(lamba < j(1,1)),1); % Identifies row n of
```

```
28      % first click
29
30      Xend(i,1) = size(lamba(lamba < j(2,1)),1); % Identifies row n
            of
31      % second click
32
33      Xarea = trapz(lamba(Xstart(i,1):Xend(i,1),1),...
34          spectra(Xstart(i,1):Xend(i,1),i)); % Calculates area under
                curve
35
36      XPeakWidth = (lamba(Xend(i,1),1)-lamba(Xstart(i,1),1)); %
            Calculate the
37      % peak width in (nm)
38
39      XPeakBackground = (spectra(Xstart(i,1),i)+spectra(Xend(i,1),i)
            )/2;%Find
40      % the average background or baseline for the peak (intensity)
41
42      Xbase = XPeakWidth*XPeakBackground; % Calculate the area of
            background
43
44      correctedXarea(i,1) = (Xarea-Xbase); % Area of just the peak
45
46      Xintensity(i,1) = max(spectra(Xstart(i,1):Xend(i,1),i)); % Max
             intesity
47      % of the peak
48
```

```
49      SBR_X(i,1) = Xintensity(i,1)/XPeakBackground; %Calculate the
            signal to
50      %background ratio
51
52      X_RMS = rms(spectra(Xstart(i,1)-20:Xend(i,1)+20,1)); %
            Calculate RMS
53
54      SNR_X(i,1) = Xarea/(X_RMS*XPeakWidth); % Calculate the Signal
            to noise
55      % ratio
56  end
57  %% Set up output data
58  AreaAndStd(1,1) = mean(correctedXarea); % mean of the area
59  AreaAndStd(1,2) = std(correctedXarea,1);% standard deviation of
        the area
60  AreaAndStd(1,3) = mean(Xintensity); % mean peak max intensity
61  AreaAndStd(1,4) = std(Xintensity,1);% standard D of peak max
        intensity
62  AreaAndStd(1,5) = mean(SBR_X,1);
63  AreaAndStd(1,6) = std(SBR_X,1);
64  AreaAndStd(1,7) = mean(SNR_X,1);
65  AreaAndStd(1,8) = std(SNR_X,1);
66
67  Peakpoints(:,1) = Xstart;
68  Peakpoints(:,2) = Xend;
69
70  close all
```

```
71 end
```

A.4 Calculate Calibration Curves

```
1  %% Imports analysis data and performs calibration statistical
       analysis
2  % Created by Ammon N Williams
3
4  close all; clear all
5
6  %% Load Data
7  addpath('c:/Program Files/MATLAB')
8  set(0,'DefaultAxesFontName', 'Times New Roman')
9  load MSU_Values_386 %Load data file from MSU_Data_Analysis
10
11 %% Setup variables
12 x = [0;0.2015;0.6911;1.3823;2.0735;3.4557;]; % Cncentration of the
       samples
13 y = AreaAndStd_MSU(:,1); % Imports the peak area, if 3, the peak
       intesity
14 AreaStd = AreaAndStd_MSU(:,2); % Imports the peak area std, 4 for
       intensity
15
16 %% Calculate the Regression line and the confidence and prediction
       interval
17 Data(:,1) = x;
18 Data(:,2) = y;
```

```
Data(:,3) = AreaStd;
NewData = sortrows(Data,1); % sorts the data in asending order
x = NewData(:,1); % Setup variables
y = NewData(:,2);
AreaStd1 = NewData(:,3);

xbar = mean(x);
ybar = mean(y);
SSx = sum((x-xbar).^2);
SSy = sum((y-ybar).^2);
Sxybar = sum((x-xbar).*(y-ybar));
m = Sxybar/SSx; % Slope of regression line
b = ybar-m*xbar; % Y-Intercept of regression line
yhat = m*x+b;
R = Sxybar/sqrt(SSx*SSy);
R2 = R^2; % R2 value for goodness of fit
LOD = (3*AreaStd1(2,1))/m; %Limits of Detection
n = size(y,1); % # of data points
Syx = sqrt((sum((y-yhat).^2))/(n-2));
t = tinv(1-.05/2,n-2); % students t value
for i = 1:n % Calculates the Intervals
    % Lower confindence interval
    CIlow(i,1) = yhat(i,1)-t*Syx*sqrt(1/n+(x(i,1)-xbar)^2/SSx);
    % upper confindence interval
    CIhigh(i,1) = yhat(i,1)+t*Syx*sqrt(1/n+(x(i,1)-xbar)^2/SSx);
    % lower prediction interval
    PIlow(i,1) = yhat(i,1)-t*Syx*sqrt(1+1/n+(x(i,1)-xbar)^2/SSx);
```

```
46      % upper prediction interval
47      PIhigh(i,1) = yhat(i,1)+t*Syx*sqrt(1+1/n+(x(i,1)-xbar)^2/SSx);
48  end
49  %% Organize variables
50  RegressionData(1,1) = m;
51  RegressionData(2,1) = b;
52  RegressionData(3,1) = R2;
53  RegressionData(4,1) = LOD;
54
55  %% Plot
56  figure(1);
57  hold on;
58  errorbar(x, y, AreaStd1,'ko');
59  hold on
60  plot(x,yhat,'k',x,CIlow,'k-.',x,PIlow,'k--',x,CIhigh,'k-.',x,
        PIhigh,'k--');
61  axis([-0.25 4 -.005 inf])
62  legend('Data','Regression fit','Confidence interval',...
63      'Prediction interval','Location','NorthWest');
64  legend boxoff
65  xlabel( 'U concentration (wt%)' );
66  ylabel( 'Intensity (a.u.)' );
67  set(gca,'XMinorTick','on','YMinorTick','on','fontsize',18)
68  % print('Uranium_cal387', '-dpng', '-r300');
```

Appendix B

Static Surface LIBS Testing

In the initial phase of the project, several preliminary experiments were done using a static surface configuration in order to gain valuable experience with LIBS in liquids. The static surface approach was used due to its simplicity. In order to mitigate the splashing issue and to eliminate material loss, a horizontal vial approach (similar to the setup used by Wachters and Cremers[19]) was used to study the static surface technique with $CeCl_3$ as a surrogate material.

B.1 Materials and Methods

Samples used in the static surface tests were made using LiCl (99.99%), KCl (99.999%), and $CeCl_3$ (99.99%) mixed into nano-pure water. The LiCl and KCl salts were purchased from Rare Earth Products and the $CeCl_3$ was purchased from Alfa Aesar. The LiCl and KCl salts were mixed into the nano-pure water at the eutectic ratio (44 wt% LiCl, 56 wt% KCl) to form a solution of 20% LiCl-KCl salt by mass. From this base solution, nine standards were prepared with concentrations of Ce ranging from 100 parts per million (ppm) to 10,000 ppm (see Table B.1). Each standard contained 9 mL of solution and was placed in a glass vial that was 25 mm in diameter and oriented on its side so that the depth of solution was 12 mm.

A CFR200 Nd:YAG laser from Big Sky Laser, Inc. was used as the laser source in this study. In this setup, the laser (frequency doubled to 532 nm) was fired downward, through a 2" pierced elliptical mirror (polished aluminum) and focused onto the surface of

Table B.1: Calibration standards showing different Ce concentrations with respect to wt% of $CeCl_3$.

Standard number	Ce concentration (ppm)	wt% $CeCl_3$
1	10,000	1.7587
2	8,000	1.4072
3	6,000	1.0554
4	4,000	0.7035
5	3,000	0.5270
6	1,000	0.1757
7	500	0.0879
8	200	0.0352
9	100	0.0176

the solution contained in the horizontal vial via a 2" quartz lens with a focal length of 60 mm (see Figure B.1 and Figure B.2). Light from the formed plasma was then collected and collimated via the 2" quartz focusing lens. The collimated light was then reflected 90° using the elliptical mirror and through an additional 2" quartz lens with a 100 mm focal length. The light, through this lens, was focused onto a fiber optic cable with a 50 μm core from Andor Technologies. The optical signal was then delivered to an iStar ICCD camera and Mechelle 5000 spectrometer ($\lambda/\Delta\lambda$ of 4,000) from Andor Technologies, and the spectra were collected using the Andor Solis software.

In these experiments, a delay time of 1.5 μs and a gate width of 2 μs were used. The laser energy was approximately 100 mJ. For each sample, ten repetitions were done, each containing 200 laser shots. As a result, 2,000 shots were collected per sample. In this case, the Andor Solis software was set to accumulate the 200 shots yielding a single spectrum per repetition. For the bulk of the experiments, a shot to shot frequency of 2 Hz was used; however, for several of the experiments, a 1 Hz cycle time was used. The ICCD gain was set at 3000 and the temperature was set at -25°C.

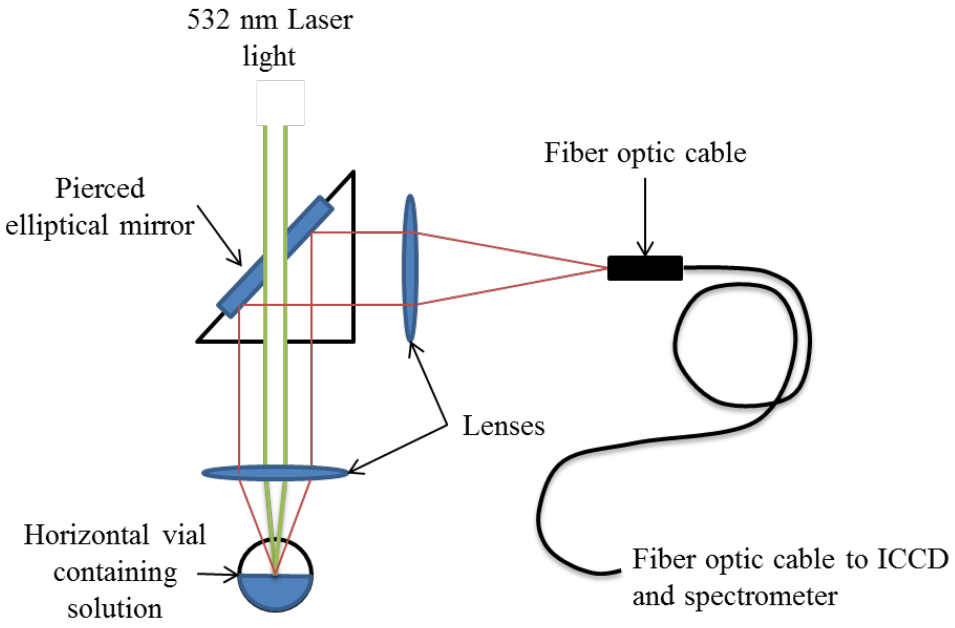

Figure B.1: Representation of the static liquid experimental setup.

B.2 Results and Discussion

The feasibility of using the horizontal vial method was explored as a means to reduce the splashing effect of the material. Here, tests were done using several different vials of the same material (soda-lime-silica glass). The vials containing the sample were stored upright until just prior to LIBS testing. When some of the vials were oriented horizontally, a thin liquid film remained in the region in previous contact with the fluid for a few seconds. In these vials, splashing from the plasma was easily reabsorbed into the film layer. However, for the vials where the film was not maintained, splashing from the plasma formed a droplet on the surface of the glass which distorted and/or obstructed the laser light after only a few shots. A photo showing a typical vial with the different splash regions is illustrated in Figure B.3. It is clear that the film is required in order to provide the ability to take multiple shots of the sample without some other mechanism for removing the droplet formation. Therefore, only vials that demonstrated the film layer were used in the analysis.

A typical spectrum for static surface analysis is shown in Figure B.4. The major elements

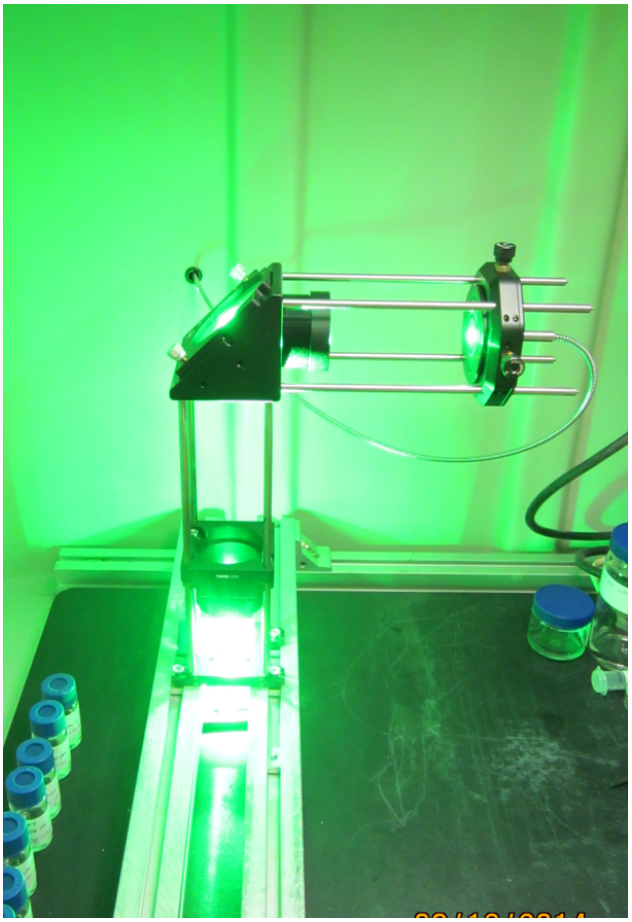

Figure B.2: Experimental setup with the Nd:YAG laser light at 532 nm.

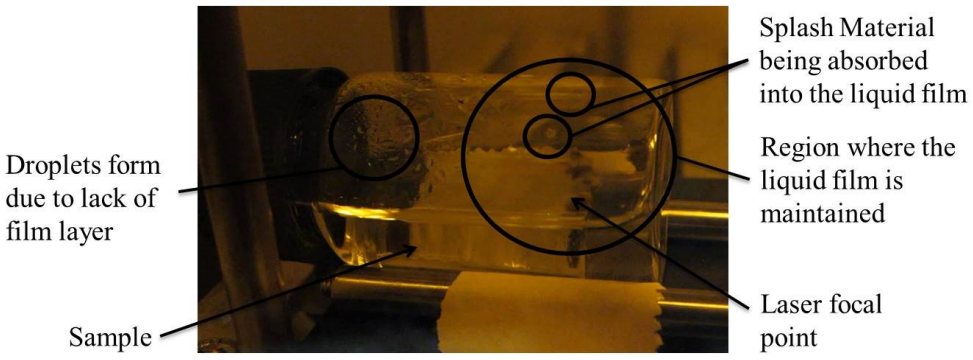

Figure B.3: Photo of a test vial containing the various splashing and film regions.

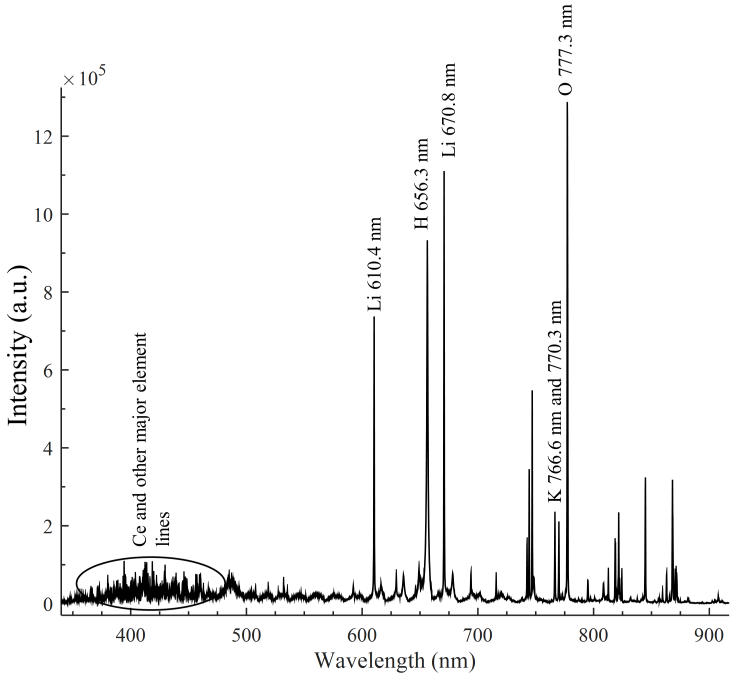

Figure B.4: A typical spectrum for the static surface experiments. The spectrum was generated from the 10,000 ppm Ce standard.

(Li, K, hydrogen (H), and oxygen (O)) can be clearly seen. There are numerous Ce lines that fall between 350 nm and 500 nm which could be used in the LIBS analysis. Peaks were selected that had low interferences and a SBR equal to or greater than 2.5. Five peaks were identified[69] that met the criteria; they are the 413.765 nm, 418.660 nm, 428.999 nm, 446.021 nm, and the 457.228 nm lines. These lines are shown in Figure B.5. The 413.765 nm and 418.660 nm lines are the strongest Ce lines observed in the spectrum. Figure B.6 shows the intensity variation in the region of interest for the 9 samples used. As the Ce concentration decreases, the intensity of the Ce peaks decreases as well.

The %RSD value was calculated between the ten repetitions taken for each sampling concentration. The shot frequency and the number of shots taken per acquisition were varied for the 4,000 ppm Ce standard. The average %RSD between 400 nm and 460 nm was compared for each to identify effects of the parameter. The average %RSD for experiments operating at 2 Hz and 200 shots was 18.5% with lows and highs ranging from 15% to 28%,

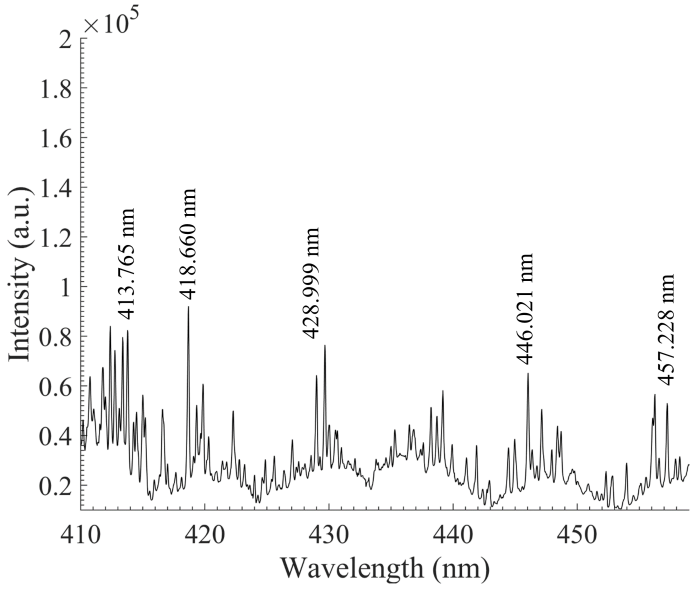

Figure B.5: Region of interest showing the diversity of Ce peaks.

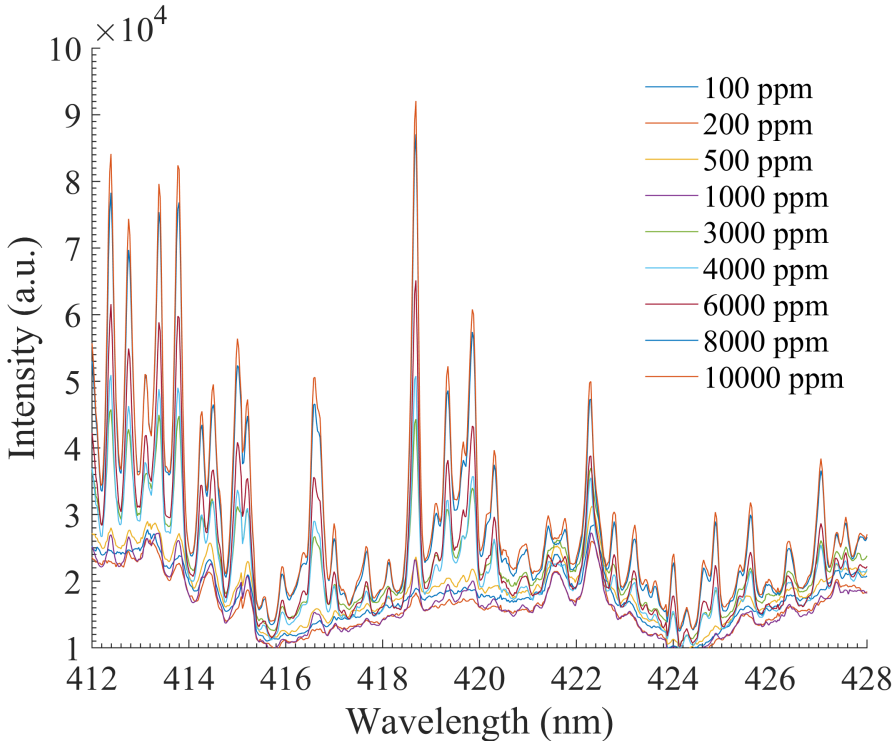

Figure B.6: Spectra showing the variation of the spectral intensity as a function of the concentration.

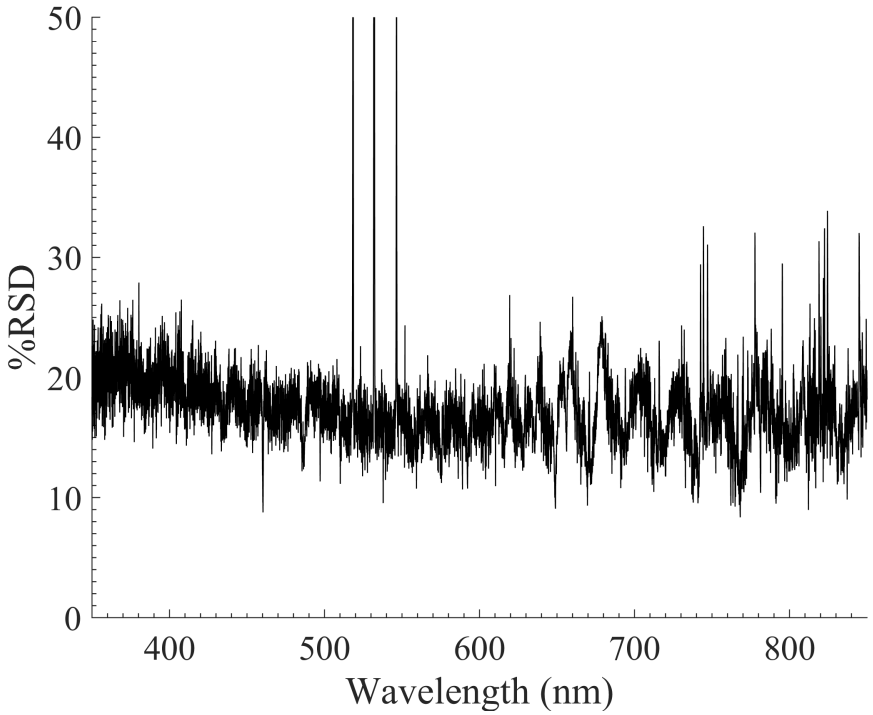

Figure B.7: The %RSD between the 10 spectra for the 4000 ppm sample at 2 Hz and with 200 shots accumulated.

respectively (see Figure B.7). Under these conditions, fluctuations in the %RSD's typically ranged between ±5%; however, spikes to higher levels were occasionally observed. At 1 Hz and 200 shots the average %RSD was calculated to be 14.6% with lows and highs ranging from 12% to 18%, respectively. The %RSD for the 2 Hz case at 500 shots was calculated to be 14.4% with lows and highs ranging from 11% to 18%, respectively. From these experiments, the slower (1 Hz) shot-to-shot frequency was better—as would be expected due to the surface perturbations created by the laser shockwave. In this system, there would be a lower limit on the shot-to-shot frequency in order to maintain the liquid film on the top surface of the vial; however, the lower limits were not explored in this study. The larger number of laser shots also yielded a better %RSD as expected. It is anticipated that combining the lower shot-to-shot frequency with more shots would further improve the repeatability of the LIBS analysis. Due to application constraints not discussed here, the acquisition parameters of 2 Hz frequency and 200 shots were used in the remainder of the static study.

Table B.2: Linear fit coefficients, goodness of fit, and the limits of detection (LOD) for the different calibration curves

Line (nm)	R^2	b_1	b_0	LOD (ppm)
413.765	0.991	0.7848	795.80	967
418.660	0.985	1.2377	407.22	403
428.999	0.986	0.6373	176.53	608
446.021	0.991	0.7404	554.58	816
457.228	0.991	0.5952	124.57	442

Spectra were collected for the nine standards as previously outlined in Table B.1. Once the spectra had been generated, the area under the peak of interest was calculated using a program written in the commercial software MATLAB. Here, a graphical user interface (GUI) was used to select the peak range and the area under the curve was calculated using a numerical integration technique. This process was done for each repetition of the sample. An average of the peak areas for the line of interest was then calculated for each standard, yielding a single point on the calibration curve. Figure B.8 shows the calibration curves for the different Ce peaks selected. For all of the selected peaks, the regression lines fit the data well with R^2 values ranging from 0.98 to 0.99. The peak areas for the 10,000 ppm standard were lower than the rest of the linear trend. This was not specific to the Ce lines only; in general, the spectra generated from this standard are slightly lower. A normalization of the curves with a Li peak does create a more linear trend but also introduces larger errors due to the large standard deviation of the Li peak. The calibration curves were fit using MATLAB. The coefficients to the linear fit and the R^2 for all of the calibration curves are shown in Table B.2.

The LOD for the different lines were calculated and the results are shown in Table B.2. All of the detection limits are larger than the two to three lowest standards; this is a result of relatively large standard deviations in the peak area at lower Ce concentrations. In other words, with the current setup (laser, spectrometer, configuration, and acquisition parameters), the variations in the spectrum are larger than the peaks themselves. The 418.660 nm peak provided the best LOD of 403 ppm and the 413.765 nm peak provided the worst

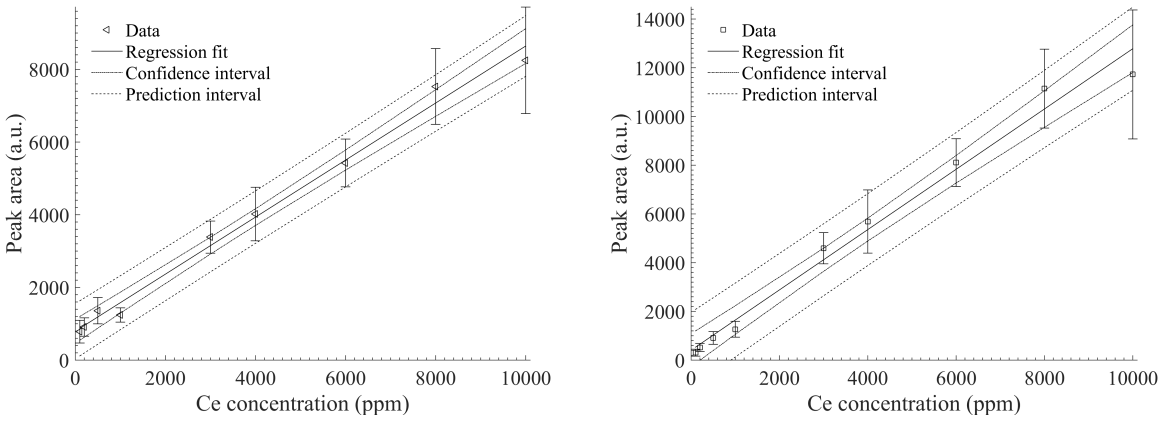

(a)

(b)

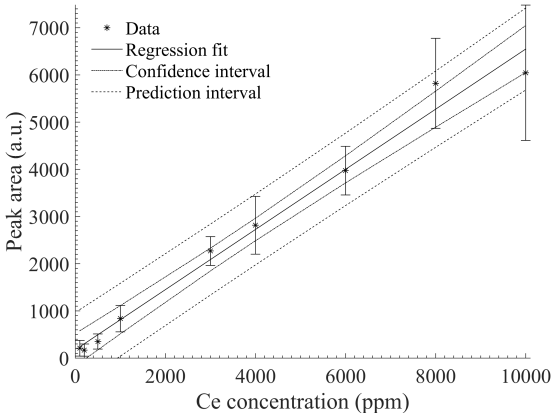

(c)

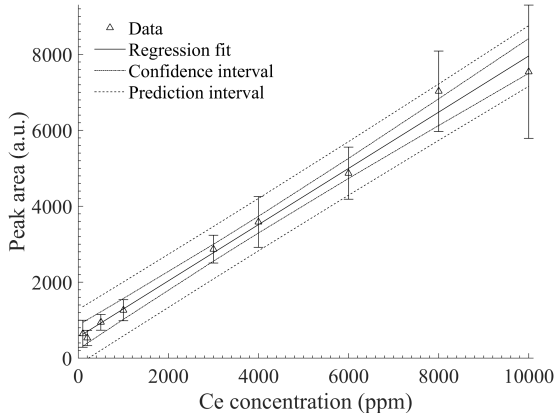

(d)

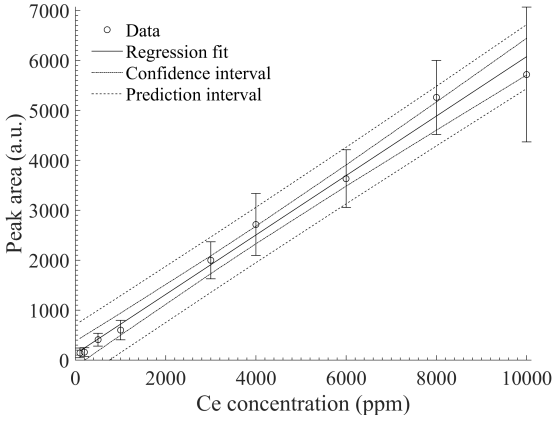

(e)

Figure B.8: Calibration curves for the Static liquid setup. (a) Curve from Ce 413.765 nm peak, (b) curve from the Ce 418.660 nm peak, (c) curve from the 428.999 nm peak, (d) curve from the 446.021 nm peak, and (e) curve from the 457.028 nm peak.

LOD at 967 ppm. Based on the calibration curves and the LOD, the 418.660 nm line is recommended for use in this system.

B.3 Conclusion

The detection of Ce was demonstrated via LIBS in a static liquid configuration. The %RSD for the static liquid configuration averaged around 18.5%. This relatively high value is a result of the splashing effects on the vial surfaces used and fluctuations in laser energy. Calibration curves were generated for the static liquid case and R^2 values ranged from 0.98 to 0.99. Of the different Ce lines explored, the 418.660 nm peak had the best LOD of 403 ppm.

This study has demonstrated the LIBS capability to measure Ce in a liquid using the static surface approach without loss of material. The %RSDs were high as stated above, more shots and a slower repetition rate could improve this. However, this technique would be extremely difficult to implement for a molten salt because it is anticipated that the splashed salt, if it formed a film, would also quickly etch the surface of the glass/quartz and thus reduce the signal over time.

Appendix C

Magnetic Pump

Due to the extreme operating conditions and safety constraints of this project, conventional pumping mechanisms are not sufficient. Traditional mechanical pumps (gear, vane, diaphragm) will not work well with this project due to temperature as well as decontamination between experimental samples. Gravity fed flow is a possibility, however, in LIBS multiple shots (50-1000) must be made for every sample. As a result, the time required to acquire the spectral data may be too long for measurement via this method. Another possibility is using electromagnetic (EM) pumps. Two main types of EM pumps exist, they are: conductive and induction type pumps.

In an conductive EM pump, electrodes are used to create a current in the conductive liquid in a channel. Perpendicular to the electric current, a magnetic field is supplied. The combined electric and magnetic fields create a force, called the Lorentz force, that directs the flow down the channel. This type of pump is effective at pumping any electrically conducting fluid. However, this type of pump is not ideal for the current application due to the use of electrodes in the design. In other words, fission product and uranium ions present in the fluid flow could be reduced at the cathode while chlorine gas is oxidized at the anode. Selection of an operating voltage sufficient to drive the fluid without a significant reactions presents a large challenge outside the scope of the current project.

Induction type EM pumps use the idea of a traveling magnetic wave. Typically induction pumps use 3 phase AC current to induce a magnetic field. Due to the nature of 3 phase current and the stator windings, the magnetic field as felt by the ionic liquid is traveling with alternating magnetic poles. This alternating magnetic field creates eddy currents in the

ionic liquid. The combined effect of the moving magnetic field and induced eddy currents is the Lorentz force that then pumps the fluid. This style of pump is convenient with working with uranium because the channel is the only portion of the pump exposed. Several high temperature induction EM pumps are commercially available; however, the available sizes are much greater than required by the current application. The high temperature application provides a challenge for insulating the windings in the pump. Also, the nature of the 3 phase windings makes this pump a challenge to custom build a small EM pump for the application. As a result, a more innovative EM pump design is needed.

One such design is an induction EM pump using rotating permanent magnets[93–101]. In this design, permanent magnets of alternating polarity are located on a spindle or rotor as shown in Figure C.1. The fluid is in a channel adjacent to the rotating magnetic field. The alternating traveling magnetic field induces eddy currents, and via the Lorentz force, the fluid is pumped through the channel. The advantage of this EM pump design is that it is relatively easy to build and operate. As a result, an EM pump based on permanent rotating magnets was selected to drive the molten salt in the loop. Several types of permanent magnet pumps have been explored in the literature including the rotor[95, 102, 103], disc[98], and centrifugal[94] designs. The rotor-style EM pump is the most common, however, the efficiency of disc-type design is greater because of the stronger magnetic flux due to magnets on the opposing disc[93]. The disadvantage of disc-type pumps is structural strength at high flow rates. For this application, only low flow rates are required and thus, the disc-type permanent magnet EM pump was selected for the design.

C.1 EM Pump Design Equations

Several design equations have been identified in the literature to provide insight on the design of a permanent magnet EM pump for the current application. To design a pump, it is important to understand the relationship between the pressure and flow generated by the

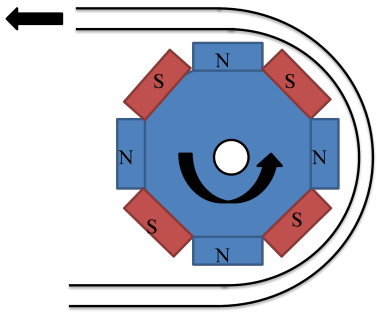

Figure C.1: Schematic representing the rotor style permanent magnet EM pump.

pump. The maximum pressure developed by the pump can be expressed by[93, 95]:

$$P_{max} = 0.5\sigma B^2 V_B l_{ch} s k \tag{C.1}$$

$$V_B = 2\pi R n \tag{C.2}$$

$$s = 1 - \frac{V_m}{V_B} \tag{C.3}$$

where, σ is the electrical conductivity of the fluid, B is the average magnetic field in the channel, V_B is the velocity of the traveling magnetic field, l_{ch} is the active length of the channel, s is the slip, k is a coefficient accounting for pressure drop due to the transversal end effect, R is the mean radius of the channel, n is the rotation speed, and V_m is the velocity of the liquid in the channel. Eqns. C.1, C.2, and C.3 appear to correlate very well with experimental data[93, 95]. With these equations, the parameters B, R, and l_{ch}, can be adjusted to achieve the desired pressure flow rate relationship for a given n. As the rotation speed n, increases, the amount of pressure generated by the pump increases. Therefore, for a given pump design, varying flow rates can be achieved simply by adjusting the rotation speed.

Another key aspect of designing a permanent magnet EM pump is selecting the appropriate motor. To do this, it is essential to understand the losses in the pump. The losses

due to induced eddy currents in the fluid is given by[93, 95]:

$$W_f = 0.5\sigma(BV_B s)^2 k L_{ch} 2ab \tag{C.4}$$

where, $2a$ is the width of the channel and b is its thickness. Losses are also generated in the channel walls if the wall material is electrically conductive. Under these circumstances the losses are given by:

$$W_w = 0.5\sigma_w(BV_B)^2 k L_{ch} 2a 2\delta_w \tag{C.5}$$

where σ_w is the electrical conductivity of the wall material and δ_w is the thickness of the wall. The total energy required to drive the pump is given by:

$$W = W_f + W_w + PQ + W_0 \tag{C.6}$$

where P is the pressure, Q is the flow rate (PQ is the hydraulic energy of flow), and W_0 is the energy required to drive the free rotor without load.

C.2 Pump Design

For the LIBS study on flowing molten salt, it is desired to be capable of pumping the fluid at a flow rate of at least 1 L/min. Using Eqns. C.1, C.2, and C.3, pump parameters have been identified and are shown in Table C.1. At the aforementioned flow rate and selected parameters, with a disc rotation at 4,800 RPM, the maximum pressure generated by the pump in 100 Pa. This is enough to overcome the pressure losses generated by flow through the remaining molten salt loop. Using Eqns. C.4, C.5, and C.6, the required motor size must be greater than 1.0 W. Since the pump magnets are to see very high temperatures, special magnetic materials are required to prevent de-magnetization. A SmCo magnet has been identified from Electron Energy Corporation that can be operated up to 500°C. The size of magnet was selected to be 1.25 in x 0.6 in x 0.4 in. The direction of magnetism is through

Table C.1: Physical parameters of the designed EM pump.

Parameter	Value	Unit
R	0.07	m
l_{ch}	0.33	m
$2a$	0.0235	m
b	0.004	m
δ_w	0.001	m

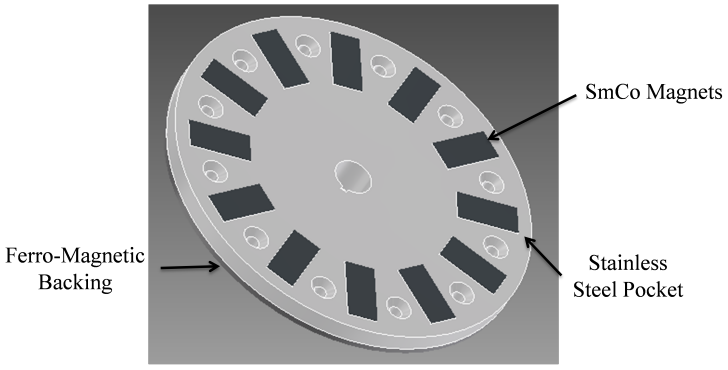

Figure C.2: 3D rendering of the disc with magnets.

the 0.4 in dimension. At 500°C the residual induction (Br) of the magnet is 0.68 T. At this strength, the flux in the center of the channel is estimated to be approximately 0.35 T.

Having established the basic dimensions and magnetic parameters, the disc and channel was designed. At the maximum operating RPM of the pump, a significant amount of centrifugal force is present on the magnets. To sufficiently secure the magnets, a design using a ferro-magnetic backing with a stainless steel (SS) pocket was designed as shown in Figure C.2. The SS pocket and the ferro-magnetic backing material will be fastened together using 0.25 in screws. Finite element analysis (FEA) was done on the disc to simulate the forces and stresses on the disk as a result of the high rotation speed. Autodesk Inventor was used in the design and FEA analysis. The design is sufficient to withstand all applied forces.

C.3 Prototype 1

The molten salt loop is made of 0.5 inch stainless steel tubing, connected with Swagelok fittings, and has a total volume of approximately 100 mL. This volume corresponds to roughly 140 g of the LiCl-KCl salt at 500°C. Since the salt is solid at room temperature, a method is needed to add the solid salt into the loop before melting. To accomplish this, a stainless steel funnel was purchased and fitted into the loop via a 90° elbow. The funnel will hold approximately 80 mL, therefore, the salt will need to be added in two melting stages.

In the original design, the drain port was located directly underneath the fill port, however, this was changed to a point on the extreme edge of the loop. This change will allow for easier drainage of the loop by tipping it such that the drain port will be at the lowest point in the loop. This prevents potential pooling of the liquid within the loop. The drain port is a 0.25 tubing adaptor that has been welded into the main loop to create a T. A Swagelok 0.25 needle valve has been positioned on the tubing adaptor and will be used to control drain flow.

Another addition to the loop is pressure ports just before and after the loop passes through the pump region. These ports are 0.125 inch tube adaptors that have been welded into the main loop. From these ports, Swagelok union fittings will be used to connect a Dwyer Series 2000-250PA differential pressure gauge. This feature will be used to measure the pressure head generated by the pump as well as provide information on the flow rates of the molten salt.

Due to the unique shape and design of the molten salt loop and electromagnet pump, it was not feasible to use a traditional induction type tube or box furnace. As a result, heating tape and temperature controller made by BriskHeat were employed. The heating tape that will be used is 1 inch wide by 48 inch long with a 13.1 W/in^2 heating capacity and is capable of temperatures up to 600°C. At 627 total Watts generated by the tape, the salt within the loop should easily be melted and maintained at 500°C. The temperature

controller is digital and can be programmed with set points and safety shutoff temperatures in an over-temperature scenario. To prevent burns and excessive heat loss from the molten salt loop and pump, 3 inch aluminosilicate insulation board was shaped around all heated features.

A motor was selected to meet acceleration and load requirements for the rotating discs and pump. Based on the pump design equations outlined in a previous report, the amount of power required to pump the salt was calculated to be approximately 1 W. This is rather small, as a result, the load required to accelerate the disc and to maintain angular momentum was the basis for motor selection. The disc have a moment of inertia (J) of approximately 330 kg/cm^2. With an acceleration of the disc form zero RPMs up to 5,000 RPMs in a reasonable amount of time equates to a torque of 1.1 N m. In addition, the power supply available in the lab is only 120 V at 20 A. Based on the torque and power criteria, a motor made by Teknic was selected. It is a M-3421 motor with a continuous torque rating of 2 N m. This motor comes complete with an encoder, power source, and operating software.

In addition to the motor, bearings to support the shaft and discs of the pump were needed. The radial load on the bearings iwas small due to the vertical configuration used. The axial load on the bearing was also small due to the relative mass of the components involved. The real challenge involved in selecting a bearing was the high temperatures involved. Special materials are required for bearings operating at 500°C, however, these materials wear quickly (graphite), or are ceramic and are prone to impact failure. Eventually, a bearing was selected from A.M.I. Bearing that is stainless steel and capable of handling temperatures up to 240°C. This selection allowed for a strong impact resistant bearing (safe), however, it may require additional cooling be provided to the shaft between the heating zone and the bearing. If needed, cooling will be provide by way of forced convection over the shaft via compressed argon. Provision for this cooling mechanism was built into the pump housing via stainless steel tubing.

The disc used to house the rare earth magnets are composed of three layers. The

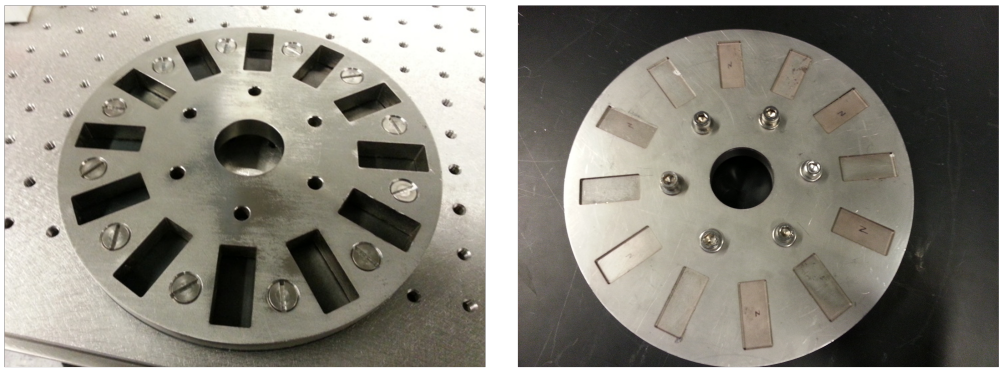

Figure C.3: (a) Photo of the support plate with attached backing. (b) Photo of the completed disc with magnets.

first layer is a mild steel backing which allows for a surface for the magnets to adhere. The second layer is a 0.5 stainless steel (non−magnetic)plate with pockets cut to hold the magnets in place. The last layer is a stainless steel plate that is 0.06 thick. The disc are shown in Figure C.3 This plate also has notches, or openings that are smaller than the magnets themselves. This prevents the magnets from being thrown from the disc without covering and shielding them. The magnets shown in the disc were placed with alternating polarity.

Following the assembly of the discs, the disc were positioned on the shaft and installed in the pump housing as shown in Figure C.4. Here, the molten salt loop channel has been positioned such that it is equidistant from the disc surfaces so that no portion is in contact with the disc.

The finished EM pump is shown in Figure C.5. Initial testing of the loop with a molten salt showed a major weakness to the design. Due to the horizontal nature of the design the loop could not easily be filled or drained. As a result, the capability of the pump was not verified.

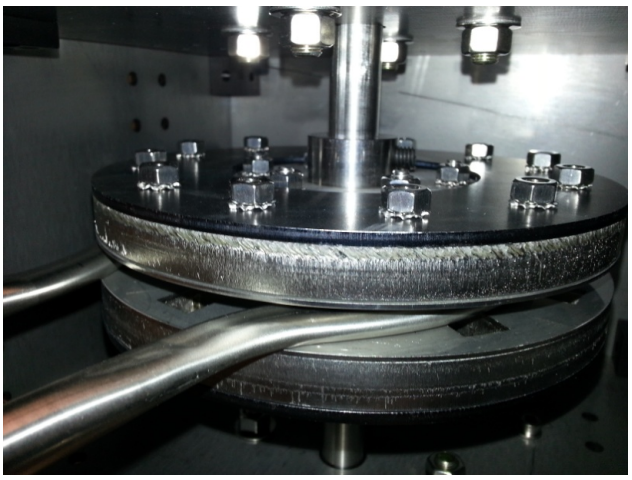

Figure C.4: Close up of the disc positioned around the molten salt loop channel.

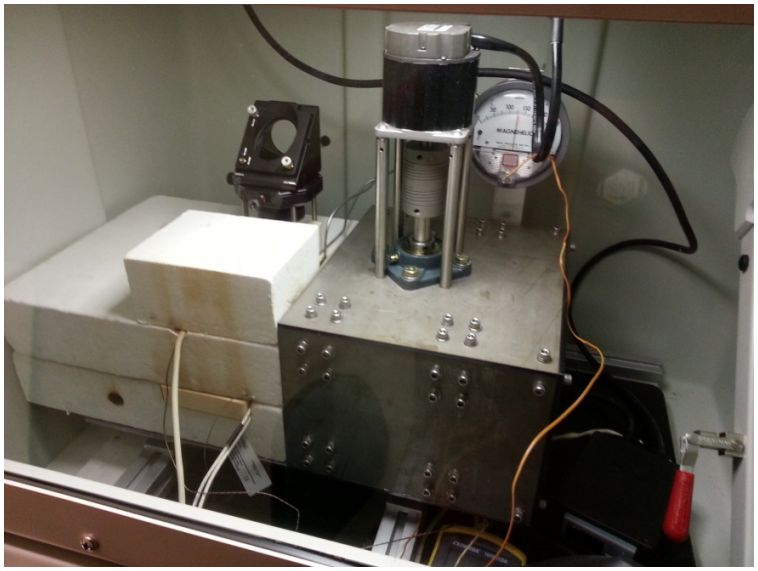

Figure C.5: Experimental apparatus complete with insulation.

C.4 Prototype 2

From the shakedown tests conducted to date using prototype 1, it was apparent that certain modifications were necessary to provide a better operating EM pump. Therefore, a second prototype (P2) molten salt loop was designed to aid in: (1) filling and draining the loop, (2) melting the salt, and (3) sealing the loop to force closed loop operation. The new loop was oriented vertically allowing gravity to aid in filling and draining the loop. Here, the fill port at the top of the loop can be sealed during operation using a Swagelok end cap. The drain valve is located at the lowest point in the loop, this allows for easy drainage of the loop. Another feature is the pressure measuring ports. The location of the ports is the same in P2 as in the previous design; however, now the ports have 1/4 tubing risers to prevent potential leakage close to the heating tape. The 1/4 inch risers are connected to 1/8 inch tubing which leads to the differential pressure gauge. This design also allows for a greater volume of gas to exist in the lines, while reducing the likeliness of capillary forces drawing salt far up the tubing. The risers as well as the 1/4 inch tubing connecting the drain valve have been welded into the main loop. The remaining fittings are Swagelok type compression fittings.

Several water tests were done to verify filling and draining procedures as well as to quantify the loop volume. For this, 100 ml of water was measured out and then a portion was used to fill the loop to capacity, the remaining water was measured to quantify the amount in the loop. For the first test 86 mL of water was used to fill the loop. Next, the drain capability was tested. The drain valve was opened and greater than 85 ml of the water was recovered. Several tests were run in this way and an average of 86 mL filled the loop. The density of the LiCl-KCl salt at 500°C is 1.62 g/cm^2; therefore, 139.3 grams of salt are needed to fill the loop.

With this design, additional heating was provided in the lower pump region. Here, the 3 inch insulation has been added to the apparatus along with a 6 ft by 1 inch heating tape

made by Briskheat. This heating tape delivers up to 615 W of energy. The heating tape was positioned around the loop such that approximately 4 ft of the loop was coiled around the EM pump disc to provide heating to the lower region of the loop, which had previously been a cold spot. The remaining 2 ft heat tape was wrapped around the upper portion of the molten salt loop. A test was done in the fume hood to test the heating capabilities of the new furnace design as well as to bake out the new insulation used in the design. During the test, the furnace was slowly ramped up to 500°C. Temperatures at the top of the loop, bottom of the loop, and at the shaft bearing interface were measured and recorded. Maximum observed temperatures were 535°C, 470°C, and 105°C for the upper portion, lower portion, and shaft bearing, respectively. The large temperature gradient between the top and bottom portion of the loops can be contributed to point of contact of the thermocouple. For the upper portion measurement, the thermocouple was in direct contact with the stainless steel loop. For the lower portion measurement, the thermocouple was positioned in air between the discs, close to the loop.

In the next phase, the apparatus was installed into the glove box as shown in Figure C.6. As previously mentioned, the apparatus was mounted vertically. The first test involving actual salt was conducted. Here, the salt beads were added prior to heating as before. However, only about half the beads could be added in this way due to geometric and physical constraints (this was expected). The furnace was then allowed to heat up slowly (approximately 4 hours) to prevent large thermal gradients within the furnace. During this time, the glovebox was continually being purged to remove any oxygen that may be released from the insulation during heating. Once the furnace was set to 500°C, the remainder of the salt was added via a funnel and stainless steel scoop. This procedure proved very effective and all 139.3 grams of salt were added. Once the salt was added, the system was left for 2 hours to come to a steady state temperature. Again, temperatures in/around the loop were 530°C, 480°C, and 140°C for the upper loop portion, lower loop section, and 2" above the furnace near the fill port, respectively.

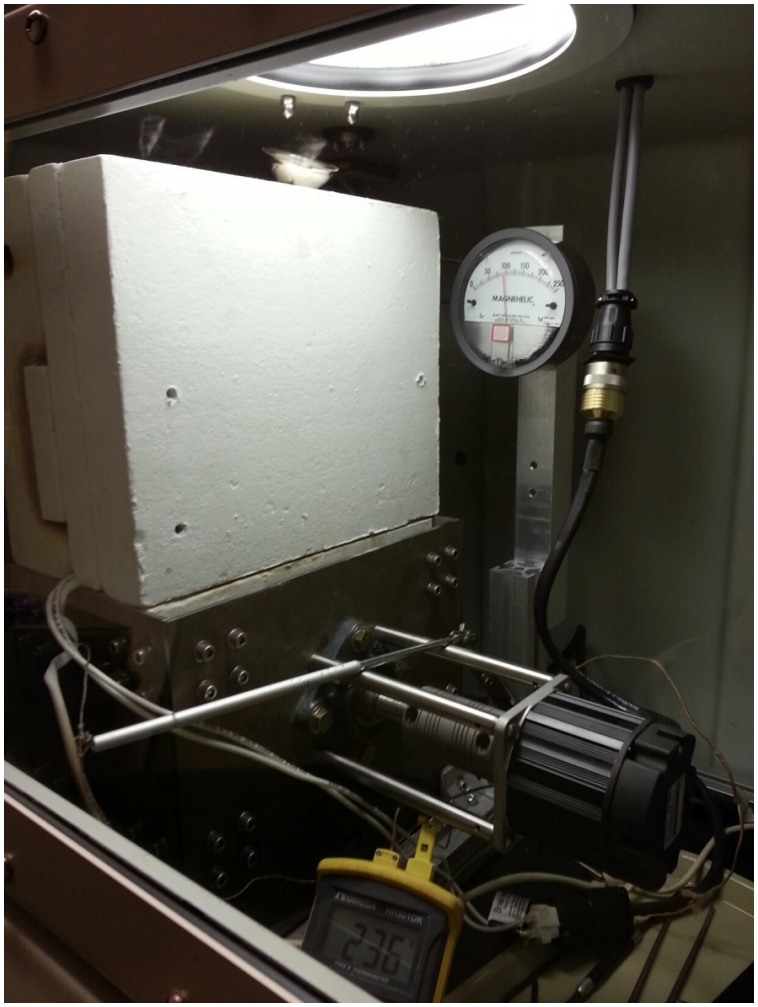

Figure C.6: Pump apparatus installed in the inert atmosphere glove box.

With the furnace operating at 500°C and the loop filled completely with salt, it was possible to test the EM pump capabilities. With the disc RPM set to zero, the differential pressure gauge was zeroed. The RPM was then set at 500 RPM and no change was observed in the pressure. The same result was observed for the 1,000 RPM, 1,500 RPM, 2,000 RPM, 2,500 RPM, and 3,000 RPM. Several potential reasons exist for this observed result. First, the magnets were de-magnetized due to temperature. This is highly unlikely due to their extremely high curie temperature at 500°C. Upon system cooling the magnetic strength of the magnets was verified using a Guassmeter, the magnets maintained their full original strength. Second, a failure in the measuring technique prevented an accurate reading of the flow within the loop. After system cool down a small amount of salt residue was discovered around the 1/8 inch Swagelok fitting on both pressure risers. This means that gas and salt escaped through at least these fittings, this could potentially skew results. This alone should not account for a zero response at the pressure gauge; however, being that salt was present this high up the riser suggest that salt rose as a result of compression of the gases in the lines and potential leaking of the risers. If allowed to rise sufficiently high to leave the heated area, it could reach the melting temperature and plug the tubing. If this occurred, regardless of the pressure differential and flow in the loop nothing would register at the gauge. Lastly, the magnetic flux or electrical conductivity of the salt is not sufficient to provide a strong enough Lorentz force for pumping to occur.

C.4.1 Molten Salt Flow —Problems and Solutions

It was thought that the molten salt shakedown experiment failed for what appeared to be capillary action and/or freezing in the pressure measurement risers coming from the main salt loop. For the next shakedown test, the 0.125 inch lines were replaced with larger 0.25 inch lines to mitigate this issue.

The first experiment conducted using the new EM pump riser design was done using pure LiCl-KCl eutectic salt. As before, the salt beads were loaded into the top portion of

the furnace at temperature until the loop was full—requiring approximately 139 g of salt at 500°C. With the loop fully loaded, and the furnace up to temperature, the EM pump capabilities were tested. At 200 RPM, there was no observed change in the pressure differential, indicating no flow or pressure gradient of any kind. The same result was observed for speeds all up to 3,000 RPM. Following the experiment, no observations were made indicating failure due to the risers.

Several possible theories exist for pump failure: (1) the pressure measuring system is not functioning correctly, (2) the electrical conductivity of the salt is too low, or (3) the Lorentz force acting on the positive ions (Li^+ and K^+) is being canceled by the forces acting on the negative ions (Cl^-). The last theory was the easiest to test. For the next experiment, a LiCl-KCl-$CeCl_3$ (10wt% $CeCl_3$) salt was used. The Ce^{+3} ion has a greater charge and would therefore, be more strongly influenced by the Lorenz force than the Cl^- ion. The experiment was prepared and conducted with similar results observed as before; that is, there was no pressure gradient generated in the molten ternary salt mixture.

C.5 Molten Tin Test

To test the other two EM pump failure theories, an additional material must be used to test the pump. Molten metals have been shown to have sufficient electrical conductivities to be pumped using design configurations similar to the one used in this study[93]. Here the objective was to test the EM pump using molten tin to verify the EM pump and pressure measuring system. Tin was selected due to its low melting point (231.9 °C), low toxicity, and high electrical conductivity.

To ensure complete melting of the tin, a temperature of 400°C was selected as the operating temperature for these experiments. At 400°C, the density (ρ), viscosity (ν), and electrical conductivity (σ) are 6.834×10^3 kg/m^3, 1.3×10^{-3} kg m/s, and 1.945×10^4 ohm^{-1} cm^{-1}, respectively. (Note: σ for molten LiCl-KCl at 500°C is 1.854 ohm^{-1} cm^{-1}). Based on

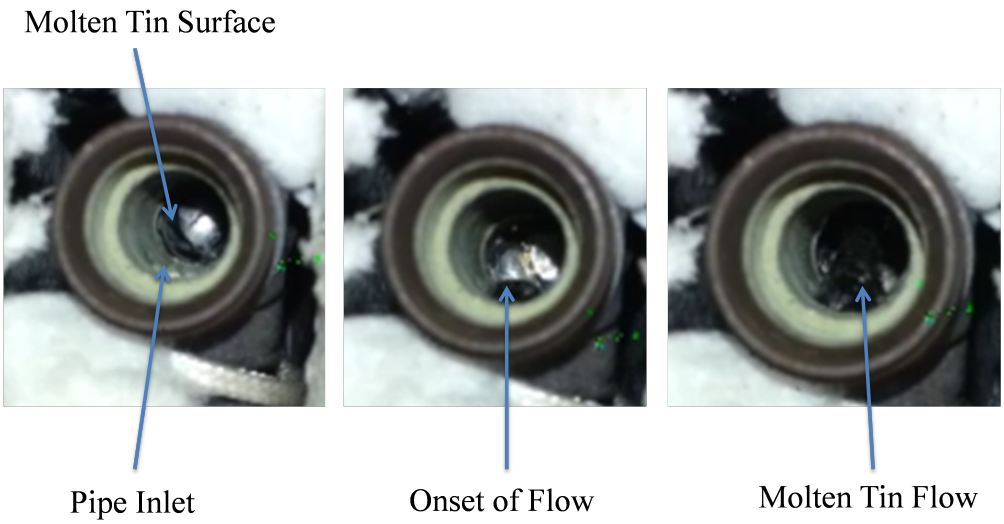

Figure C.7: Photos extracted from a video taken at the onset of molten metal flow in the electromagnetic pump.

previous experiments, 86 mL of material is needed to fill the loop, thus 587.7 g of tin were required.

C.5.1 Experiment 1

The EM pump was positioned in the fume hood in the Radiochemistry Laboratory in the VCU West Hall. Here, the loop was loaded with tin as done previously. The temperature was ramped to 400°C, at this point; the surface of the molten tin could be seen near the top of the fill port. However, the liquid level was low and the system had not yet closed, in other words, the upper portion of the loop was still dry. When the pump motor was engaged slightly, the liquid level on the high pressure side of the loop was observed to increase. As the motor speeds (in RPM) were increased, the liquid level continued to increase until it reached the top of the loop and spilled over into the low pressure portion of the loop. Photos extracted from a video of the observed flow are shown in Figure C.7. At this point, an additional 6 g of tin were added to ensure the loop was properly filled. By observation, it is clear that flow is occurring within the loop, such flow was never observed for the molten salt system.

In addition to the observed flow, pressure readings were measured as a function of the motor RPM. Here, motor RPM was rapidly taken from zero to the end RPM in a single step. A pressure data collected from the first experimental run is shown in Figure C.8. It can be seen that as the motor RPM increased, the measured pressure differential also increased. From the pressure differential, the average velocity (v), flow rate (Q), and Reynolds (Re) number can be calculated using the following equations:

$$v = \frac{\Delta p D^2}{32 \mu l} \tag{C.7}$$

$$Q = \frac{\pi D^4 \Delta p}{128 \mu l} \tag{C.8}$$

$$Re = \frac{\rho v D}{\mu} \tag{C.9}$$

where Δp, D, and l are the differential pressure, tube diameter, and tube length, respectively. Eqns. C.7 and C.8 are derived under the assumption that the flow is fully laminar. Calculated values for the velocity, flow rate and Reynolds numbers are shown in Table C.2. Interestingly, values of the Re number indicate that much of the flow is not in the laminar flow regime (Re $\leq$ 2100), but in the transitional regime (2100 $<$ Re $<$ 4000) and turbulent regime (Re $\geq$ 4000). As a result, Eqns. C.7 and C.8 can only be used as an approximation of the flow characteristics of the metal within the loop.

When attempting to operate at the motor at 1035 RPM during this first experiment, a large noise was observed and the pressure spiked up to 150 Pa and then slowly and continuously climbed. At zero RPM the pressure did not return to zero but remained at approximately 65 Pa. The fill port cap was removed and it was observed that the liquid level in the loop had dropped approximately 2 cm, suggesting that molten metal had been forced up the pressure risers. The pressure still responded, albeit, slower, so the assumption was made that the risers were not blocked.

To account for the drop in material, 41.5 g of tin were added to the loop to ensure the loop

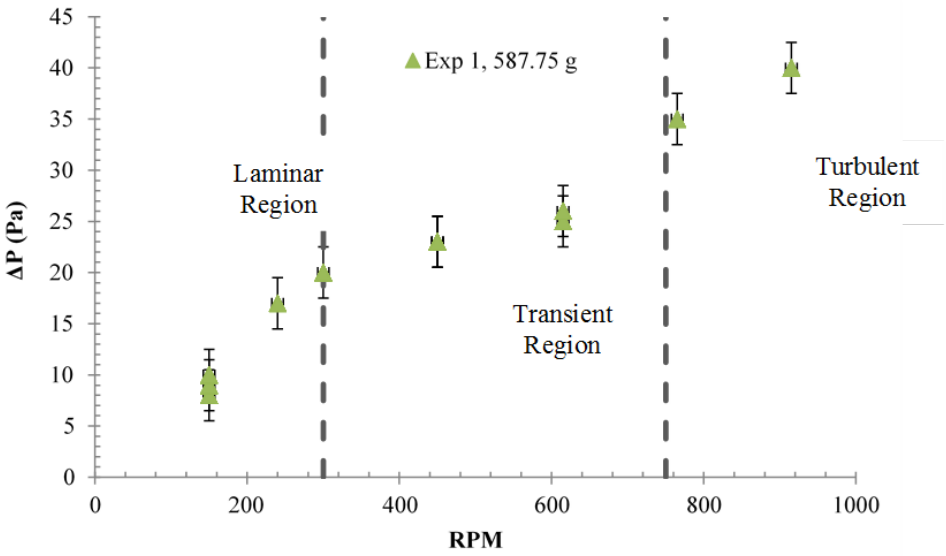

Figure C.8: Pressure curve for experiment 1. For motor speeds up to approximately 300 RPM the flow in the loop is laminar. Between 300 and 750 RPM the flow is in the transitional regime. For motor speeds the above 750 RPM the flow is within the turbulent regime.

Table C.2: Calculated values of the velocity, flow rate, and Reynolds number for Exp. 1.

RPM	ΔP (Pa)	v (cm/s)	Q (cm^3/s)	Re
150	8	1.67	1.56	902
150	9	1.88	1.76	1015
150	10	2.08	1.95	1127
240	17	3.54	3.32	1916
300	20	4.17	3.90	2255
450	23	4.79	4.49	2593
450	23	4.79	4.49	2593
450	23	4.79	4.49	2593
615	25	5.21	4.88	2818
615	26	5.42	5.08	2931
765	35	7.30	6.83	3945
915	40	8.34	7.81	4509

was completely filled. Several pumping runs were conducted but the data was not consistent and the response time was quite slow. At this point, the pressure gauge was removed from the risers and solid tin was observed in the fitting leading into the pressure gauge as well as within the gauge itself. During the first experiment, when attempting to reach 1035 RPM material must have been thrown up into the risers due to a large impulse in the fluid created by the rapid acceleration of the motor.

The observed material was easily removed from the fitting and gauge; however, the riser tube itself was blocked with an unknown amount of material. Since material had been added to the main loop, there would not be room for the metal volume in the risers to drain properly; therefore, 105.5 g of tin were drained from the main loop via the drain port. The risers were drained by tipping the furnace (now at room temp) on its side and heating the risers using a heating tape on hand. The heat tape was operated at 400°C for 20 minutes. Once the riser had cooled, a thermocouple was inserted into the riser down into the loop region, verifying that the blockage had been removed. At this point, approximately 525 g of tin was in the loop.

C.5.2 Experiment 2

For this experiment, no new metal was added into the loop. The goal was to measure the pressure gradient induced by the pump under no flow conditions. Motor control for this experiment was done using Quickset software via a %offset function. To prevent an impulse as described previously, motor RPM was ramped in 1 %offset intervals (30 RPM). Data collected in this experiment is shown in Figure C.9. Here, as the RPM increased, the liquid level in the high pressure side increased with pressure. However, for the data greater than 210 RPM, the liquid level had risen far enough that it was spilling over into the low pressure side of the loop. When speed were greater than 270 RPM, air was being introduced into the loop creating a sucking sound due to the low liquid level. As a result, no data was collected at speeds greater than 270 due to inconsistencies introduced by air introduction to

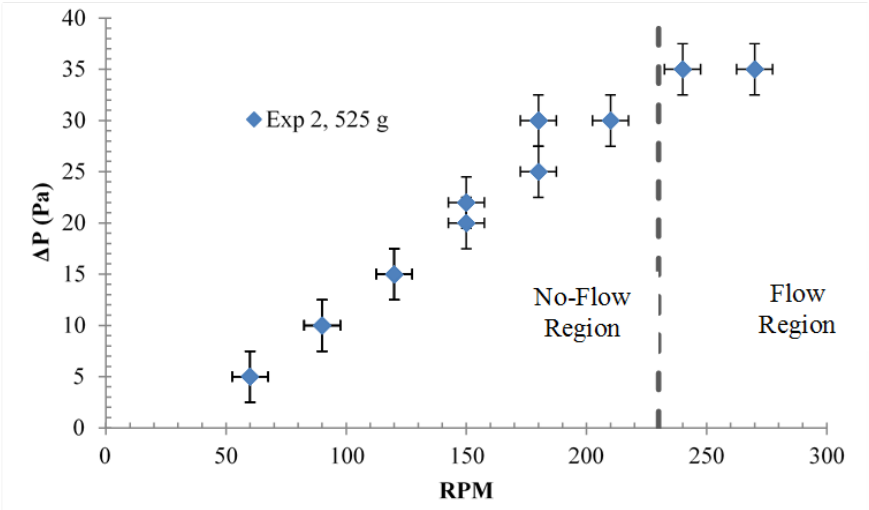

Figure C.9: Pressure curve for experiment 2. In the initial linear portion no flow occurred; however, liquid metal levels were high enough in the last two points for material to spill over into the low pressure side.

the pumping region causing a two-phase flow.

No additional molten metal experiments have been conducted to date; however, these experiments clearly demonstrate that the EM pump does work and that the pressure measuring system is working. As a result, it can be concluded that a molten salt cannot be pumped via this system due to low electrical conductivity. As a result, additional methods to performs LIBS on a non-static molten salt must be explored.